eXPRESS Polymer Letters Vol.10, No.9 (2016) 721
Available online at www.expresspolymlett.com
DOI: 10.3144/expresspolymlett.2016.65

Editorial corner – a personal view
'Energy Materials' … the role of polymers

G. C. Psarras[*]

Department of Materials Science, University of Patras, 26504 Patras, Hellas (Greece)

In physics textbooks energy is defined as the capacity of a physical system to do work. Moreover, energy can be converted from a form to another, transferred and stored. Although the previous definition appears to be confusing for non-scientists, energy is related to everyday life worldwide. Regional and global economies, and the resulting policies, are directly related to the production, transfer, storage and utilization of energy. Energy resources, as well as the transport pipelines constitute important points of the geopolitical status.

Over the past decades huge amounts of fossil fuels were consumed causing the rapid depletion of the known reserves, in tandem with the worsening of environmental pollution, global climate change and health effect. The output is an increasing demand for renewable and clean energy sources, and a more efficient use of energy. Materials are crucial to all stages of energy, including production, transportation, storage, harvesting and exploitation. A vast variety of portable electronic devices and electric vehicles became extremely popular in our days. The development of these devices creates the necessity for portable energy storage systems such as batteries, supercapacitors etc. Requirements underline the demand for a new class of materials characterized by high energy/power density, flexibility, low weight and cost. Materials for energy receive increasing attention and polymers play an important role in this aspect too.

Fuel cells are environmental friendly, silent since they do not posses moving parts, and can be kept in operation as long as the oxidant and the fuel are suitably fed. Fuel cells with polymer electrolyte exhibit high power performance at low or intermediate temperatures, being thus promising power supplies for stationary and portable applications. Solid state lithium polymer batteries is the next step in electrochemical storage systems due to their high safety, energy density, and multiple charging/decharging cycles. Major drawback appears to be their low ionic conductivity at room temperature. Furthermore, solar cells with organic quantum dots and polymer-based organic photovoltaics constitute additional energy devices. The undeniable importance of electric energy is related to the need of better storage. Multifunctional polymer composites could be exploited as structural energy storing devices, where matrix and filler synergistically undertake the roles of structural support and energy storage. Therefore, a breakthrough in research and development of energy-materials is expected in near future.

Prof. Dr. Georgios C. Psarras
Member of International Advisory Board

[*]Corresponding author, e-mail: G.C.Psarras@upatras.gr

eXPRESS Polymer Letters Vol.10, No.9 (2016) 722–729
Available online at www.expresspolymlett.com
DOI: 10.3144/expresspolymlett.2016.66

Acceleration effect of ionic liquids on polycyclotrimerization of dicyanate esters

A. Fainleib[1*], *O. Grigoryeva*[1], *O. Starostenko*[1], *A. Vashchuk*[1], *S. Rogalsky*[2], *D. Grande*[3]

[1]Institute of Macromolecular Chemistry, National Academy of Sciences of Ukraine, Kharkivske shose 48, 02160 Kyiv, Ukraine
[2]Institute of Bioorganic Chemistry and Petrochemistry, National Academy of Sciences of Ukraine, Kharkivske shose 50, 02160 Kyiv, Ukraine
[3]Institut de Chimie et des Matériaux Paris-Est, UMR 7182 CNRS – Université Paris-Est Créteil Val-de-Marne, 2, rue Henri Dunant, 94320 Thiais, France

Received 25 January 2016; accepted in revised form 21 March 2016

Abstract. The polycyclotrimerization reaction of dicyanate ester of bisphenol E (DCBE) in the presence of varying amounts (from 0.5 to 5 wt%) of 1-octyl-3-methylimidazolium tetrafluoroborate ([OMIm][BF_4]) ionic liquid has been investigated using differential scanning calorimetry (DSC) and Fourier transform infrared spectroscopy (FTIR) techniques, after a curing stage at 150 °C for 6 h. It is noteworthy that an amount of [OMIm][BF_4] as low as 0.5 wt% accelerates dramatically the thermal curing process leading to the formation of a polycyanurate network. The conversion of DCBE increased with increasing [OMIm][BF_4] content in the temperature range studied. A reaction mechanism associated with the ionic liquid-catalyzed DCBE polycyclotrimerization is newly proposed *via* the involvement of a $[CN]^{\delta+}$–$[OMIm]^{\delta-}$ complex as a key intermediate.

Keywords: *polymer synthesis, polycylotrimerization, cyanate ester resins, ionic liquid*

1. Introduction

Cyanate ester resins (CERs) – also known as polycyanurates (PCNs) – are commonly used in aerospace applications and electronic devices as high temperature polymer matrices. The specific interest in these high performance polymers arises from their unique combination of intrinsic properties, including thermal, fire, radiation and chemical resistance, high tensile moduli (3.1–3.4 GPa) and glass transition temperatures (T_g > 250 °C), low dielectric constants (ε ~ 2.5–3.2), high adhesion to conductor metals and composites as well as low water/moisture adsorption [1, 2].

Ionic liquids (ILs) have attracted widespread interest in polymer science, due to their unique properties, such as low melting temperature, incombustibility, electrochemical, and high-temperature stability. They have progressively been used as solvents and substances with catalytic properties [3, 4] as well as conductive fillers [5]. Miscellaneous reports on using ILs in polymerization processes have been published [6–12]. For instance, Wu *et al*. [12] have recently investigated the cationic polymerization of isobutyl vinyl ether in 1-octyl-3-methylimidazolium tetrafluoroborate ([OMIm][BF_4]). It was noticed that the cationic process led to higher monomer conversions in the presence of [OMIm][BF_4]. Although the polymerization reaction in [OMIm][BF_4] could not be controlled, due to the presence of β-proton elimination, the monomer addition experiments confirmed the existence of long-lived species. The results showed that introducing a small amount of 2,6-di-tertiobutyl

*Corresponding author, e-mail: fainleib@i.ua

pyridine into the system might lead to a controlled polymerization. In contrast, reports on ILs involved in crosslinking processes are much scarcer [13].

The curing kinetics of neat CERs has extensively been reported in the literature [14–21]. It is of common knowledge that the polycyclotrimerization of dicyanate esters is rather slow, and it generally requires the presence of a curing catalyst which may be either a Lewis acids or acetylacetonates of Cu^{2+}, Co^{3+}, Zn^{2+} and Mn^{2+} [22], or a chelate in the presence of an active hydrogen-containing co-catalyst (such as nonylphenol), acting as a source of proton. Recently, Throckmorton [23] has examined the effect of ILs on curing of cyanate esters in IL-modified thermosets and their nanocomposites, and interestingly, he concluded that the ionic liquids accelerated the CER curing.

In the present work, we have highlighted the acceleration effect occurring in the polymerization of a dicyanate monomer in the presence of a specific ionic liquid, namely [OMIm][BF_4], and for the first time suggested the mechanism of the polycyclotrimerization of cyanate ester in the presence of imidazolium IL. It is worth noting that ILs are thermally stable compounds that is important for the polycyclotrimerization, which is usually carried out at high temperatures up to 230–280 °C [1, 2]. The structure of such catalyst systems allows for easier separation, recovery, and recycling from the reaction mixtures [24]. Additionally, introducing ILs into CER frameworks may impart conductivity to the CER-based nanocomposites. ILs could be extracted and potentially used repeatedly; therefore, CER/IL composites could be applied as precursors to porous materials as well.

2. Experimental

2.1. Materials

1,1′-Bis(4-cyanatophenyl)ethane (dicyanate ester of bisphenol E, DCBE) under the trade name Primaset™ LECy, was kindly supplied by Lonza Ltd., Switzerland, and was used as received. The following chemicals were used for the synthesis of the 1-octyl-3-methylimidazolium tetrafluoroborate ([OMIm][BF_4]): 1-methylimidazole, 1-bromooctane, tetrafluoroboric acid (50% in H_2O), ethyl acetate, hexane, methylene chloride, and sodium sulfate. The chemicals were provided by Fluka and were used as received.

2.2. Ionic liquid synthesis

1-octyl-3-methylimidazolium tetrafluoroborate [OMIm][BF_4] was synthesized using the approaches described elsewhere [25, 26]. The mixture of 1-bromooctane (27 g, 0.14 mol) and 1-methylimidazole (10 g, 0.12 mol) was heated at 140 °C for 2 h under stirring and argon atmosphere. The viscous liquid of light brown color obtained was cooled to room temperature and washed with ethyl acetate-hexane mixture (3:1 (v/v), 3×100 mL). Residual solvents were removed under reduced pressure, and the obtained product was dissolved in 150 mL of water. Tetrafluoroboric acid (25 mL) was added to the solution, followed by stirring for 1 h. The water immiscible layer formed was extracted with methylene chloride (2×100 mL), and dried overnight with sodium sulfate. The solvent was distilled off, and the resulting ionic liquid was dried under a reduced pressure of 1 mbar at 80 °C for 12 h. The product yield was equal to 72%. The onset temperature of thermal degradation (T_d) was equal 343 °C as determined by thermogravimetric analysis (TGA) under air.

^{1}H NMR (300 MHz, DMSO-D_6): δ = 0.86 (t, 3H, CH_3, J = 7.2 Hz), 1.25 (m, 10H, $CH_3(CH_2)_5$), 1.78 (m, 2H, NCH_2CH_2), 3.85 (s, 3H, NCH_3), 4.16 (t, 2H, NCH_2, J = 7.2 Hz), 7.67 (br s, 1H, C_4–H), 7.74 (br s, 1H, C_5–H), 9.06 (s, 1H, C_2–H). ^{19}F NMR (188 MHz, DMSO-D_6): δ = –148.8 (s, 4F, BF_4).

2.3. Preparation of CER/[OMIm][BF_4] samples

The blends of DCBE monomer with 0.5, 1.0, 2.0, 3.0, 4.0, and 5.0 wt% [OMIm][BF_4] were stirred at $T \approx 20$ °C for 3 min to obtain homogeneous mixtures, followed by a heating step at 150 °C for 6 h.

2.4. Physico-chemical techniques

^{1}H NMR and ^{19}F NMR techniques were used to characterize the ionic liquid. The spectra were recorded with a Varian (300 MHz) NMR spectrometer at 23 °C using DMSO-D6 as the deuterated solvent.

The thermal stability of the ionic liquid was assessed by TGA under air atmosphere using a TA Instruments TGA Q-50 thermobalance over a temperature range from 25 to 700 °C at a heating rate of 10 °C·min^{-1}.

Differential scanning calorimetry (DSC) measurements were performed using a Perkin-Elmer DSC-7 under nitrogen atmosphere, in a temperature range

from 150 to 340 °C at a heating rate of 10 °C·min^{-1}. The samples mass was about 6–9 mg. The post-curing conversion (α_{post}) of cyanate (O–C≡N) groups from DCBE was calculated from Equation (1) [27]:

$$\alpha_{post} = \left(\alpha_c + \frac{\Delta H_t}{\Delta H_{tot}}\right) \cdot 100 \quad (1)$$

where $\alpha_c[(\Delta H_{tot} - \Delta H_{post})/\Delta H_{tot}]$ [28] is the conversion after heating at 150 °C for 6 h, ΔH_t is the reaction enthalpy at time t, ΔH_{tot} is the total enthalpy of polycyclotrimerization of DCBE monomer (ΔH_{tot} = 770 J·g^{-1} [29]), and ΔH_{post} is the post-curing enthalpy, which was calculated from the exotherm area of cured sample divided by its mass.

Fourier transform infrared (FTIR) spectra were recorded between 4000 and 600 cm^{-1} using a Bruker Tensor 37 spectrometer. For each spectrum, 16 consecutive scans with a resolution of 0.6 cm^{-1} were averaged. All spectra were recorded at room temperature. The monomer conversion was determined from the absorbance variation of the bands with maxima at 2266 and 2235 cm^{-1}, corresponding to the stretching vibrations of the cyanate groups. The stretching band of benzene ring at 1501 cm^{-1} was used as an internal standard. The conversion (α_c) of cyanate groups after heating at 150 °C for 6 h was calculated from Equation (2):

$$\alpha_c = 1 - \frac{\frac{A_{(t)2266-2235}}{A_{(0)2266-2235}}}{\frac{A_{(t)1501}}{A_{(0)1501}}} \cdot 100 \quad (2)$$

where $A_{(t)2266–2235}$ is the area under absorption bands of O–C≡N groups at time t, $A_{(t)1501}$ is the area under absorption band of benzene ring at time (t), and $A_{(0)}$ is the area under absorption bands of the corresponding groups in initial DCBE monomer.

3. Results and discussion

In the first stage the mixtures of DCBE monomer with different amounts of ionic liquid [OMIm][BF$_4$] were heated at 150 °C for 6 h. In the presence of a catalyst, one such curing step permitted to attain a gel point [30].

3.1. DSC analysis

Figure 1a exhibits the DSC thermograms for neat CER and CER/[OMIm][BF$_4$] samples of different compositions cured at 150 °C for 6 h, and their main thermal characteristics are summarized in Table 1. For the neat CER sample, the exotherm maximum is associated with a temperature of post-curing (T_{p1}) equal to 294 °C with some weak shoulder at ~239 °C. The shoulder may be attributed to the formation of the intermediate linear CER dimers, trimers and potentially other higher even-mers [31]. The CER/[OMIm][BF$_4$] samples display bimodal curing profiles with distinct exothermic peaks corresponding to CER post-curing process at the selected heating rate (10 °C·min^{-1}). For the CER/[OMIm][BF$_4$] specimens, T_{p1} was shifted toward much lower temperatures, *i.e.* 218–221 °C (Table 1). This fact attested that, in the presence of [OMIm][BF$_4$], the polycyclotrimerization of DCBE

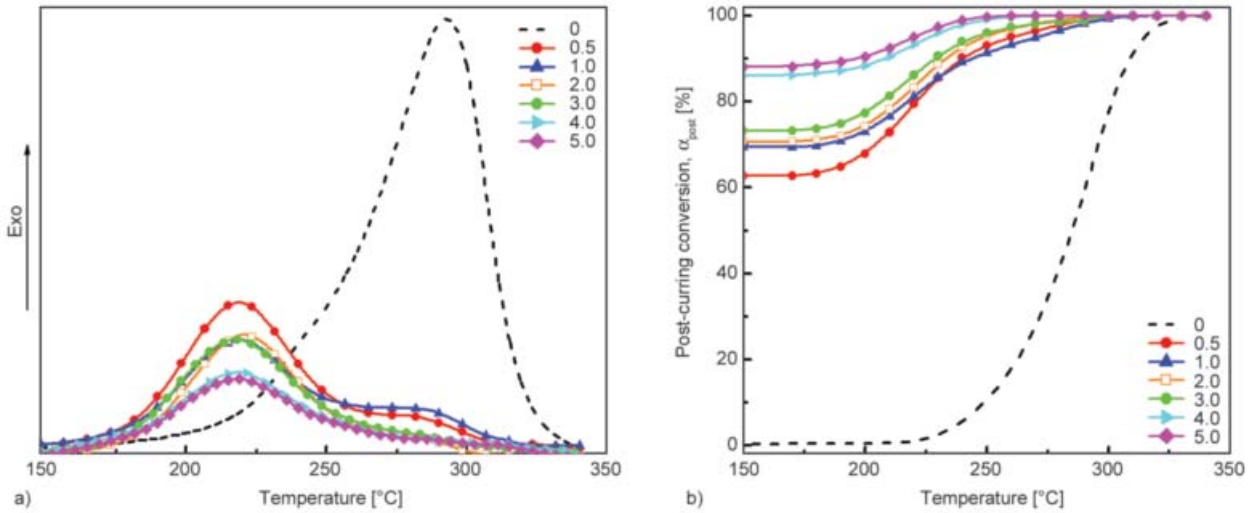

Figure 1. (a) DSC thermograms and (b) temperature dependence of post-curing conversion for CER samples with different [OMIm][BF$_4$] contents

Table 1. Thermal characteristics of CER/[OMIm][BF_4] samples cured at 150 °C for 6 h as determined by DSC

[OMIm][BF_4] content [wt%]	Post-curing interval [°C]			T_{p1}[b] [°C]	T_{p2}[c] [°C]	ΔH_{post}[d] [J·g^{-1}]	ΔH_c[e] [J·g^{-1}]
	T_{onset}	T_{end}	ΔT[a]				
0.0	160	339	179	294	–	755	15
0.5	154	319	165	219	280	296	474
1.0	156	324	168	218	279	233	537
2.0	156	320	164	221	280	223	544
3.0	155	318	163	218	281	203	567
4.0	154	320	166	220	282	120	650
5.0	153	318	165	218	282	114	656

[a]Post-curing temperature interval: $\Delta T = T_{end} - T_{onset}$
[b]Peak temperature of post-curing associated with first endotherm maximum
[c]Peak temperature of post-curing associated with second endotherm maximum
[d]Post-curing enthalpy under selected conditions (from 150 to 340 °C at 10 °C·min^{-1})
[e]Curing enthalpy after heating at 150 °C for 6 h: $\Delta H_c = \Delta H_{tot} - \Delta H_{post}$, ΔH_{tot} = 770 J·g^{-1} [30]

mostly occurred at lower temperatures. Yet, in the latter case, it should be noted that weak peaks (T_{p2}) appeared around 279–282 °C, namely at a temperature similar to that of pure DCBE polymerization. One could suppose that the first exotherm maximum corresponded to the curing reaction catalyzed by [OMIm][BF_4], while the second peak was attributed to a higher temperature thermal curing without catalyst participation.

Table 1 clearly shows that the reaction rate of CER curing was enhanced by the presence of [OMIm][BF_4]. It is noteworthy that loading of [OMIm][BF_4] was associated with a substantial narrowing the post-curing temperature interval from 179° C for neat CER to 163–168 °C for CER/ [OMIm][BF_4] samples. Moreover, the enthalpy of post-curing process (ΔH_{post}) for pure DCDE was equal to 755 J·g^{-1}. According to literature [29], the total enthalpy of polycyclotrimerization of DCBE monomer (ΔH_{tot}) was equal to 770 J·g^{-1}. Therefore, one could conclude that the polymerization of neat DCBE practically did not occur after the 6 h-curing stage at 150 °C. In sharp contrast, ΔH_{post} for DCBE post-polycyclotrimerization in the IL-containing samples dramatically decreased with increasing [OMIm][BF_4] contents, so in turn the curing enthalpy after the curing stage at 150 °C for 6 h (ΔH_c) increased accordingly.

Figure 1b displays the temperature dependence of post-curing conversion values (α_{post}) for neat CER and CER/[OMIm][BF_4] samples. As stated above, the polymerization of DCBE monomer hardly occurred during thermal heating at 150 °C for 6 h, thus the corresponding curve started around 2% conversion. When pure DCBE was post-cured from 150 to 340 °C with a heating rate of 10 °C min^{-1}, an induction period was found to last around 7.5 min before reaching 225 °C, *i.e.* the temperature from which α_{post} appeared to sharply increase up to 100% conversion. Contrarily, the O–C≡N conversion (α_c) in the CER/[OMIm][BF_4] samples after heating at 150 °C for 6 h reached values as high as 62–85%, depending on the [OMIm][BF_4] content (Table 2). Notably, complete conversion was not reached because of the low curing temperature (150 °C) as far as the final curing temperature should be equal to 230–270 °C, and even higher [1, 2]. When heating from 150 to 340 °C, the DCBE conversion values (α_{post}) further increased gradually to attain completion. In summary, the higher the [OMIm][BF_4] content, the higher the O–C≡N conversion (α_c) reached after heating at 150 °C for 6 h, and the shorter the time to reach complete conversion during post-curing process.

Table 2. Conversion values (α_c) for CER/[OMIm][BF_4] samples after heating at 150 °C for 6 h

[OMIm][BF_4] content [wt%]	α_c [%]	
	DSC[a]	FTIR[b]
0.0	2	1
0.5	62	59
1.0	69	65
2.0	71	76
3.0	74	77
4.0	84	86
5.0	85	87

[a]The experimental error on values determined by DSC was estimated to be equal to 1%
[b]The experimental error on values determined by FTIR was estimated to be equal to 2%

3.2. FTIR analysis

The peculiarities of DCBE polycyclotrimerization in the absence and in the presence of [OMIm][BF_4] were also investigated using FTIR. Figure 2 shows the FTIR absorption spectra for uncured DCBE monomer (curve 0), neat CER (curve 0_T), and CER/[OMIm][BF_4] samples (curves 0.5_T–5.0_T) after heating at 150 °C for 6 h. For neat CER, no visible changes in the intensity of the bands of cyanate groups at 2266–2235 cm^{-1} were observed, and a very low conversion of DCBE could be suggested on the basis of the appearance of small bands at 1563 and 1366 cm^{-1}, corresponding to C=N–C groups and N–C–O groups of cyanurate cycles, respectively. In contrast, concerning CER/[OMIm][BF_4] samples, the intensity of the bands at 2266–2235 cm^{-1} decreased, and bands clearly appeared at 1563 and 1366 cm^{-1}, thus evidencing the formation of polycyanurate crosslinked structures. This conclusion was in a good agreement with the DSC data discussed above. The conversion values (α_c) of O–C≡N groups associated with the different [OMIm][BF_4] contents was calculated using FTIR data, and both sets of values obtained from FTIR and DSC data matched pretty well (see Table 2).

Both FTIR and DSC results clearly evidenced an acceleration effect of [OMIm][BF_4] on the CER formation during curing process at 150 °C for 6 h. Interestingly, the catalytic effect was already noticeable at the lowest content of [OMIm][BF_4] investigated, *i.e.* 0.5 wt%. This could be attributed to the presence of an acid center in the ring of the [OMIm] cation, which might accelerate the polycyclotrimerization of the dicyanate monomer.

3.3. Proposed mechanism of the [OMIm][BF_4]-catalyzed cyclotrimerization of DCBE

It has been well investigated that Lewis acids, such as $TiCl_4$, could be used as catalysts for polycyclotrimerization of dicyanate esters [32]. Martin and coworkers [33, 34] reported the appearance of bands around 2300 cm^{-1} when dicyanates were treated with an excess of Lewis acid. A strong band at 2320 cm^{-1} indeed appeared upon addition of 1–5 equiv. of $TiCl_4$ to bisphenol A dicyanate ester; no 'free' cyanate was detectable in these cases [32]. The band at 2320 cm^{-1}, attributed to a cyanate-catalyst complex, was formed rapidly on mixing before gradually disappearing at the end of the reaction. Therefore, the band around 2300–2320 cm^{-1} was ascribed to a simple cyanate-Lewis acid complex [32–34].

Likewise, in our investigation, we proposed a mechanism involving a cyanate-ionic liquid complex. Indeed, the appearance of a shoulder at 2330 cm^{-1} in

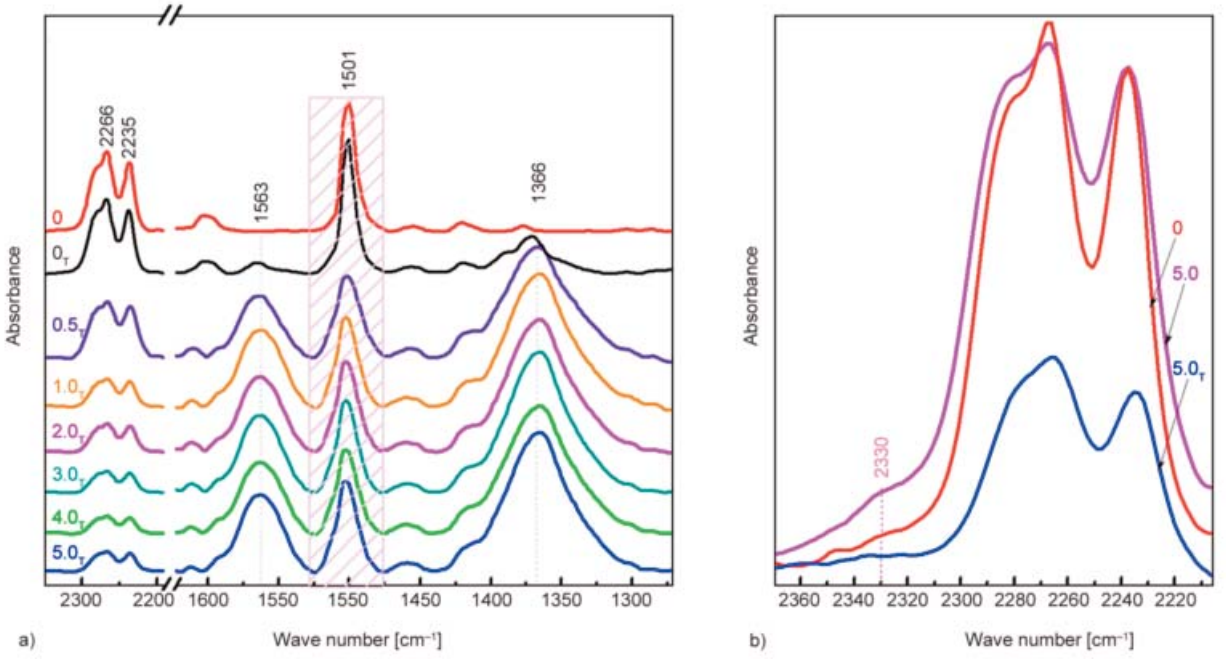

Figure 2. FTIR spectra of: (a) DCBE monomer (curve 0) and CER samples with different [OMIm][BF_4] contents after heating at 150 °C for 6 h (curves 0_T–5.0_T, the number indicating the IL content); (b) uncured DCBE (curve 0) and CER/[OMIm][BF_4] sample (95/5 wt%) before (curve 5.0) and after (curve 5.0_T) the same heating stage in the spectral zone of 2370–2200 cm^{-1}

the FTIR spectra after mixing DCBE with 5 wt% of [OMIm][BF_4] was observed in Figure 2b (curve 5.0). After heating the mixture at 150 °C for 6 h and reaching high conversion of cyanate groups, this shoulder disappeared (curve 5.0_T). We proposed a possible mechanism for the DCBE/[OMIm][BF_4] system in Figure 3. First, a pseudo-nitrillium ion **2** was formed when mixing dicyanate **1** with [OMIm][BF_4] *via* the involvement of a $[CN]^{\delta+}$–$[OMIm]^{\delta-}$ complex whose characteristic FTIR absorption band could be assigned to the shoulder at 2330 cm^{-1}. This cyanate-ionic liquid complex was then attacked by a 'free' cyanate monomer **1**, thus leading to the formation of a nitrillium ion **3**. The latter was attacked by a 'free' dicyanate molecule **1** with formation of a nitrillium ion **4**, which was transformed into an acyclic trimer **5** with [OMIm][BF_4] release, and finally into a cyclotrimer (cyanurate) **6**. Taking in account the existence of an acid center in the ring of 1-octyl-3-methylimidazolium cation (*i.e.*, C–H bond in position **2** imparts slight acidity); we could suppose that this center indeed catalyzed the cyclotrimerization reaction of DCBE. It has to be noted here that a small shoulder at 2330 cm^{-1} is also observed in the FTIR spectrum of the DCBE. It is known that phenolic groups catalyze polycyclotrimerization of CER and

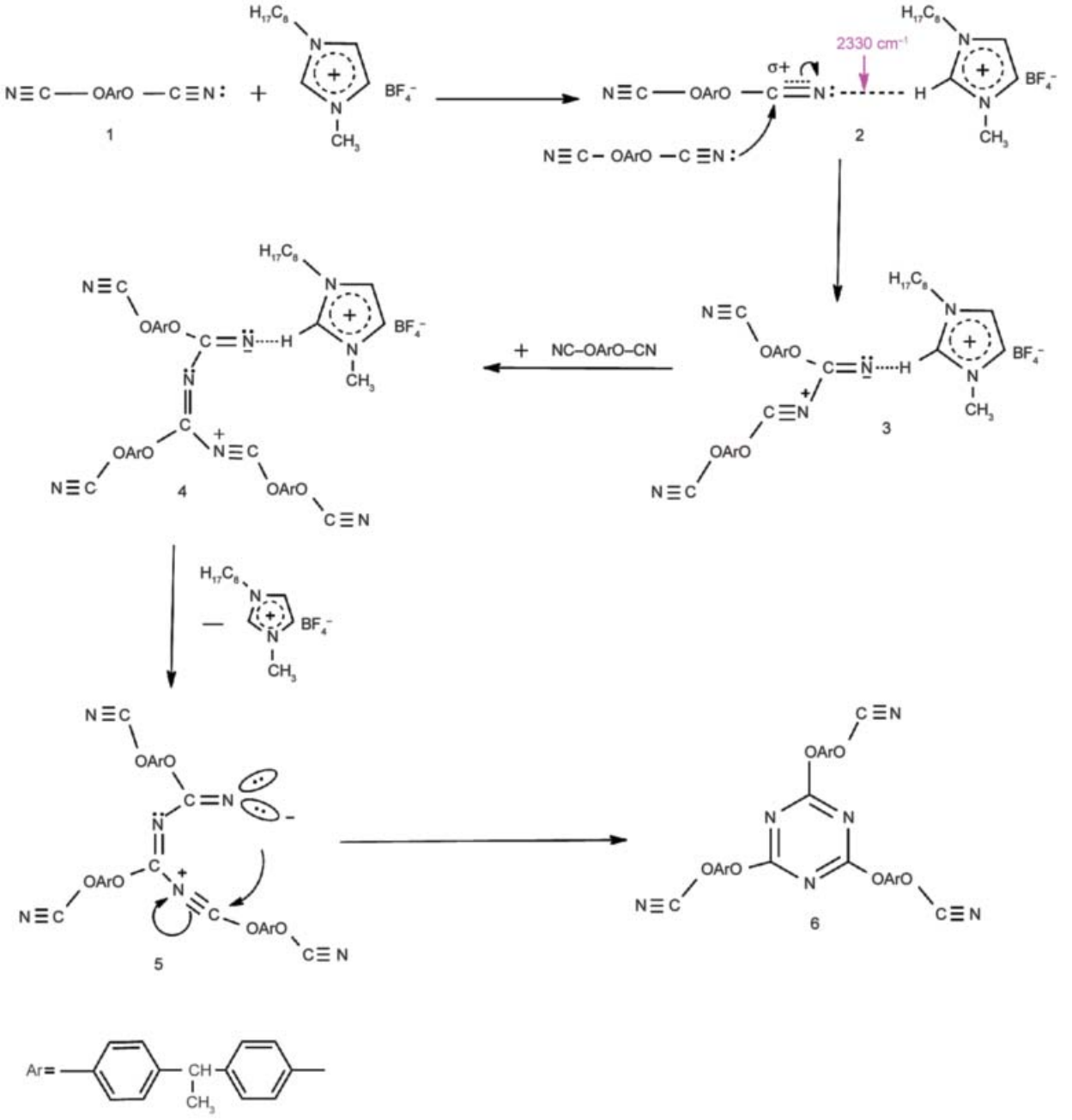

Figure 3. Proposed mechanism for the [OMIm][BF_4]-catalyzed cyclotrimerization of DCBE

it occurs also through formation of the intermediate structure, which disappear after formation of triazine cycle and reclaiming phenol [1]. So the traces of bisphenol E, left after DCBE synthesis, could form the dimer structures with cyanate ester and this complex may be also characterized by the shoulder at 2330 cm^{-1} in FTIR spectrum of neat cyanate ester.

4. Conclusions

The [OMIm][BF_4]-catalyzed polycyclotrimerization of DCBE was investigated through DSC and FTIR analyses. A dramatic influence of the ionic liquid on CER curing was demonstrated. For samples containing [OMIm][BF_4], polycyclotrimerization of DCBE took place even at the heating stage at 150 °C, while for pure DCBE polycyclotrimerization practically did not occur. The conversion of DCBE increased with increasing [OMIm][BF_4] contents in the temperature range studied. A plausible mechanism based on the formation of a $[CN]^{\delta+}$–$[OMIm]^{\delta-}$ complex was proposed to account for the acceleration effect of the ionic liquid on the curing process associated with CERs. We assume that one such catalytic effect of imidazolium-based ILs will take place for any dicyanate monomer. The effect of other IL types on kinetics of polycyclotrimerization of dicyanate esters has to be further studied.

It should be emphasized that [OMIm][BF_4] displayed a catalytic activity in the absence of any additional organic solvent or co-catalyst. Interestingly, the ionic liquid is not destroyed during the CER synthesis.

Acknowledgements

The authors gratefully acknowledge the National Academy of Sciences of Ukraine (NASU) and the 'Centre National de la Recherche Scientifique' (CNRS) of France for partial financial support through bilateral cooperation project No. 26199.

References

[1] Hamerton I.: Chemistry and technology of cyanate ester resins. Chapman and Hall, Glasgow (1994).

[2] Fainleib A.: Thermostable polycyanurates: Synthesis, modification, structure and properties. Nova Science Publishers, New York (2010).

[3] Wang Y., Li H., Wang C., Jiang H.: Ionic liquids as catalytic green solvents for cracking reactions. Chemical Communications, **17**, 1938–1939 (2004).
DOI: 10.1039/B402524E

[4] Olivier-Bourbigou H., Magna L., Morvan D.: Ionic liquids and catalysis: Recent progress from knowledge to applications. Applied Catalysis A: General, **373**, 1–56 (2010).
DOI: 10.1016/j.apcata.2009.10.008

[5] Ohno H., Yoshizawa M., Ogihara W.: Development of new class of ion conductive polymers based on ionic liquids. Electrochimica Acta, **50**, 255–261 (2004).
DOI: 10.1016/j.electacta.2004.01.091

[6] Wasserscheid P., Welton T.: Ionic liquids in synthesis. Wiley, Weinheim (2002).

[7] Holbrey J. D., Chen J., Turner M. B., Swatloski R. P., Spear S. K., Rogers R. D.: Applying ionic liquids for controlled processing of polymer materials. in 'Ionic liquids in polymer systems' (eds.: Brazel C. S., Rogers R. D.) ACS Symposium Series, Washington, Vol 913, 71–87 (2005).
DOI: 10.1021/bk-2005-0913.ch005

[8] Pârvulescu V. I., Hardacre C.: Catalysis in ionic liquids. Chemical Reviews, **107**, 2615–2665 (2007).
DOI: 10.1021/cr050948h

[9] Strehmel V., Berdzinski S., Ehrentraut L., Faßbender C., Horst J., Leeb E., Liepert J., Ruby M-P., Senkowski V., Straßburg P., Wenda A., Strehmel C.: Application of ionic liquids in synthesis of polymeric binders for coatings. Progress in Organic Coatings, **89**, 297–313 (2015).
DOI: 10.1016/j.porgcoat.2015.07.025

[10] Stejskal J., Dybal J., Trchová M.: The material combining conducting polymer and ionic liquid: Hydrogen bonding interactions between polyaniline and imidazolium salt. Synthetic Metals, **197**, 168–174 (2014).
DOI: 10.1016/j.synthmet.2014.09.002

[11] Trchová M., Šeděnková I., Morávková Z., Stejskal J.: Conducting polymer and ionic liquid: Improved thermal stability of the material – A spectroscopic study. Polymer Degradation and Stability, **109**, 27–32 (2014).
DOI: 10.1016/j.polymdegradstab.2014.06.012

[12] Wu Y-B., Han L., Zhang X-G., Mao J., Gong L-F., Guo W-L., Gu K., Li S-X.: Cationic polymerization of isobutyl vinyl ether in an imidazole-based ionic liquid: Characteristics and mechanism. Polymer Chemistry, **6**, 2560–2568 (2015).
DOI: 10.1039/C4PY01784F

[13] Snedden P., Cooper A. I., Khimyak Y. Z., Scott K., Winterton N.: Cross-linked polymers in ionic liquids: Ionic liquids as porogens. in 'Ionic liquids in polymer systems' (eds.: Brazel C. S., Rogers R. D.) ACS Symposium Series, Washington, Vol 913, 133–147 (2005).
DOI: 10.1021/bk-2005-0913.ch009

[14] Osei-Owusu A., Martin G. C., Gotro J. T.: Analysis of the curing behavior of cyanate ester resin systems. Polymer Engineering and Science, **31**, 1604–1609 (1991).
DOI: 10.1002/pen.760312208

[15] Osei-Owusu A., Martin G. C., Gotro J. T.: Catalysis and kinetics of cyclotrimerization of cyanate ester resin systems. Polymer Engineering and Science, **32**, 535–541 (1992).
DOI: 10.1002/pen.760320805

[16] Wu S. J., Mi F. L.: Cure kinetics of a cyanate ester blended with poly(phenylene oxide). Polymer International, **55**, 1296–1303 (2006).
DOI: 10.1002/pi.2083

[17] Gómez C. M., Recalde I. B., Mondragon I.: Kinetic parameters of a cyanate ester resin catalyzed with different proportions of nonylphenol and cobalt acetylacetonate catalyst. European Polymer Journal, **41**, 2734–2741 (2005).
DOI: 10.1016/j.eurpolymj.2005.05.005

[18] Simon S. L., Gillham K. J.: Cure kinetics of a thermosetting liquid dicyanate ester monomer/high-T_g polycyanurate material. Journal of Applied Polymer Science, **47**, 461–485 (1993).
DOI: 10.1002/app.1993.070470308

[19] Li W., Liang G., Xin W.: Triazine reaction of cyanate ester resin systems catalyzed by organic tin compound: Kinetics and mechanism. Polymer International, **53**, 869–876 (2004).
DOI: 10.1002/pi.1446

[20] Fainleib A., Bardash L., Boiteux G.: Catalytic effect of carbon nanotubes on polymerization of cyanate ester resins. Express Polymer Letters, **3**, 477–482 (2009).
DOI: 10.3144/expresspolymlett.2009.59

[21] Bershtein V. A., Fainleib A. M., Pissis P., Bei I. M., Dalmas F., Egorova L. M., Gomza Y. P., Kripotou S., Maroulos P., Yakushev P. N.: Polycyanurate–organically modified montmorillonite nanocomposites: Structure–dynamics–properties relationships. Journal of Macromolecular Science Part B: Physics, **47**, 555–575 (2008).
DOI: 10.1080/00222340801955545

[22] Li Q. F., Lu K., Yang Q. Q., Jin R.: The effect of different metallic catalysts on the coreaction of cyanate/epoxy. Journal of Applied Polymer Science, **100**, 2293–2302 (2006).
DOI: 10.1002/app.22882

[23] Throckmorton J. A.: Ionic liquid-modified thermosets and their nanocomposites: Dispersion, exfoliation, degradation, and cure. PhD dissertation, Drexel University (2015).

[24] Valkenberg M. H., de Casto C., Hölderich W. F.: Immobilisation of ionic liquids on solid supports. Green Chemistry, **4**, 88–93 (2002).
DOI: 10.1039/B107946H

[25] Dzyuba S. V., Bartsch R. A.: Efficient synthesis of 1-alkyl(aralkyl)-3-methyl(ethyl)imidazolium halides: Precursors for room-temperature ionic liquids. Journal of Heterocyclic Chemistry, **38**, 265–268 (2001).
DOI: 10.1002/jhet.5570380139

[26] Ennis E., Handy T. S.: Facile route to C2-substituted imidazolium ionic liquids. Molecules, **14**, 2235–2245 (2009).
DOI: 10.3390/molecules14062235

[27] Li J., Chen P., Ma Z., Ma K., Wang B.: Reaction kinetics and thermal properties of cyanate ester-cured epoxy resin with phenolphthalein poly(ether ketone). Journal of Applied Polymer Science, **111**, 2590–2596 (2009).
DOI: 10.1002/app.29264

[28] Zhao L., Hu X.: A variable reaction order model for prediction of curing kinetics of thermosetting polymers. Polymer, **48**, 6125–6133 (2007).
DOI: 10.1016/j.polymer.2007.07.067

[29] Reams J. T., Guenthner A. J., Lamison K. R., Vij V., Lubin L. M., Mabry J. M.: Effect of chemical structure and network formation on physical properties of di(cyanate ester) thermosets. ACS Applied Materials and Interfaces, **4**, 527–535 (2012).
DOI: 10.1021/am201413t

[30] Fainleib A., Gusakova K., Grigoryeva O., Starostenko O., Grande D.: Synthesis, morphology, and thermal stability of nanoporous cyanate ester resins obtained upon controlled monomer conversion. European Polymer Journal, **73**, 94–104 (2015).
DOI: 10.1016/j.eurpolymj.2015.10.009

[31] Kasehagen L. J., Macosko C. W.: Structure development in cyanate ester polymerization. Polymer International, **44**, 237–247 (1997).
DOI: 10.1002/(SICI)1097-0126(199711)44:3<237::AID-PI868>3.0.CO;2-L

[32] Cunningham I. D., Brownhill A., Hamerton I., Howlin B.: Kinetics and mechanism of the titanium tetrachloride-catalysed cyclotrimerisation of aryl cyanates. Journal of the Chemical Society, Perkin Transactions 2, **9**, 1937–1943 (1994).
DOI: 10.1039/P29940001937

[33] Martin D., Weise A.: Cyansäureester, XIV. Komplexe von Cyansäure-arylestern mit Lewis-säuren und ihre Alkylierung (in German). Chemische Berichte, **100**, 3747–3755 (1967).
DOI: 10.1002/cber.19671001133

[34] Martin D., Bauerand M., Pankratov V. A.: Cyclotrimerisation of cyano-compounds into 1,3,5-triazines. Russian Chemical Reviews, **47**, 975–990 (1978).
DOI: 10.1070/RC1978v047n10ABEH002288

eXPRESS Polymer Letters Vol.10, No.9 (2016) 730–741
Available online at www.expresspolymlett.com
DOI: 10.3144/expresspolymlett.2016.67

Mechanical and electro-mechanical properties of three-dimensional nanoporous graphene-poly(vinylidene fluoride) composites

G. P. Zheng[1,2*], *Z. Y. Jiang*[2], *Z. Han*[1,2], *J. H. Yang*[1]

[1]School of Materials Science and Engineering, University of Shanghai for Science and Technology, Shanghai 200093, China
[2]Department of Mechanical Engineering, Hong Kong Polytechnic University, Hung Hom, Kowloon, Hong Kong, China

Received 13 January 2016; accepted in revised form 28 March 2016

Abstract. Three-dimensional nanoporous graphene monoliths are utilized to prepare graphene-poly(vinylidene fluoride) nanocomposites with enhanced mechanical and electro-mechanical properties. Pre-treatment of the polymer (poly(vinylidene fluoride), PVDF) with graphene oxides (GOs) facilitates the formation of uniform and thin PVDF films with a typical thickness below 100 nm well coated at the graphene nano-sheets. Besides their excellent compressibility, ductility and mechanical strength, the nanoporous graphene-PVDF nanocomposites are found to possess high sensitivity in strain-dependent electrical conductivity. The improved mechanical and electro-mechanical properties are ascribed to the enhanced crystalline β phase in PVDF which possesses piezoelectricity. The mechanical relaxation analyses on the interfaces between graphene and PVDF reveal that the improved mechanical and electro-mechanical properties could result from the interaction between the –C=O groups in the nanoporous graphene and the $–CF_2$ groups in PVDF, which also explains the important role of GOs in the preparation of the graphene-polymer nanocomposites with superior combined mechanical and electro-mechanical properties.

Keywords: *processing technology, nanoporous graphene, ferroelectric polymers, mechanical properties, dynamic mechanical relaxation*

1. Introduction

In the past several years three-dimensional (3D) nanoporous graphene structures have attracted much attention since they are promising multi-functional materials which implement the superior properties of two-dimensional (2D) graphene sheets for macroscopic applications [1–5]. Graphene aerogel (GA) is the most typical 3D network structure consisting of graphene nano-sheets and possesses ultra-light weight (density as low as 0.16 mg/cm^3), ultra-high surface area (as large as 600 m^2/g), super-elasticity, high compressibility and conductivity. They could be used as mechanical dampers, strain gauge, stress and pressure sensors with high performances [6–10]. However their weak inter-connected graphene structures have prevented GAs from exhibiting stable mechanical and electro-mechanical behaviours. For example, the mechanical strength (<100 kPa) and Young's modulus (<5 MPa) of GA are too low for practical functional application [1–3]. In particular, formation of micro-cracks inside GAs after cyclic loading could deteriorate their mechanical and electro-mechanical performances.

In this work, we develop GA supported poly(vinylidene fluoride) (GAsPVDF) polymers which could be promising multi-functional materials. Poly(vinylidene fluoride) (PVDF) has been widely used as functional or structural material in water-proof layers,

*Corresponding author, e-mail: mmzheng@polyu.edu.hk

sensors, transducers and actuators. PVDF is a semi-crystalline polymer and is typically brittle. When it is used for piezoelectric or pyroelectric applications, the desirable content of polar crystalline β phase in PVDF has to be developed through mechanical deformation or electrical poling, and is difficult to be controlled. Hence, PVDF polymers used as sensors or actuators are typically micro-sized thin films and bulk PVDF is usually not much useful in piezoelectric and pyroelectric applications. Besides their high mechanical strength, excellent compressibility and ductility, a hybrid structure of GA and PVDF films is expected to exhibit superior dielectric, piezoelectric and pyroelectric properties because of the ultra-high surface areas of the adsorbed thin PVDF films, and could be better functional materials as compared to GA and PVDF [11]. Although functionalization of GA with oxides, polymers and metals has been reported in previous studies [12–16], this work is the first attempt in engineering GA with dielectric and ferroelectric materials. The bulk GA functionalized with PVDF films could exhibit superior combined mechanical and electro-mechanical properties and is versatile for various functional applications.

Although the GAs exhibit great hydrophobicity because of their intrinsically large surface area and non-polar carbon structure, for organic solvents and oils, they have excellent adsorption capacity and ultrafast absorption rate. Based on these features, GAs can be immersed in organic solvent to form composite structures with other functional materials. In this work, we synthesize GAsPVDF multi-functional materials via immersing GA in organic solutions of PVDF. Since the $–CH_2$ and $–CF_2$ groups in PVDF are active toward some functional molecular groups which exist more or less in GA (usually reduced graphene oxides or RGO), it is expected that the main chains of PVDF are attracted to the graphene sheets in GA. On the other hand, blending of PVDF with graphene oxides (GOs) in organic solution has been found to result in a PVDF-GO nanocomposite with enhanced ferroelectric and pyroelectric properties [17, 18]. In the formation of GAsPVDF, we add GOs into the organic solution of PVDF where GA is immersed. GOs could not only act as surfactants of GA but also facilitate the coating of PVDF-GO nanocomposites with enhanced piezoelectric and ferroelectric properties on the graphene nano-sheets. Comparative studies are carried out to investigate the mechanical and electro-mechanical properties of GAsPVDF samples prepared with and without GO blending of PVDF solutions. X-ray diffraction (XRD), scanning electron microscopy (SEM), Fourier-transform infra-red (FTIR) and Raman spectroscopy are used to analyze the structural properties of the GAsPVDF samples prepared by different methods. Samples are tested under compression to characterize their mechanical properties. The relation between the compressive strain and electrical resistance of GAsPVDF are measured to characterize the electro-mechanical properties of the samples. The effects of graphene and GO sheets on the formation of PVDF films inside GA are analyzed using anelastic mechanical relaxation, which is effective in analyzing the interaction between the nano-fillers (PVDF) and the porous matrix (GA) [19]. The interaction between the functional molecular groups in GAs or GOs and $–CF_2$ groups in PVDF is characterized to elucidate the atomistic behaviors of the graphene-PVDF hybrid structures inside GAs.

2. Experimental methods

GOs were chemically exfoliated from natural graphite flakes via a modified Hummers method [20]. Graphite flakes (5.0 g) (CP, Aladdin Reagent Database Inc., Shanghai, China) and sodium nitrates (2.5 g) (CP, Aladdin Reagent Database Inc., Shanghai, China) were added into concentrated sulfuric acid (115 mL) at room temperature. After soaking in ice bath for 25 mins with mild agitation, potassium permanganate (15.0 g) (CP, Aladdin Reagent Database Inc., Shanghai, China) was added gradually into the mixture. Then, the mixed suspension was heated to 35 °C and kept for 45 min. Deionized water (230 mL) was added and the temperature of the solution was kept at 98 °C for 45 mins. When the brown mixture turned into yellow, the mixture solution was diluted to 700 mL, followed by adding 30 mL H_2O_2 (30%). The mixture was then filtered and washed with 50 mL of HCl solution (9%). Finally, the solution was centrifuged for several times at 11 000 rpm until the pH of the system was about 7. The resulting sample was dried in vacuum at 60 °C for 72 h.

GO solution of 2 $mg \cdot mL^{-1}$ was prepared by the sonication of 2.2 g graphite oxide in 1 L water for about 2 hours. The aggregates were then removed by mild centrifugation (3000 rpm for 10 mins). Graphene hy-

drogels (GHs) were fabricated by a typical hydrothermal method. 2 mg·mL^{-1} of GO solution was put in a Teflon-lined stainless-steel autoclave, sealed, and hydrothermally treated at 180 °C for 20 h to obtain GH. Then GH was further hydrothermally treated in ammonia solution at 90 °C for 1 h. After freeze drying, the cylindrical GA with a typical height of 10 mm was obtained. The diameter of the 3D graphene monoliths is 5–8 mm.

GAsPVDF samples were prepared via immersing GAs directly in N,N-dimethylformamide (DMF, Sigma-Aldrich, Shanghai, China) with different concentrations of PVDF (Sigma-Aldrich, Shanghai, China). The schematic of the preparation process is shown in Figure 1. The concentrations of PVDF in the DMF solvent are measured by the mass ratio of PVDF to DMF. The procedure of preparing GAsPVDF with GO blending in the PVDF solution is described as follows. First, the graphene oxides were dissolved in DMF with the assistance of sonication and agitation. Then the PVDF powder was added to the suspension and stirred for 8 hours. The mass ratio of PVDF to GO was kept as a constant (50:1) in the solutions with different concentrations of PVDF. Finally, the cylindrical GAs were immersed in the solutions under sonication for 3 hours and held for another 24 hours for the complete impregnation of GAs with the solution. The GAsPVDF samples were obtained after the samples were dried at 70 °C in a vacuum oven till the DMF was removed completely. The samples are denoted as GAsPVDF-GOx where x = 0.5, 1, 3 and 10% represent the concentrations of PVDF in the DMF solvent. Similar steps were carried out to prepare GAsPVDF without GO blending in the PVDF solution. The synthesized samples are denoted as GAsPVDF-x where x = 1, 2, 3 and 10% represent the concentrations of PVDF in the DMF solvent.

Functional groups and chemical bonds of the synthesized samples were determined by X-ray photoelectron spectroscopy (XPS, PHI 5000C ESCA, Perkin Elmer, Massachusetts, USA) at a base pressure of $1 \cdot 10^{-9}$ mbar. XRD patterns of the samples were taken by an X-ray diffractometer (XRD, PW3040/60, Philips, Netherlands) with nickel filtered Cu Kα radiation. The microstructures of samples were investigated by Scanning Electron Microscopy (SEM, JSM-6490, JEOL Inc., Peabody, USA) which was equipped with energy dispersive X-ray (EDX) analysis and was operated at 20 kV. FT-IR spectra were recorded by an FT-IR spectrophotometer (Spectrum 100, Perkin Elmer, Massachusetts, USA) with a resolution of 1.0 cm^{-1}. Raman experiments were carried out on a Raman Station (Model 400/400F, Perkin Elmer, Massachusetts, USA) with a resolution of 1.0 cm^{-1}.

The compressive curves of the samples were measured by a compression testing machine (Materials Testing Z2.5TH, Zwick Techonology & Instrument Co. Ltd, Shanghai, China). The samples were pol-

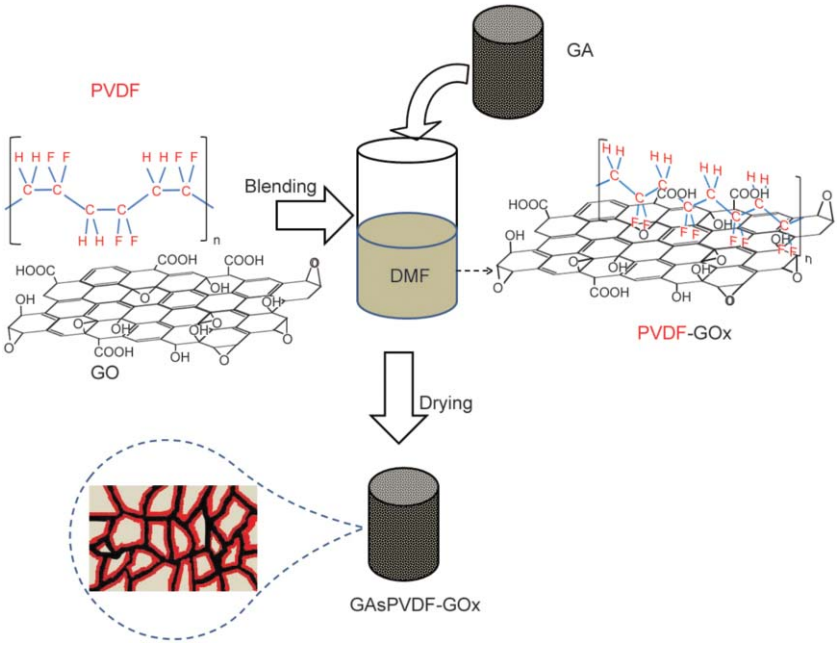

Figure 1. Schematic of preparation of GAsPVDF-GOx from PVDF solution with GO blending. The microstructures of the resulting GAsPVDF-GOx samples are illustrated as PVDF films (in red) coated at the graphene sheets (in black)

ished into a cylindrical shape with a height of 8 mm and a diameter of 4 mm. The compressive strain rate was 0.02 min^{-1}. Samples with the same dimensions were used for electrical resistance measurement under compression. Silver-paste layers with a thickness of 0.1 mm were coated at the top and bottom surfaces of the samples to form electrodes. The ferroelectric test system (TF2000E, aixACCT, Aachen, Germany) under the leakage current measuring mode was used to measure the currents of the sample under the applied voltages of 0–2 V. The electrical resistance was calculated from the Ohm's law.

Mechanical relaxation of graphene sheets and graphene-PVDF interfaces in GAsPVDF samples were characterized using a Dynamic Mechanical Analyzer (DMA, Q800, TA Instruments, Minneapolis, USA). The samples were polished into a cylindrical shape with a height of 10 mm and a diameter of 5 mm and were tested in a compression mode of dynamic mechanical analysis. The sinusoidal strain with an amplitude of 0.3% at various frequencies were applied to the samples. The anelastic relaxation behaviors of the samples between 50 and –150 °C were measured. The cooling rate is 0.6 °C/min.

3. Results and discussion

3.1. Characterizations of GA supported poly(vinylidene fluoride)

SEM images of the GAsPVDF-GOx samples are shown in Figure 2. In the preparation of GAsPVDF-GOx with low concentrations of PVDF (x = 0.5 and 1%), a relatively small amount of PVDF and GOs are dissolved in the DMF solvent. Since the solution is a very dilute liquid and there is strong interaction between PVDF and GO, PVDF tends to form particulates with GOs rather than coatings on the graphene sheets inside GAs. As shown in the SEM images (Figure 2a, b), small PVDF-GO particles only cover surfaces of the graphene sheets inside GAs. With increasing PVDF and GO contents in the DMF solvent (x = 3 and 10%), the PVDF solution becomes more viscous and more PVDF and GO are absorbed into GAs. As shown in Figure 2c, d, film-like PVDF is adsorbed much easier into GAs immersed in the viscous PVDF solution. The red arrows in Figure 2d are used to estimate the thickness of PVDF-absorbed graphene nanosheets, which is about 90 nm. Thus it can be determined that the thickness of PVDF films in the GAsPVDF-GO10% sample could be smaller than 100 nm. EDX analysis is used to determine the molar fraction of F atoms relative to the total atoms (C, O, F) in the GAsPVDF-GOx samples. Table 1 shows the relation between x and the molar fraction of F atom which could be proportional to the PVDF content in GA. The PVDF content of GAsPVDF-GOx is found to increase with increasing PVDF concentration of the solution.

Table 1. Molar fraction of F atoms in GAsPVDF-GOx samples determined from XPS and EDX analyses

	x = 0.5%	x = 1%	x = 3%	x = 10%
XPS	0.098±0.001	0.102±0.001	0.144±0.001	0.212±0.001
EDX	0.083±0.005	0.097±0.005	0.146±0.005	0.209±0.005

SEM images of the GAsPVDF-x samples are shown in Figure 3. The PVDF forms a network structure based on the architecture of graphene aerogel. The concentration of PVDF solution (x = 1, 2, 3, 10%) does not much affect the morphology of PVDF formed inside GAs. The thickness of PVDF is found to be much thicker than that of GAsPVDF-GOx. Comparison on the SEM images of GA (Figure 2e), GAsPVDF-GO10% (Figure 2d) and GAsPVDF-10% (Figure 3d), demonstrates that GO blending in the PVDF solution facilitates the formation of uniform and thin PVDF coatings on the graphene sheets inside GA.

XPS spectrum shown in Figure 4 indicates that the GAsPVDF-GOx samples have a predominant F 1s peak at around 663 eV. The content of PVDF in the GAsPVDF-GOx samples could be characterized by the molar fraction of F atoms in the samples consisting of C, O and F atoms. As listed in Table 1, it is found that the molar fraction of F atoms in the GAsPVDF-GOx sample determined by XPS increases with increasing concentration of PVDF in the solution and is close to that determined by EDX, especially in the GAsPVDF-GOx samples with x > 1%. The quantitative comparison on the molar fractions of F atoms determined by EDX and XPS suggests that the PVDF thin films could be coated uniformly on the graphene sheets in the GAsPVDF-GOx samples.

XRD patterns of the GAsPVDF samples prepared from PVDF solution with and without GO blending are shown in Figure 5. The intensities of the XRD peaks at 20.4° corresponding to the (110) planes of

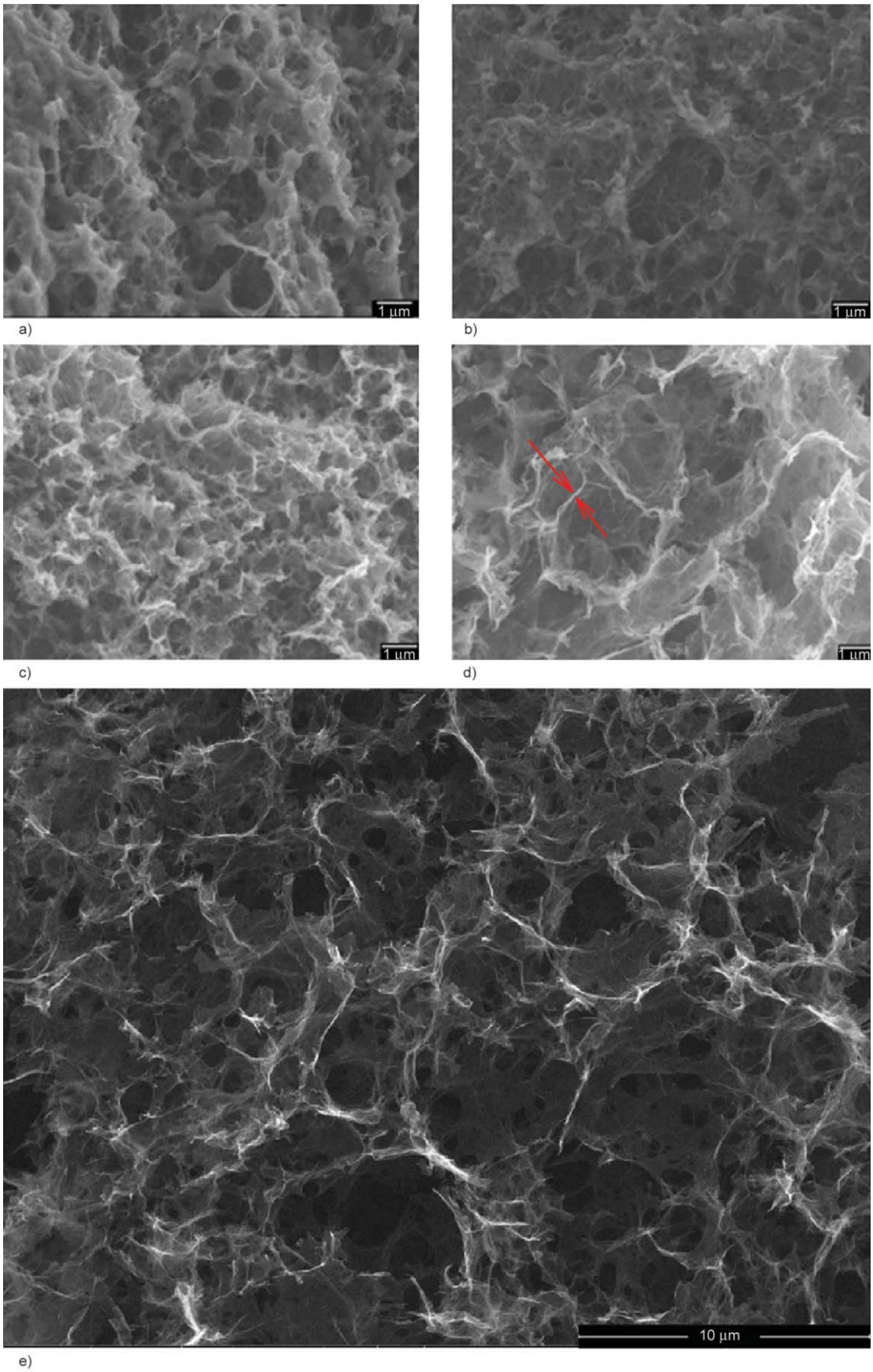

Figure 2. SEM images of GAsPVDF-GOx samples prepared from PVDF solution with GO blending. (a)–(d): x = 0.5, 1, 3, 10%, respectively. (e) GA. The arrows in (d) are used to estimate the thickness of PVDF-absorbed graphene nanosheets.

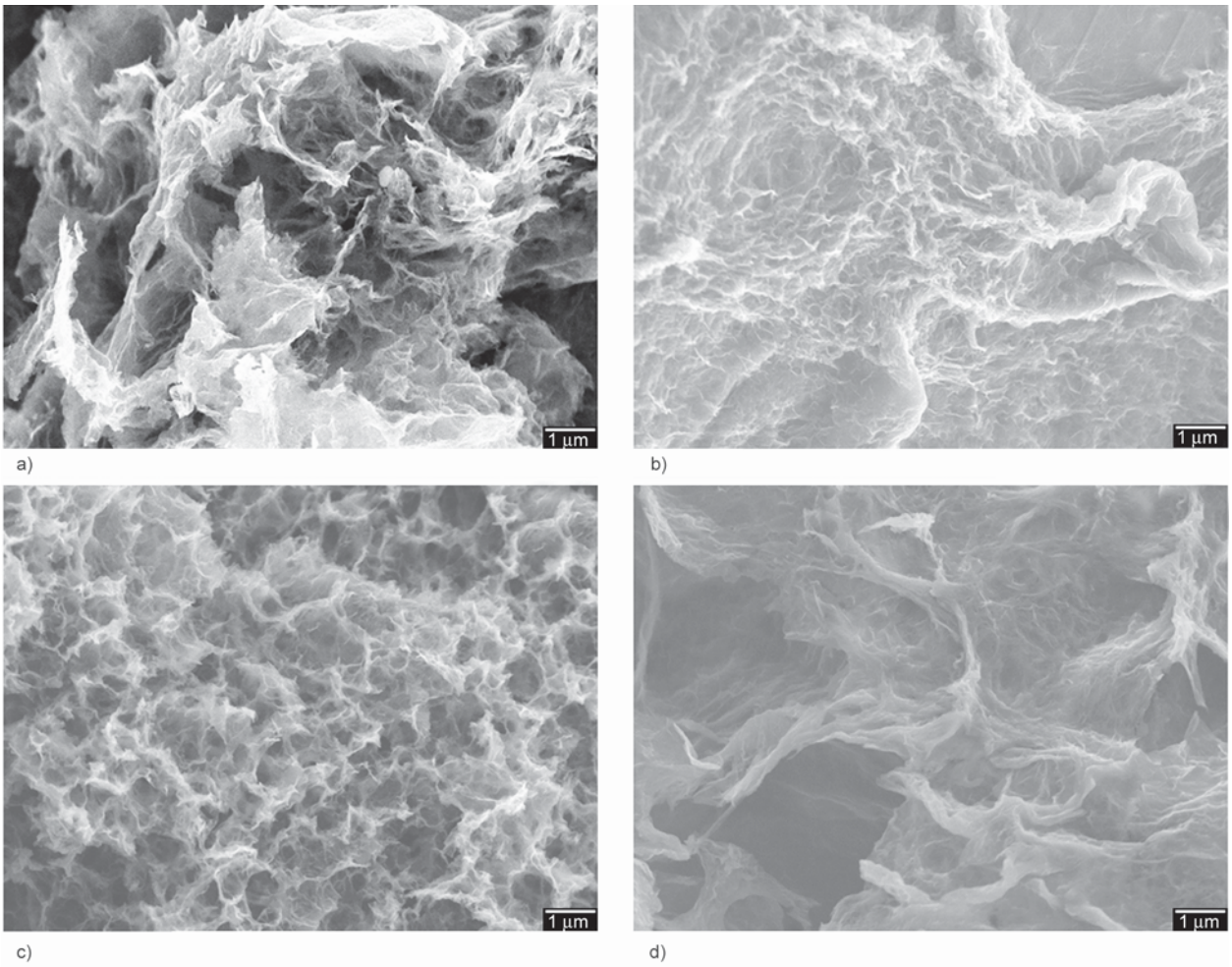

Figure 3. SEM images of GAsPVDF-x samples prepared from PVDF solution without GO blending. (a) x = 1%; (b) x = 2%; (c) x = 3%; (d) x = 10%.

the crystalline β phase of PVDF increase with increasing PVDF content x. Furthermore, the GAsPVDF-GOx samples are found to have stronger (110) peak of PVDF β phase (relative to the (001) peak of GA at 24.6°) than that of the GAsPVDF-x samples.

FTIR spectra of the GAsPVDF-GOx samples prepared from PVDF solution with GO blending are shown in Figure 6a. The IR transmittance peak at 839 cm^{-1} characterizes the presence of the β-polymorph phase in PVDF. In the β conformation of PVDF, fluorine and hydrogen atoms are on opposite sides of the main molecule chains and hence the net non-zero dipole moments are formed. With increasing content of PVDF, the transmission intensity at 839 cm^{-1} becomes stronger, demonstrating that the crystalline β phase of PVDF could increase with increasing concentration of PVDF.

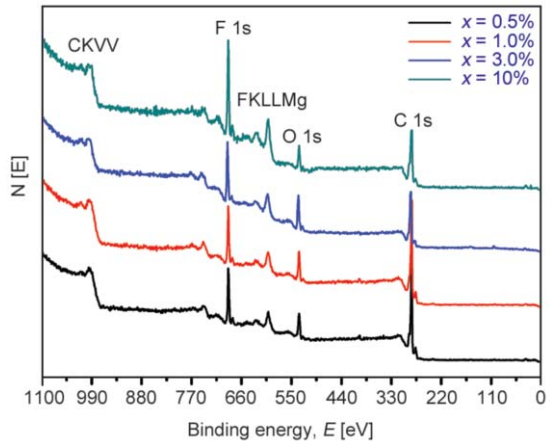

Figure 4. XPS survey scan of GAsPVDF-GOx samples

Raman spectra of the GAsPVDF-GOx samples prepared from PVDF solution with GO blending are shown in Figure 6b. The D-band (1327 cm^{-1}) represents the defects in the graphene or amorphous carbon; the G-band (1593 cm^{-1}) is caused by the in-plane vibration of graphite with an E_{2g}-symmetry intra-layer mode. The intensity ratio of G-band to D-bands (I_G/I_D) is much higher in GAsPVDF-GO10% than any other samples, suggesting that the defective carbon structures in GAsPVDF-GOx are repaired

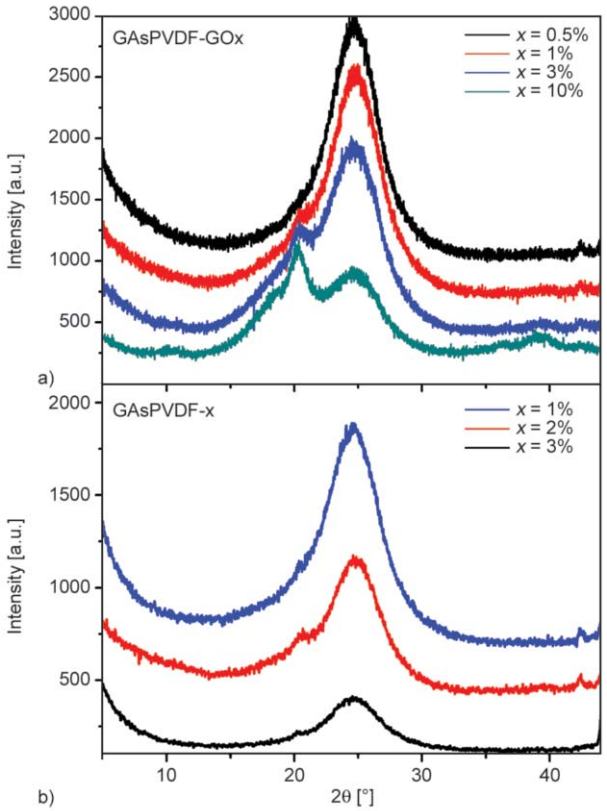

Figure 5. XRD patterns of (a) GAsPVDF-GOx, and (b) GAsPVDF-x samples

due to the attachments of the $–CF_2$ groups of PVDF on the graphene sheets, as illustrated in Figure 1. Therefore the Raman spectra further demonstrate that in the GAsPVDF-GOx samples PVDF is well coated on the RGO or GO sheets inside GAs.

It is well known that the PVDF crystalline β phase has excellent piezoelectric and pyroelectric properties [18]. From the characterizations described above, GAsPVDF-GOx prepared from PVDF solution with GO blending obviously have better quality of PVDF coating for piezoelectric and pyroelectric applications. The formation of well coated PVDF films on the graphene sheets in the GAsPVDF-GOx sample can be explained as follows: First, because the GOs are abundant of –C=O groups, and GOs and GA exhibit high affinity, therefore the strong interaction between –C=O groups in GOs and $–CF_2$ groups in PVDF drives the PVDF to lay on the graphene sheets inside GA. Second, such interaction promotes the ordering of $–CF_2$ groups in PVDF, resulting in the PVDF films uniformly coated on the graphene sheets inside GAs. Therefore GOs are not only surfactants of GA but also blending elements of PVDF which improve the piezoelectric and ferroelectric properties of PVDF. Interestingly, it has been observed that GOs in de-ionized water actually deteriorate the 3D graphene structures of GA, instead of acting as a surfactant of GA when it is in DMF. Therefore, it is suggested that GO and PVDF first form a nanocomposite which could relieve the oxidation reaction between GO and GA.

3.2. The mechanical properties of GA supported poly(vinylidene fluoride)

Figure 7 shows the compressive curves of GAsPVDF-GOx and GAsPVDF-x samples, in comparison with that of GA shown in the inset of Figure 7a. The GAsPVDF-GOx and GAsPVDF-x samples exhibit significantly improved mechanical strength as compared with that of GA samples. Remarkably, the mechanical strength of the GAsPVDF-x samples prepared from PVDF solution without GO blending is lower than that of the GAsPVDF-GOx samples prepared from PVDF solution with GO blending, and

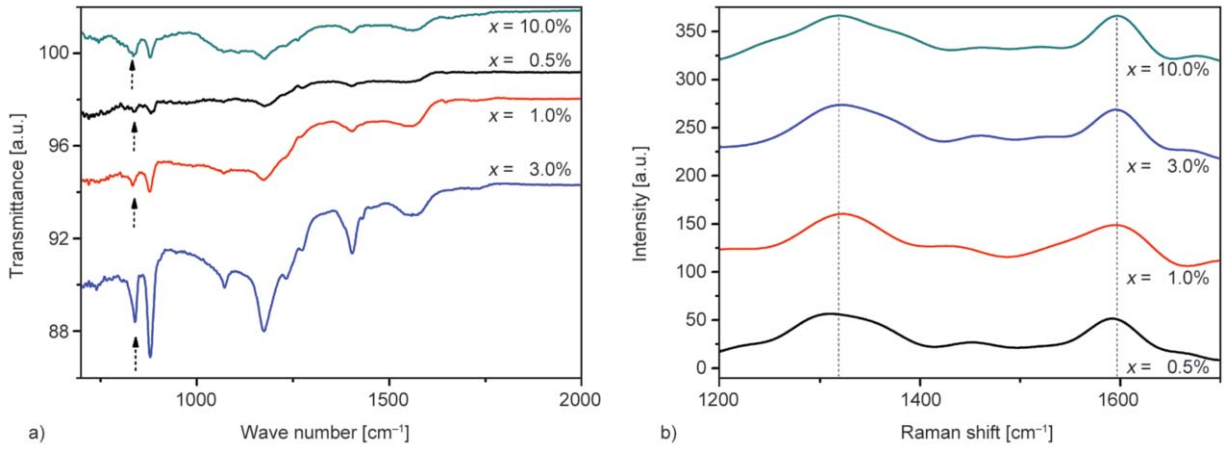

Figure 6. (a) FTIR spectra of GAsPVDF-GOx samples. The arrows indicate the IR transmission peak at 839 cm^{-1} which characterizes the PVDF crystalline beta phase. (b) Raman spectra of GAsPVDF-GOx samples.

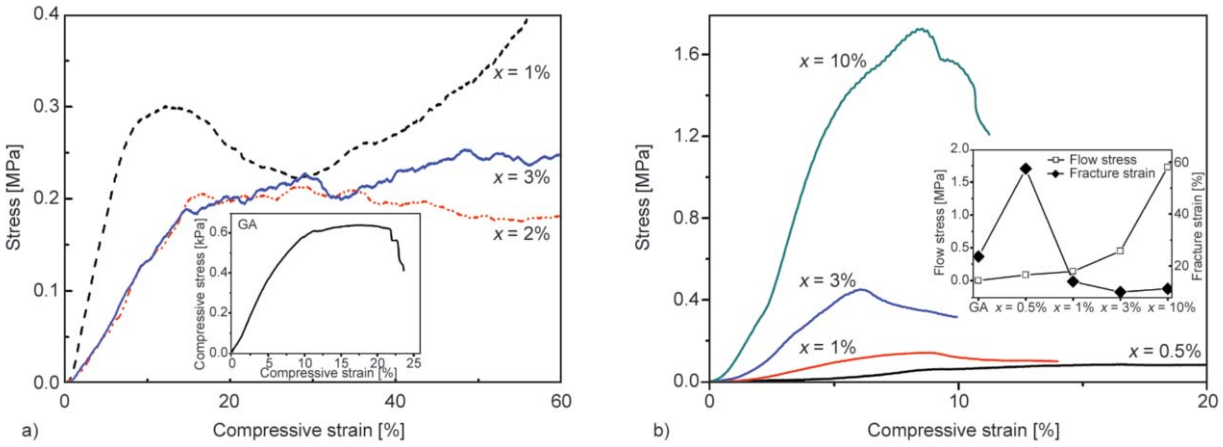

Figure 7. (a) The compressive curves of GAsPVDF-x samples; the inset is that of GA. (b) The compressive curves of GAsPVDF-GOx samples. The inset shows the flow stress and fracture strain of the samples.

is less dependent on the absorbed PVDF content x. As shown in Figure 7b, the mechanical strength of the GAsPVDF-GOx samples prepared from PVDF solution with GO blending increases significantly with increasing PVDF content, suggesting the good and firm coating of PVDF in the 3D graphene structures of GA. On the contrary, the PVDF coating on the graphene sheets in the GAsPVDF-x samples might be loose and not uniform, resulting in the low flow stress which is not much affected by the content of absorbed PVDF.

The effect of PVDF content x on the mechanical strength and ductility of GAsPVDF-GOx is significant, as shown in the inset of Figure 7b. The flow stress (0.087 MPa) and the fracture strain (57.5%) of GAsPVDF-GOx with x = 0.5% are all much higher than those of pristine GA, suggesting that the PVDF coating on the graphene sheets inside GA is effective in improving the mechanical strength and superplasticity of GA. The enhanced mechanical properties of the GAsPVDF-GOx samples prepared from PVDF solution with GO blending are attributed to the strong interaction between PVDF and GA.

3.3. The electro-mechanical properties of GA supported poly(vinylidene fluoride)

The change of electrical resistance ΔR (absolute value) of the GAsPVDF-GOx samples under applied compressive strain ε is shown in Figure 8. A linear relation between $\Delta R/R$ and ε under loading and unloading conditions can be observed. R is the electrical resistance at ε = 0 and varies from 1.5 Ω/cm^2 for GA to 0.4 MΩ/cm^2 for GAsPVDF-GO10%. The conductivities of GAsPVDF-GOx are more sensitive to

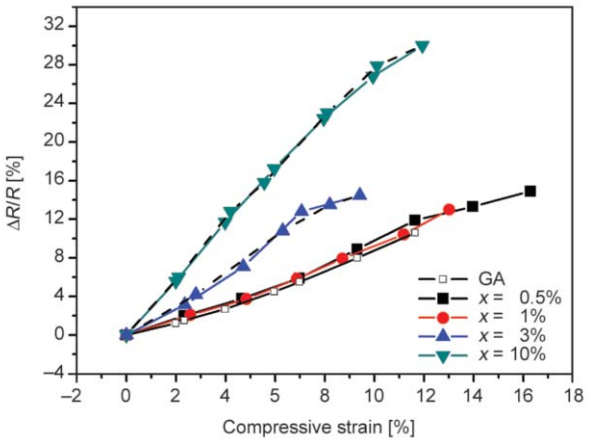

Figure 8. The relative changes of resistances $\Delta R/R$ of GAsPVDF-GOx samples (x =0.5, 1, 3 and 10%) and GA under compressive strains (in colored solid lines). The $\Delta R/R$ under the release of compression on the samples (x =3 and 10%) are plotted in black dash lines

the compressive strain than that of GA. For the GAsPVDF-GO10% sample prepared from PVDF solution with GO blending, $\Delta R/R$ is about 27% at ε = 10%, which is 2.6 times larger than that of GA. As shown in Figure 8, the conductivity of GAsPVDF-GOx with more absorbed PVDF is more sensitive to the mechanical compression.

In GA, the dependence of $\Delta R/R$ on ε is mainly caused by the weakly connected graphene sheets among which the junction areas have low conductivities. Under compression, the volume fraction of the interconnecting graphene sheets increases, resulting in the increase of conductivity with increasing compressive strains. Since the PVDF is an electrical insulator, the effect of PVDF on the relation between $\Delta R/R$ and ε for the GAsPVDF-GOx samples could be complicat-

ed. In the GAsPVDF-GOx samples with low PVDF content (x = 1, 2%), PVDF films are not likely to cover most of the surface areas of graphene sheets. Because the junctions among graphene sheets are more active toward PVDF adsorption, PVDF could be coated on those junction areas in GA, leaving the surface areas of the graphene sheets to be conductive. Since graphene sheets are much more flexible than PVDF, the compression on GAsPVDF-GOx leads to the formation of conductive paths among graphene sheets. Therefore the $\Delta R/R$ of GAsPVDF-GOx could be more sensitive to ε than that of GA where the compression leads to the formation of conductive paths at the junction areas.

It is interesting that the change of $\Delta R/R$ with respect to ε is more sensitive in the GAsPVDF-GOx samples with more PVDF content x. When the content of the adsorbed PVDF in GA is high, the PVDF films tend to cover the surfaces of graphene sheets, as demonstrated by the XPS and EDX results listed in Table 1. If the mechanism of compression-induced conductivity change is the same as those described above, the conductivity of the GAsPVDF-GOx samples with $x > 1\%$ must be less sensitive to compression compared with that of the samples with $x < 1\%$. On the contrary, the conductivities are more sensitive to compression for the GAsPVDF-GOx samples with increasing content of adsorbed PVDF ($x > 1\%$), as shown in Figure 8. Therefore, the strain-dependent conductivity of the GAsPVDF-GOx samples could not be associated with the compression-induced interconnecting graphene sheets. As discussed in Sec. 3.1, PVDF adsorbed in GA should be piezoelectric because it possesses large volume fraction of crystalline polar crystalline phase. The applied compressive strain could induce polarization and net charges on the electrodes of the GAsPVDF-GOx samples. In the measurement of electrical resistance, there are additional dipolar currents generated by the applied strain besides those caused by the applied voltage. Therefore, the $\Delta R/R$ of the GAsPVDF-GOx samples changes more significantly with the applied strain in comparison with that of GA, and the conductivity is more sensitive to compression in the GAsPVDF-GOx samples with more PVDF content x.

3.4. Anelastic analysis on the interfaces between GA and PVDF

Anelastic mechanical relaxation of GAsPVDF-GOx and GAsPVDF-x samples are measured to further elucidate the effect of PVDF on the microstructural features and the mechanical properties of GAs. Under the applied periodic stresses, the anelastic responses of graphene nano-sheets, amorphous and crystalline regions of PVDF films, and those molecular groups at the interfaces between GA and PVDF can be well characterized by the mechanical loss and dynamical modulus. Figure 9 shows the storage modulus and mechanical loss (tan δ) of GA monoliths used for the

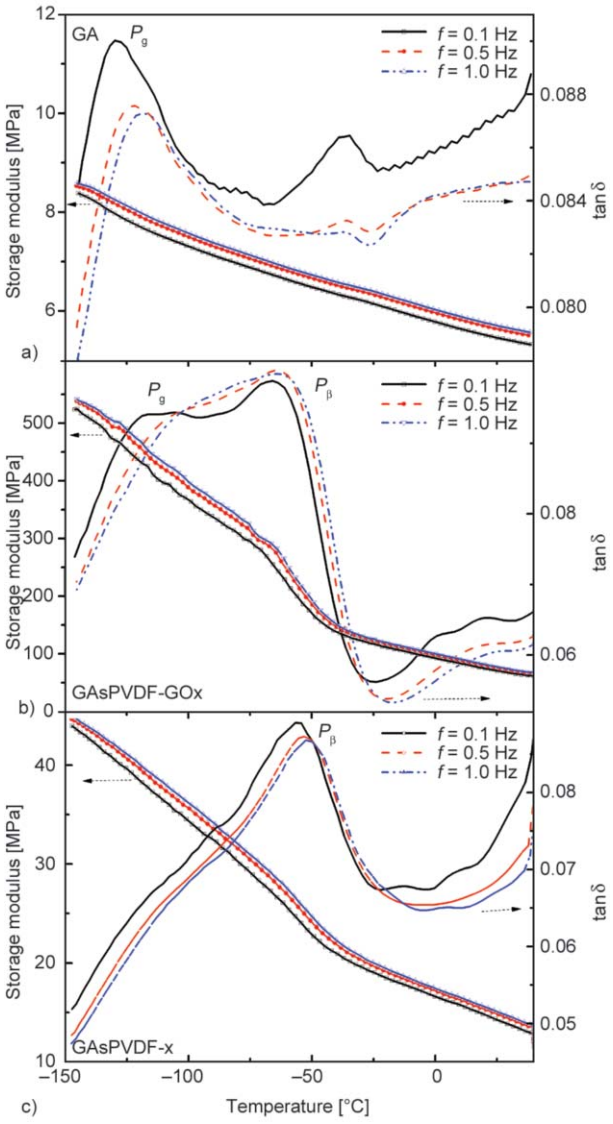

Figure 9. The storage modulus and mechanical losses (tan δ) of (a) GA, (b) GAsPVDF-GO10%, and (c) GAsPVDF-10% samples at various frequencies f.

preparation of GAsPVDF, GAsPVDF-GOx and GAsPVDF-x samples, respectively. The 3D graphene structure in GA is mostly characterized by the tan δ peak (labeled as P_g) at –130 ~ –120 °C depending on the testing frequency, which is of relaxation type as shown in Figure 9a. The activation energy of relaxation E_a can be well determined by the Arrhenius relation (Equation (1)):

$$f = f_0 \exp\left(\frac{-E_a}{k_B T}\right) \quad (1)$$

where f is the test frequency, f_0 is the attempt frequency of the diffusion of atoms and T is the peak temperature of P_g peak. k_B is the Boltzmann constant. Figure 10a shows the fits of ln$f$ and 1/T based on Equation (1). E_a and f_0 are determined to be 0.38 eV and $2.8 \cdot 10^{11}$ s^{-1}, respectively. Because the low activation energy E_a is close to that of two-dimensional diffusion of carbon atoms [21], it is suggested that the P_g peak could be related to the relaxation of defective carbon atoms on the graphene sheets in GAs. Considering the nano-porous features of 3D graphene monolith, the relaxation nature of such tan δ peak implies that it is caused by the relaxation of the inter-connecting junction areas of graphene sheets in GA where defective carbon atoms exist.

The mechanical losses of GAsPVDF-GO10% and GAsPVDF-10% samples are much increased as compared with that of GA. The presence of PVDF films in these samples is much evident from a broad β relaxation peak at –55 ~ –30 °C (labeled as P_β), which is caused by the Brownian motions of amorphous PVDF [22]. In GAsPVDF-10% samples prepared from PVDF solution without GO blending the P_β peak seems to overwhelm the characteristic P_g peak of GA. However, in GAsPVDF-GO10% samples prepared from PVDF solution with GO blending the P_β peak of PVDF does not affect much the characteristic P_g peak of GA. It is thus suggested that in GAsPVDF-GO10% samples prepared from PVDF solution with GO blending the 3D graphene microstructures are mostly preserved since PVDF is coated on the graphene sheets; while in GAsPVDF-10% samples prepared from PVDF solution without GO blending the 3D graphene microstructures might be damaged by the PVDF deposited at the junction areas of the graphene sheets. In the GAsPVDF-10% samples amorphous PVDF polymer is dominant in the graphene-PVDF hybrid structures at the inter-connecting regions of GAs.

Unlike those caused by the diffusions of defective carbon atoms, the mechanical relaxation of amorphous structures (β relaxation) in PVDF cannot be characterized by the Arrhenius relation. Instead the β relaxation is typically characterized by the Vogel-Fulcher-Tammann (VFT) relation as shown by Equation (2):

$$f = f_0 \exp\left[\frac{-E_a}{k_B (T - T_0)}\right] \quad (2)$$

where T is the peak temperature of P_β peak. T_0 represents the Kauzmann temperature or static freezing temperature which is far below the glass transition temperature. Figure 10b shows the fits of ln$f$ and $1/(T - T_0)$ based on Equation (2). T_0 = –140 °C is chosen for the fits. The apparent activation energy E_a of

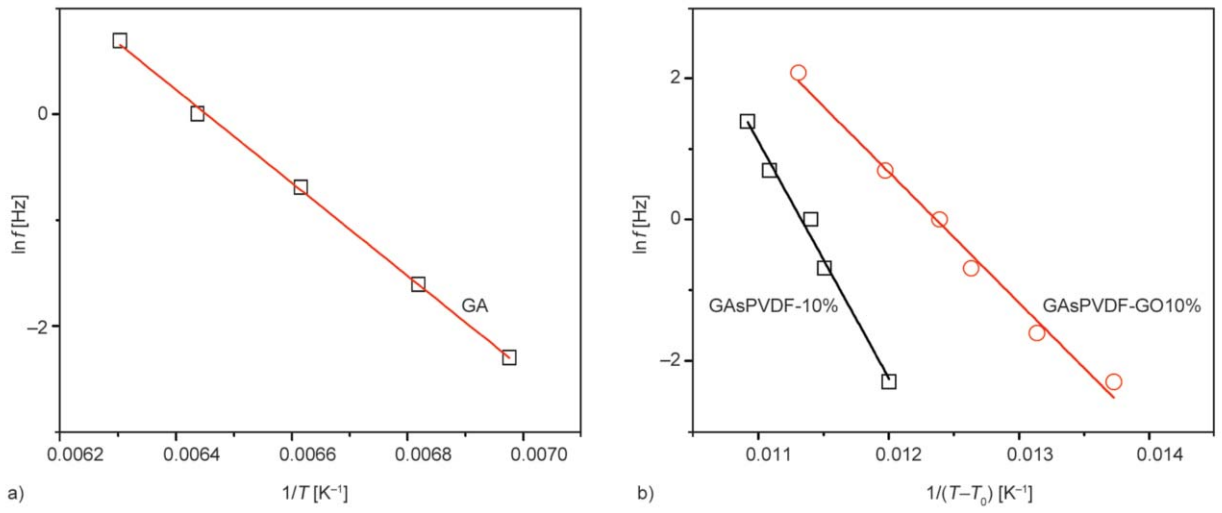

Figure 10. (a) The Arrhenius plots for the P_g peak in GAs. (b) Determination of the apparent activation energy of β relaxation using the VFT relation.

β relaxation for the GAsPVDF-GO10% and GAsPVDF-10% samples is 0.16 eV and 0.29 eV, respectively. Because E_a of β relaxation for the GAsPVDF-GO10% sample is consistent with that (~0.15 eV) for PVDF-GO composite films [23] and is different with that (~0.09 eV) for pure PVDF films [18], it is envisaged that GOs are incorporated into the PVDF films in GAsPVDF-GO10% samples. Since the additions of GOs in PVDF enhance the polar crystalline phase of PVDF [17, 18, 23], the films in GAsPVDF-GOx samples have less amorphous structures than those in GAsPVDF-x samples. Comparison between the P_β peak temperatures for the GAsPVDF-GO10% samples and the GAsPVDF-10% samples could provide further evidence, as shown in Figure 9b and 9c, respectively. Nevertheless, E_a of β relaxation for the GAsPVDF-10% samples is much larger than that for the GAsPVDF-GO10% samples, demonstrating the high content of amorphous structures in PVDF which prevents the formation of well coated PVDF films on the graphene surfaces in GAs, as shown in Figure 10b.

4. Conclusions

Graphene aerogel supported poly(vinylidene fluoride) samples were synthesized. The blending of GOs with PVDF solutions facilitates the formation of thin and uniform PVDF films whose typical thickness is below 100 nm on the graphene sheets inside GAs. The graphene aerogel supported poly(vinylidene fluoride) has high content of crystalline β phase which possesses pyroelectricity and piezoelectricity. With increasing contents of PVDF and crystalline PVDF β phase, the graphene aerogel supported poly(vinylidene fluoride) samples exhibit significantly improved mechanical and electro-mechanical properties as compared to those of GAs, suggesting that they could be used as multi-functional materials such as high-performance sensors, actuators and kinetic energy harvesters. The superior combined mechanical and electro-mechanical properties of graphene aerogel supported poly(vinylidene fluoride) are attributed to the strong interaction between the –C=O groups in GAs or GOs and the $–CF_2$ groups in PVDF.

Acknowledgements

The authors are grateful for the supports provided by the Science and Technology Innovation Commission of Shenzhen (No. JCYJ2013041152508657), and the Program for Eastern Scholar at Shanghai Institutions of Higher Learning.

References

[1] Hu H., Zhao Z., Wan W., Gogotsi Y., Qiu J.: Ultralight and highly compressible graphene aerogels. Advanced Materials, **25**, 2219–2223 (2013). DOI: 10.1002/adma.201204530

[2] Sun H., Xu Z., Gao C.: Multifunctional, ultra-flyweight, synergistically assembled carbon aerogels. Advanced Materials, **25**, 2554–2560 (2013). DOI: 10.1002/adma.201204576

[3] Ito Y., Tanabe Y., Qiu H. J., Sugawara K., Heguri S., Tu N. H., Huynh K. K., Fujita T., Takahashi T., Tanigaki K., Chen M. W.: High-quality three-dimensional nanoporous graphene. Angewandte Chemie, **126**, 4922–4926 (2014). DOI: 10.1002/ange.201402662

[4] Biener J., Dasgupta S., Shao L., Wang D., Worsley M. A., Wittstock A., Lee J. R., Biener M. M., Orme C. A., Kucheyev S. O., Wood B. C., Willey T. M., Hamza A. V., Weissmüller J., Hahn H., Baumann T. F.: Macroscopic 3D nanographene with dynamically tunable bulk properties. Advanced Materials, **24**, 5083–5087 (2012). DOI: 10.1002/adma.201202289

[5] Gui X., Cao W., Wei J., Li H., Jia Y., Li Z., Fan L., Wang K., Zhu H., Wu D.: Soft, highly conductive nanotube sponges and composites with controlled compressibility. ACS Nano, **4**, 2320–2326 (2010). DOI: 10.1021/nn100114d

[6] Zhang X., Sui Z., Xu B., Yue S., Luo Y., Zhan W., Liu B.: Mechanically strong and highly conductive graphene aerogel and its use as electrodes for electrochemical power source. Journal of Materials Chemistry, **21**, 6494–6497 (2011). DOI: 10.1039/C1JM10239G

[7] Feng W., Yan L.: *In situ* self-assembly of mild chemical reduction graphene for three-dimensional architectures. Nanoscale, **3**, 3132–3137 (2011). DOI: 10.1039/C1NR10355E

[8] Qiu L., Liu J. Z., Chang S. L. Y., Wu Y., Li D.: Biomimetic superelastic graphene-based cellular monoliths. Nature Communications, **3**, 1241/1–1241/7 (2012). DOI: 10.1038/ncomms2251

[9] Hodlur R. M., Rabinal M. K.: Self assembled graphene layers on polyurethane foam as a highly pressure sensitive conducting composite. Composites Science and Technology, **90**, 160–165 (2014). DOI: 10.1016/j.compscitech.2013.11.005

[10] Kuang J., Liu L., Gao Y., Zhou D., Chen Z., Han B., Zhang Z.: A hierarchically structured graphene foam and its potential as a large-scale strain-gauge sensor. Nanoscale, **5**, 12171–12177 (2013).
DOI: 10.1039/C3NR03379A

[11] Rahman M. A., Lee B. C., Phan D. T., Chung G. S.: Fabrication and characterization of highly efficient flexible energy harvesters using PVDF–graphene nanocomposites. Smart Materials and Structures, **22**, 085017/1–085017/5 (2013).
DOI: 10.1088/0964-1726/22/8/085017

[12] Cong H-P., Ren X-C., Wang P., Yu S-H.: Macroscopic multifunctional graphene-based hydrogels and aerogels by a metal ion induced self-assembly process. ACS Nano, **6**, 2693–2703 (2012).
DOI: 10.1021/nn300082k

[13] Hu H., Zhao Z., Zhang R., Bin Y., Qiu J.: Polymer casting of ultralight graphene aerogels for the production of conductive nanocomposites with low filling content. Journal of Materials Chemistry A, **2**, 3456–3760 (2014).
DOI: 10.1039/C3TA14840H

[14] Hu H., Zhao Z., Wan W., Gogotsi Y., Qiu J.: Polymer/graphene hybrid aerogel with high compressibility, conductivity, and 'sticky' superhydrophobicity. ACS Applied Materials and Interfaces, **6**, 3242–3249 (2014).
DOI: 10.1021/am4050647

[15] Gong Y., Yang S., Liu Z., Ma L., Vajtai R., Ajayan P. M.: Graphene-network-backboned architectures for high-performance lithium storage. Advanced Materials, **25**, 3979–3984 (2013).
DOI: 10.1002/adma.201301051

[16] Xiao L., Wu D., Han S., Huang Y., Li S., He M., Zhang F., Feng X.: Self-assembled Fe_2O_3/graphene aerogel with high lithium storage performance. ACS Applied Materials and Interfaces, **5**, 3764–3769 (2013).
DOI: 10.1021/am400387t

[17] El Achaby M., Arrakhiz F. Z., Vaudreuil S., Essassi E. M., Qaiss A.: Piezoelectric β-polymorph formation and properties enhancement in graphene oxide – PVDF nanocomposite films. Applied Surface Science, **258**, 7668–7677 (2012).
DOI: 10.1016/j.apsusc.2012.04.118

[18] Jiang Z. Y., Zheng G. P., Han Z., Liu Y. Z., Yang J. H.: Enhanced ferroelectric and pyroelectric properties of poly(vinylidene fluoride) with addition of graphene oxides. Journal of Applied Physics, **115**, 204101/1–204101/6 (2014).
DOI: 10.1063/1.4878935

[19] Ilčíková M., Mrlík M., Sedláček T., Doroshenko M., Koynov K., Danko M., Mosnáček J.: Tailoring of viscoelastic properties and light-induced actuation performance of triblock copolymer composites through surface modification of carbon nanotubes. Polymer, **72**, 368–377 (2015).
DOI: 10.1016/j.polymer.2015.03.060

[20] Han Z., Tang Z., Shen S., Zhao B., Zheng G. P., Yang J. H.: Strengthening of graphene aerogels with tunable density and high adsorption capacity towards Pb^{2+}. Scientific Reports, **4**, 5025/1–5025/6 (2014).
DOI: 10.1038/srep05025

[21] Hofmann S., Csányi G., Ferrari A. C., Payne M. C., Robertson J.: Surface diffusion: The low activation energy path for nanotube growth. Physical Review Letters, **95**, 036101/1–036101/4 (2005).
DOI: 10.1103/PhysRevLett.95.036101

[22] Callens A., Eersels L., De Batist R.: Low temperature internal friction on γ-irradiated polyvinylidene fluoride (PVDF). Journal of Materials Science, **13**, 1887–1990 (1978).
DOI: 10.1007/BF00552895

[23] Jiang Z. Y., Zheng G. P., Zhan K., Han Z., Yang J. H.: Formation of piezoelectric β-phase crystallites in poly (vinylidene fluoride)-graphene oxide nanocomposites under uniaxial tensions. Journal of Physics D: Applied Physics, **48**, 245303/1–245303/7 (2015).
DOI: 10.1088/0022-3727/48/24/245303

eXPRESS Polymer Letters Vol.10, No.9 (2016) 742–749
Available online at www.expresspolymlett.com
DOI: 10.3144/expresspolymlett.2016.68

Stress intensification – an abnormal phenomenon observed during stress relaxation of dynamic coordination polymer

N. N. Xia[1], *M. Z. Rong*[1], *M. Q. Zhang*[1*], *S.-W. Kuo*[2]

[1]Key Laboratory for Polymeric Composite and Functional Materials of Ministry of Education, GD HPPC Lab, School of Chemistry and Chemical Engineering, Sun Yat-Sen University, 510275 Guangzhou, China
[2]Department of Material and Optoelectronic Science, National Sun Yat-Sen University, 804 Kaohsiung, Taiwan

Received 14 January; accepted in revised form 28 March 2016

Abstract. The authors report that during tensile stress relaxation test of a polyurethane crosslinked by catechol-iron coordination bonds, the stress gradually increases with time after the initial drop, which differs from the documented behaviors of other materials. Based on model experiment and structural characterization, water triggered rapid increase of dynamic crosslinkages accompanied by Poisson's contraction is found to be responsible for the stress intensification effect. In addition, the influential factors are carefully discussed. The findings might help to develop novel polymeric materials with improved application performance under loading conditions.

Keywords: *smart polymers, stress relaxation, polyurethane, dynamic coordination bond, crosslink*

1. Introduction

Stress relaxation of materials used to refer to stress decrease with time under constant strain. In the case of polymers, macromolecular conformation has to be at a non-equilibrium state upon being stressed. Accordingly, movement of chain segments would take place to reduce or relieve the internal stress with increasing time.

In reality, the mechanisms involved in stress relaxation fall into five groups depending on polymer species and practical application circumstances [1, 2]: (i) chain scission (mostly because of hydrolysis or oxidative degradation), (ii) bond interchange, (iii) viscous flow (caused by slippage of linear chains), (iv) Thirion relaxation (reversible relaxation of physical crosslinks or trapped entanglements in elastomers), and (v) molecular relaxation near glass transition temperature.

From the phenomenological point of view, linear polymers can completely relax stress to zero provided time is long enough, while crosslinked polymers can only relax stress to a certain equilibrium value owing to the network confinement. However, if the crosslinked polymers are built up by reversible bonds, as revealed by recent investigation [3–9], rearrangement of the networks would be allowed when the reversible reaction is triggered. The materials also go to a lower state of energy, leading to complete relaxation of the stress.

Unlike these known behaviors, here we report stress intensification behavior appearing during stress relaxation test of a hyperbranched polyurethane (HBPU), which holds catechol and hydrophilic carboxyl end groups and is crosslinked by catechol-Fe^{3+} complexes (HBPU-DMPA-[$Fe(DOPA)_3$], DMPA = dimethylol propionic acid, DOPA = 3.4-dihydroxyphenyl-L-alanine, refer to Figure 1. That is, after the initial reduction in stress as usual, the stress gradually increases rather than decreases or levels off. Since there is no similar observation in literature, a preliminary exploration of the molecular cause for the abnormal effect

*Corresponding author, e-mail: ceszmq@mail.sysu.edu.cn

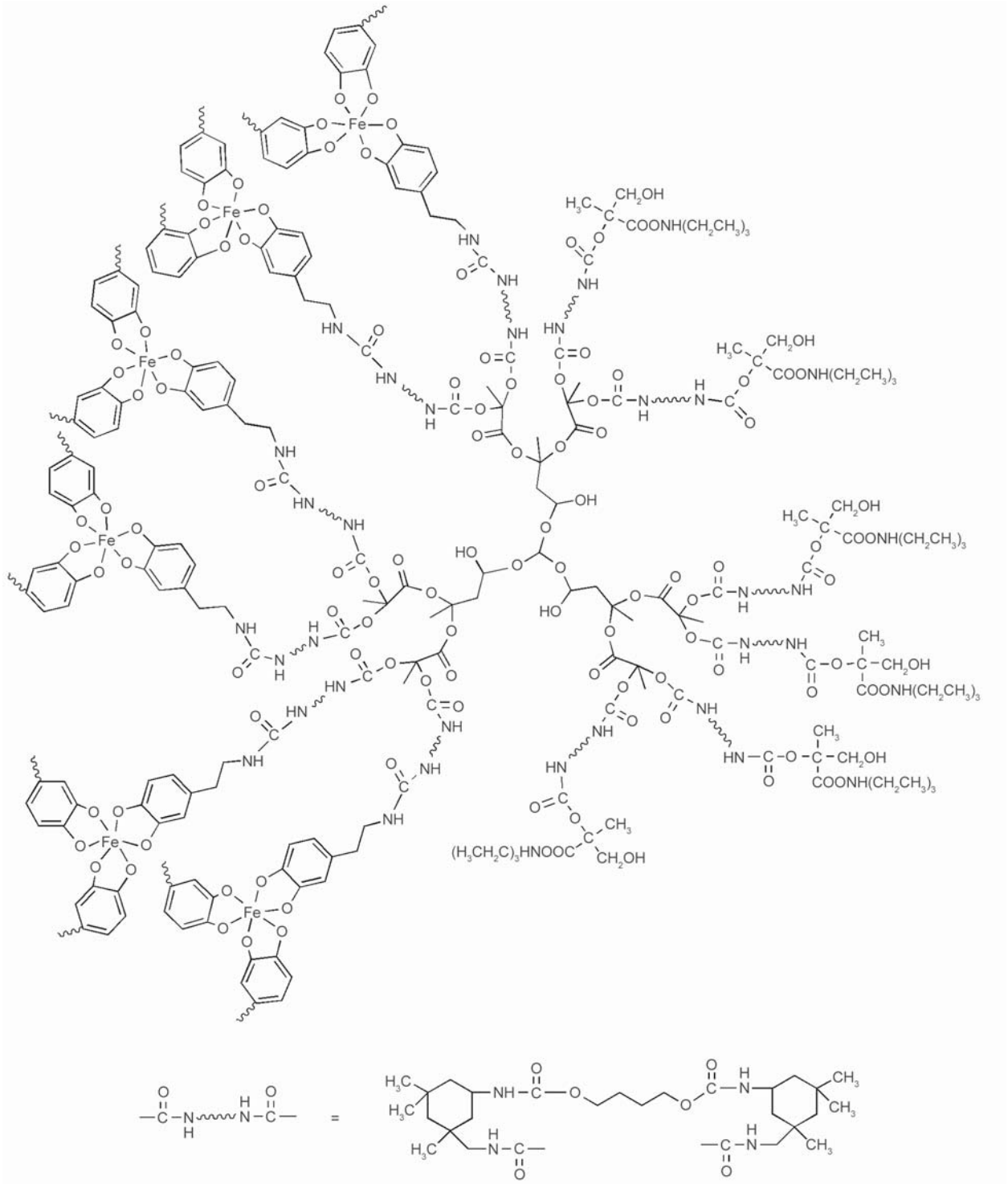

Figure 1. Structure of HBPU-DMPA-[Fe(DOPA)$_3$]. During the synthesis, hyperbranched polyester is used as the starting material, and then polyurethane prepolymer, DMPA, dopamine hydrochloride, and ferric chloride are introduced, respectively (Figure 2)

is conducted hereinafter to have an in-depth understanding. The dynamic coordination-dissociation behavior of the crosslinkages in the polymer is absent in conventional irreversibly bonded versions. It is hoped that the present work will help to carry forward this interesting property for future design, synthesize, manufacturing and application of novel materials.

2. Experimental

HBPU-DMPA-[Fe(DOPA)$_3$] with Fe^{3+}/dopamine molar ratio of 1:3 was synthesized following the pro-

cedures described in ref. [10] (Figure 2). T_g of the soft segments is –63.3 °C, while that of the hard segments is –7.5 °C, as determined by dynamic mechanical analysis (DMA) [10].

Stress relaxation was measured at 25 °C in tensile mode at a constant strain of 10% with DMA (01dB-MetraviB DMA-25N, ACOEM Group, Limonest, France). Prior to the measurement, the specimens were saturated by water with different pH values. Then, some of the specimens were directly sent for testing (called water saturated specimens hereinafter), while the rest were dried and tested (called dry specimen). During testing the water saturated specimens were wrapped by waterlogged absorbent cotton to maintain water content.

Rheological data were obtained from a strain-controlled ARG2 rheometer (TA Instruments, New Castle, USA) with 25 mm parallel-plate geometry (disk-

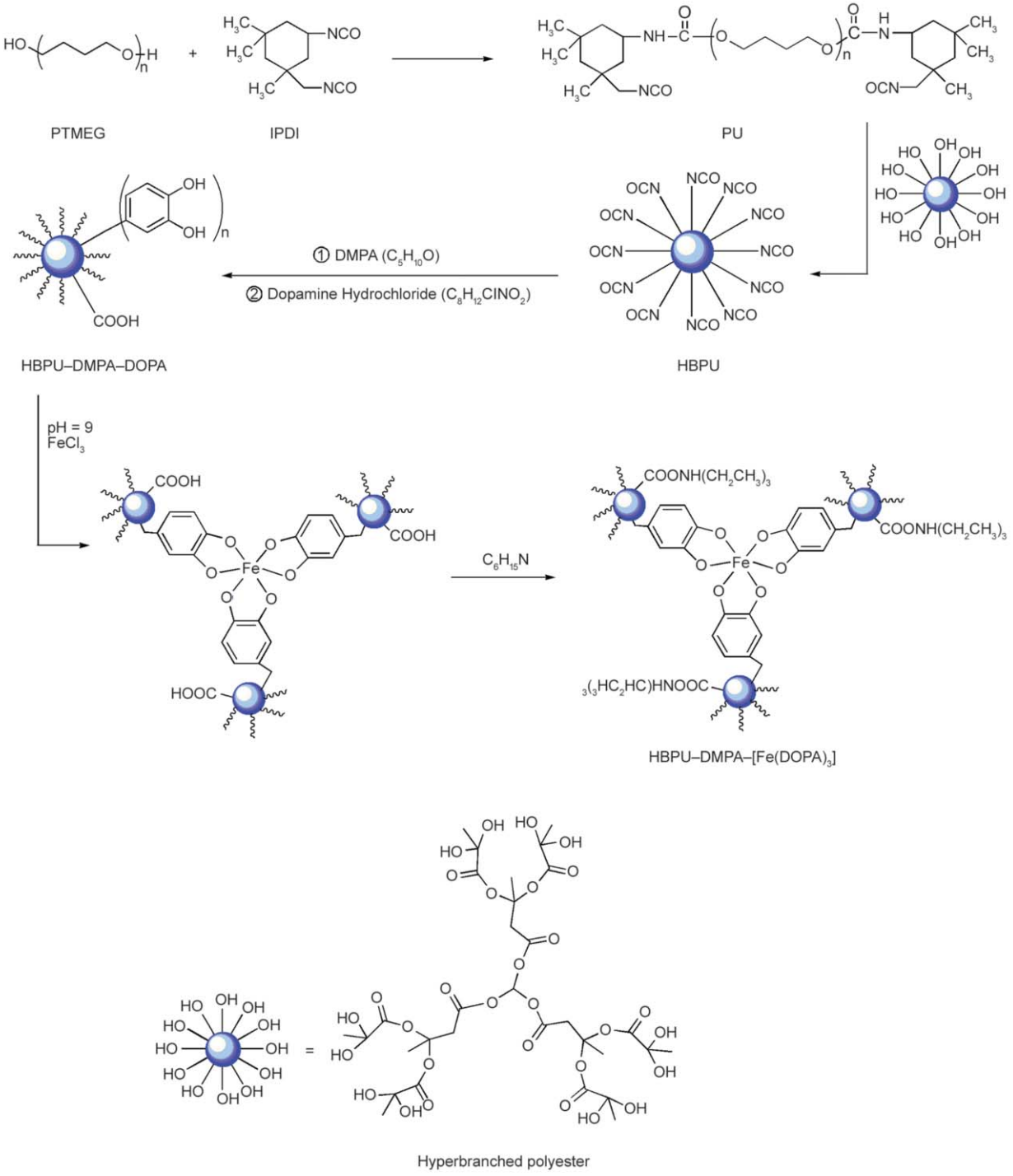

Figure 2. Synthesis of HBPU-DMPA-[Fe(DOPA)$_3$]

shaped specimens: 10 mm in diameter and 2 mm in thickness). Frequency sweeps at 0.2% strain were conducted at different temperatures.

To obtain Raman spectra of the materials subjected to volume contraction during tensile stress relaxation, disk-shaped specimens (diameter: 12 mm, thickness: 1.5 mm) were pretreated following the above procedures applied for stress relaxation, placed into a mold with round cavity (inner diameter: 12 mm) and compressed by a steel cylinder (diameter: 12 mm) under 0.6 MPa for preset time. Afterwards, Raman spectra were collected by a confocal Raman microscope (Renishaw inVia, Renishaw, Gloucestershire, UK). The diode-pumped 785 nm near infrared laser excitation was used in combination with a 20× microscope objective. The spectra were acquired using an air-cooled CCD behind a grating (300 $g \cdot mm^{-1}$) spectrograph with a spectral resolution of 4 cm^{-1}. Because the samples were sensitive to burning by the laser beam, laser power of 10 mW and exposure time of 20 s were used for all measurements. Each collected spectrum consisted of 60 accumulations of a 0.2 s integration time. For each sample, three spectra were collected from different regions and averaged.

3. Results and discussion

The polymer HBPU-DMPA-[Fe(DOPA)$_3$] was originally synthesized for developing lipophilic material capable of self-healing and recycling in seawater (pH = 8.3) [10]. Therefore, characterization of structure and properties is carried out in water as a function of pH in comparison with that in dry environment.

As shown in Figure 3, the above-mentioned stress intensification can be found under certain circumstances. More exactly, only the specimens of HBPU-DMPA-[Fe(DOPA)$_3$] saturated by water at pH = 9 and 7 exhibit the abnormal manner (Figure 3a). A simple explanation of this habit lies in stress hardening due to improvement of macromolecular chains orientation induced by tension. However, this is an apparent paradox because (i) the small strain applied during stress relaxation is barely enough for chain extension, (ii) the polymers studied here are crosslinked so that the molecular chains are unable to align preferentially along the stretching direction, and (iii) either the same polymer HBPU-DMPA-[Fe(DOPA)$_3$], which was firstly saturated by water at pH = 9 or 7 and then dried (Figure 3b), or the control HBPU-DMPA-DOPA (Figure 3c and Figure 2), behaves like conventional polymers, despite the fact that all the materials shown in Figure 3 were tested on the same conditions.

A careful examination of Figure 3 indicates that (i) water saturation and (ii) higher pH value of the water are necessary for achieving obvious stress intensification effect of HBPU-DMPA-[Fe(DOPA)$_3$]. The first issue is precisely the key factor for trigger-

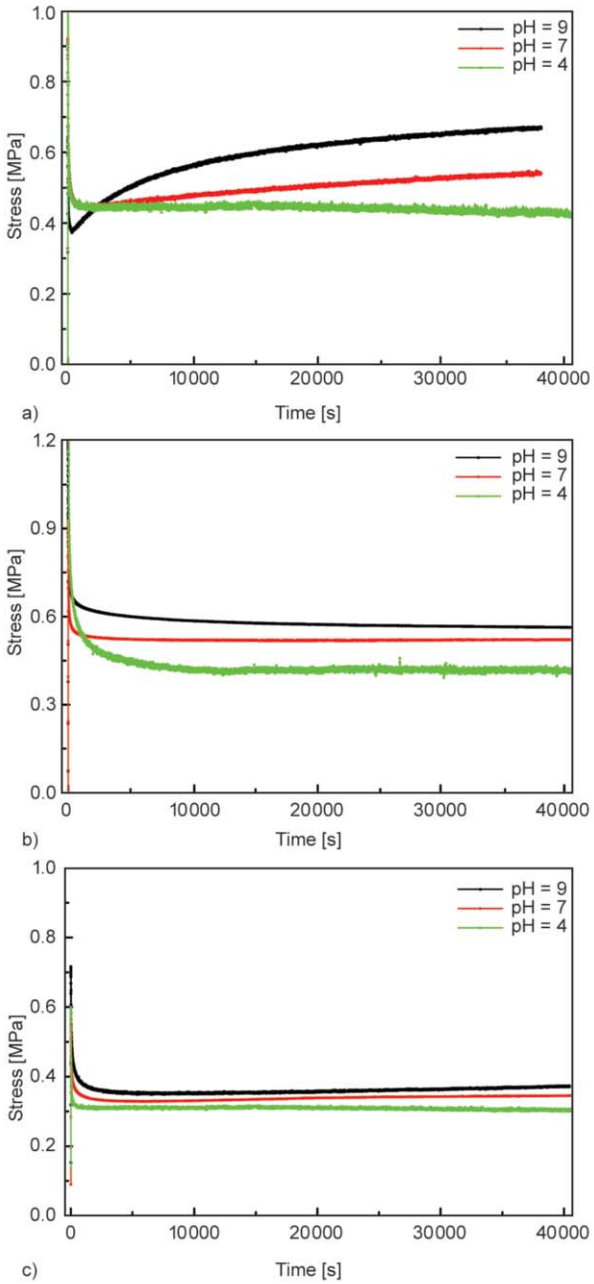

Figure 3. Tensile stress relaxation behaviors of (a) water saturated and (b) dry HBPU-DMPA-[Fe(DOPA)$_3$] as a function of pH in comparison with (c) the water saturated control HBPU-DMPA-DOPA. Temperature: 25 °C.

ing the dynamic coordinate bonds in HBPU-DMPA-[Fe(DOPA)$_3$] [10]. It has been known that when the polymer is immersed in water with different pH values (9, 7 and 4), tris-, bis- and mono-catechol-Fe^{3+} coordinations appear in the polymer network successively [11]. Higher coordination number is acquired at higher pH. Moreover, our recent investigation reveals that the DOPA-iron complexation can be triggered to a dynamic state in the presence of water and the dynamic manner is immobilized after removing water. That is, the catechol-Fe^{3+} crosslinkages of HBPU-DMPA-[Fe(DOPA)$_3$] are dynamically connected and disconnected at any time in wet environment. Accordingly, the polymer is in the dynamic equilibrium (in the presence of water) and stable state (in the absence of water), respectively.

By taking advantages of the dynamic reversible crosslinking, the network chains of HBPU-DMPA-[Fe(DOPA)$_3$] is able to be ceaselessly rearranged. As a result, the frequency dependence of storage shear modulus, G', of the water saturated specimen intersects with that of loss shear modulus, G'', suggesting a transition from elastic-like ($G' > G''$) to viscous-like ($G' < G''$) with decreasing frequency (Figure 4a). Since the disconnected networks need time to be reconnected, the system has to perform like viscous fluid at low frequency regime [12–14]. In contrast, the dry HBPU-DMPA-[Fe(DOPA)$_3$] (Figure 4b) and the control without Fe^{3+} (Figure 4c) do not exhibit the same network reconfiguration due to lack of the dynamic bonds.

Just because of existence of the dynamic reversible bonds, the crosslinked networks should be rearranged to a less stretched state upon being stressed and the water saturated HBPU-DMPA-[Fe(DOPA)$_3$] is supposed to show complete stress relaxation. However, surprisingly this behavior does not appear (Figure 3a). We believe that there must be a synergistic effect between network reshuffling and formation of catechol-Fe^{3+} crosslinks in this case. Iron ions have been known to be highly mobile throughout the material in cooperation with the network rearrangement [10]. When the specimen is stretched, the transverse contraction forces reduction of intermolecular distance. Accordingly, quite a few transient crosslinks are easily established among neighbor macromolecules and iron ions. Because (i) formation of additional crosslinks is faster than relaxation movement of the molecular chains and (ii) the higher crosslinking density corresponds to higher strength of the material (Figure 5), the measured stress increases with time after the initial drop due to conformation change (Figure 3a). With respect to dry HBPU-DMPA-[Fe(DOPA)$_3$] and the control HBPU-DMPA-DOPA, no dynamic bonds are available so that their stress relaxation behaviors resemble those of irreversibly bonded polymers. The stress

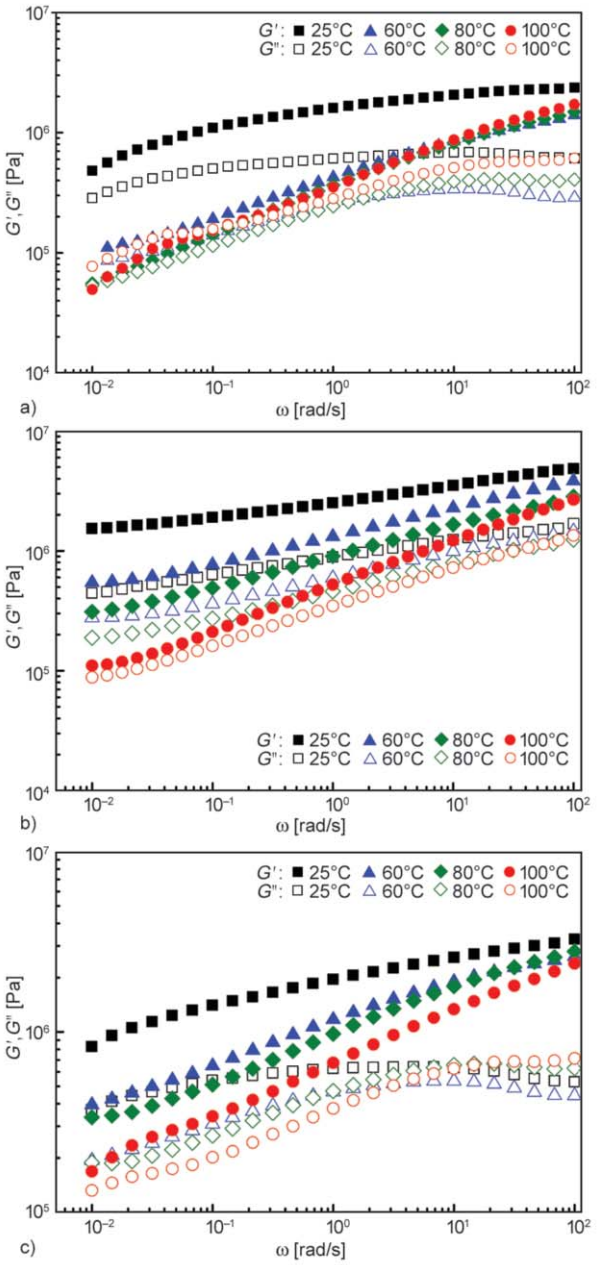

Figure 4. Storage shear modulus, G', and loss shear modulus, G'', as a functions of oscillatory frequency, ω, for (a) HBPU-DMPA-[Fe(DOPA)$_3$] saturated by water (pH = 9), (b) HBPU-DMPA-[Fe(DOPA)$_3$] that was firstly saturated by water (pH = 9) and then dried, and (c) HBPU-DMPA-DOPA saturated by water (pH = 9)

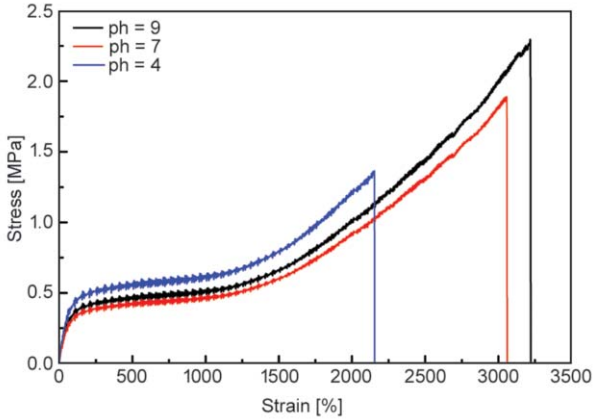

Figure 5. Tensile stress-strain curves of HBPU-DMPA-[Fe(DOPA)$_3$] measured in water at 25 °C

rapidly declines to a stable value and then no longer changes with time (Figures 3b and 3c).

To verify the analysis, a group of model experiments are designed as follows. Firstly, HBPU-DMPA-[Fe(DOPA)$_3$] was compressed in a mold to simulate the Poisson's contraction induced during tensile stress relaxation test (refer to the Experimental part for more details). Next, Raman spectra of the compressed specimen were collected as a function of compression time (equivalent to stress relaxation time to some degree). As the band at 500~650 cm^{-1} originates from chelation of Fe^{3+} with oxygen atoms of catechol [15], the peak area is correlated with coordination number of catechol-Fe^{3+} bonds. Although the compressed specimens had to be taken out of the mold for the spectroscopic measurement, the plastic deformation produced by compression cannot be fully recovered, so that the obtained structural information still roughly describes the characteristics of the crosslinkages as expected.

It is seen from Figure 6 that the area of the Raman peak at 500~650 cm^{-1} of water saturated HBPU-DMPA-[Fe(DOPA)$_3$] increases with a rise in compression time in the case of pH = 7 and 9. Moreover, the increment for pH = 9 is greater than that for pH = 7. Clearly, amount of the newly formed catechol-Fe^{3+} crosslinkage increases with time at a constant pH value of 7 or 9, and also increases with pH at a constant time. When pH = 4, the Raman peak area keeps unchanged within the time rage of interests, meaning the quantity of catechol-Fe^{3+} crosslinkage remains the same. The situation apparently coincides with the dry HBPU-DMPA-[Fe(DOPA)$_3$] (Figure 6).

By comparing Figure 3 with Figure 6, it is reasonable to conclude that the Poisson's contraction created in the course of tensile stress relaxation test promotes formation of catechol-Fe^{3+} crosslinkage in water saturated HBPU-DMPA-[Fe(DOPA)$_3$]. This is true especially for pH = 9. Considering the fact that the tris-coordinate catechol-Fe^{3+} crosslinks generate larger confinement than bis- and mono-catechol-Fe^{3+} coordination established at pH = 7 and 4, the polymer exhibits more obvious self-strengthening effect with a rise in time under the circumstances. ^{57}Fe Mössbauer measurements of model complex of Fe[DOPA]$_3$indicate that in the case of pH = 9, both tris- and bis-coordination bonds appear in anhydrous sample, while tris-coordination bonds predominate in water saturated version due to the dynamic coordination-dissociation of DOPA-iron interaction [10]. Compared to small molecular Fe[DOPA]$_3$, however, migration of iron ions in HBPU-DMPA-[Fe(DOPA)$_3$] has to be hindered by the surrounding macromolecules even when water is present. Consequently, some iron ions can only establish bis-coordination with catechol for pH = 9 due to the kinetic factor. The coexistence of tris- and bis-catechol-Fe^{3+} crosslinks [11, 16] makes it possible for the polymer HBPU-DMPA-[Fe(DOPA)$_3$] to increase its crosslinking density by converting bis-coordination into tris-coordination. So long as the intermolecular space is reduced, probability of collision of iron ions with catechol in the polymer is raised and more tris-coordination would be obtained (Figure 7).

For pH = 7, the crosslinks of HBPU-DMPA-[Fe(DOPA)$_3$] is dominated by bis-catechol-Fe^{3+} co-

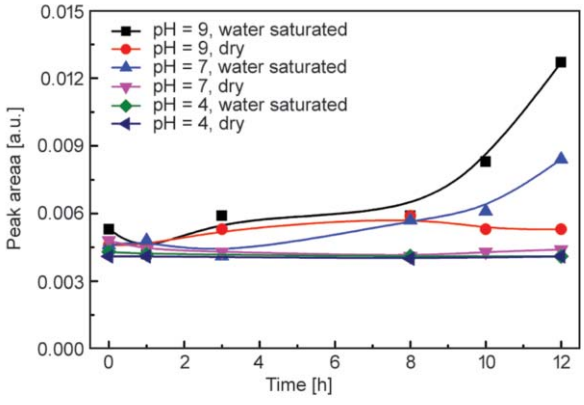

Figure 6. Area of the Raman peak at 500~650 cm^{-1} of HBPU-DMPA-[Fe(DOPA)$_3$] versus compression time

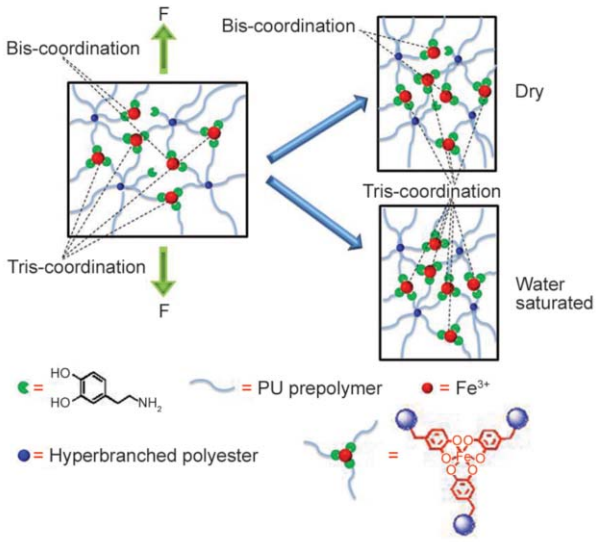

Figure 7. Change in coordination number of catechol-Fe^{3+} bonds of HBPU-DMPA-[$Fe(DOPA)_3$] in response to lateral contraction during tension (pH = 9)

ordination. Although amount of the crosslinks also increases, the improvement of material strength is less significant. Meantime, the compacted macromolecular chains do not contribute to formation of mono-catechol-Fe^{3+} coordination at pH = 4, as mono-coordination does not necessarily involve aggregated molecules. Therefore, there is no detectable change in the corresponding curve of Figure 6. Since the intermolecular interaction is not enhanced, the specimen of water saturated HBPU-DMPA-[$Fe(DOPA)_3$] (pH = 4) does not show stress intensification during stress relaxation test (Figure 3a).

On the other hand, Figure 6 demonstrates that the catechol-iron interaction nearly does not vary in the dry HBPU-DMPA-[$Fe(DOPA)_3$]. Because the dynamic bonds are immobilized in the material, coordination number of catechol-Fe^{3+} bonds has to be unchanged regardless of mobility of iron ions (Figure 7). It agrees with the results of stress relaxation that the specimens behave like conventional polymers (Figure 3b).

In fact, stress intensification is not limited to HBPU-DMPA-[$Fe(DOPA)_3$]. When the iron is replaced by boron, the water saturated HBPU-DMPA-[$B(DOPA)_2$] (pH = 9) also shows the same effect (Figure 8). There is no technique available for determining coordination status of boron in bulk material for the moment. Detailed investigation of the underlying mechanism has to be made in the future, but the result provides a useful reference for designing materials with similar property.

Nevertheless, it is worth noting that dynamically bonded polymers do not necessarily exhibit similar stress intensification manner. As mentioned in the Introduction, the stress applied to the polymers crosslinked by dynamic reversible bonds (like disulfide, C–ON and aromatic Schiff base bonds) used to relax to zero [3–9]. It might be attributed to the fact that these polymers lack the mechanism of increasing crosslinks during stress relaxation.

4. Conclusions

The stress intensification observed during tensile stress relaxation test of HBPU-DMPA-[$Fe(DOPA)_3$] proves to result from increase of catechol-iron crosslinkages. Formation of the additional crosslinkages is so fast that relaxation of the chain segments are not ready to proceed. High pH (e.g. pH = 9) of the water used for saturating the polymer favors creation of more tris-coordination and hence more obvious the self-strengthening effect. The habit might find application in offshore engineering.

In a broad sense, the stress intensification is useful for improving durability of polymeric products for long-term usage as they would no longer flow under a fixed load like conventional versions but become stronger. Further efforts are needed to know more about the working principle, to enhance the effect, and to reproduce the property across different materials.

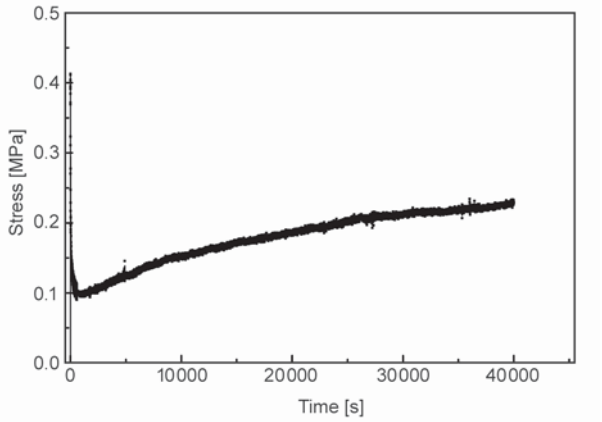

Figure 8. Tensile stress relaxation behavior of water saturated HBPU-DMPA-[$B(DOPA)_2$] (pH = 9). Temperature: 25 °C.

Acknowledgements

The authors thank the support of the Natural Science Foundation of China (Grants: 51273214 and 51333008), the Natural Science Foundation of Guangdong (Grant: S2013020013029), the Science and Technology Program of Guangzhou (Grant: 2014J4100121), and the Basic Scientific Research Foundation in Colleges and Universities of Ministry of Education of China (Grants: 15lgzs103 and 14lgqt01).

References

[1] Manson J. A., Sperling L. H.: Polymer blends and coposites. Springer, New York (1976).

[2] Sperling L. H.: Introduction to physical polymer science. Wiley, Hoboken (2006).

[3] Pepels M., Filot I., Klumperman B., Goossens H.: Self-healing systems based on disulfide–thiol exchange reactions. Polymer Chemistry, **4**, 4955–4965 (2013).
DOI: 10.1039/C3PY00087G

[4] Lei Z. Q., Xie P., Rong M. Z., Zhang M. Q.: Catalyst-free dynamic exchange of aromatic Schiff base bonds and its application to self-healing and remolding of crosslinked polymers. Journal of Materials Chemistry A, **3**, 19662–19668 (2015).
DOI: 10.1039/C5TA05788D

[5] Lei Z. Q., Xiang H. P., Yuan Y. J., Rong M. Z., Zhang M. Q.: Room-temperature self-healable and remoldable cross-linked polymer based on the dynamic exchange of disulfide bonds. Chemistry of Materials, **26**, 2038–2046 (2014).
DOI: 10.1021/cm4040616

[6] Xiang H. P., Qian H. J., Lu Z. Y., Rong M. Z., Zhang M. Q.: Crack healing and reclaiming of vulcanized rubber by triggering the rearrangement of inherent sulfur crosslinked networks. Green Chemistry, **17**, 4315–4325 (2015).
DOI: 10.1039/C5GC00754B

[7] Zhang Z. P., Rong M. Z., Zhang M. Q.: Room temperature self-healable epoxy elastomer with reversible alkoxyamines as crosslinkages. Polymer, **55**, 3936–3943 (2014).
DOI: 10.1016/j.polymer.2014.06.064

[8] Yuan C. E., Rong M. Z., Zhang M. Q.: Self-healing polyurethane elastomer with thermally reversible alkoxyamines as crosslinkages. Polymer, **55**, 1782–1791 (2014)
DOI: 10.1016/j.polymer.2014.02.033

[9] Zhang Z. P., Lu Y., Rong M. Z., Zhang M. Q.: A thermally remendable and reprocessable crosslinked methyl methacrylate polymer based on oxygen insensitive dynamic reversible C–ON bonds. RSC Advances, **6**, 6350–6357 (2016).
DOI: 10.1039/C5RA22275C

[10] Xia N. N., Xiong X. M., Wang J., Rong M. Z., Zhang M. Q.: A seawater triggered dynamic coordinate bond and its application for underwater self-healing and reclaiming of lipophilic polymer. Chemical Science, **7**, 2736–2742 (2016).
DOI: 10.1039/C5SC03483C

[11] Holten-Andersen N., Harrington M. J., Birkedal H., Lee B. P., Messersmith P. B., Lee K. Y. C., Waite J. H.: pH-induced metal-ligand cross-links inspired by mussel yield self-healing polymer networks with near-covalent elastic moduli. Proceedings of the National Academy of Sciences of the United States of America, **108**, 2651–2655 (2011).
DOI: 10.1073/pnas.1015862108

[12] Roberts M. C., Hanson M. C., Massey A. P., Karren E. A., Kiser P. F.: Dynamically restructuring hydrogel networks formed with reversible covalent crosslinks. Advanced Materials, **19**, 2503–2507 (2007).
DOI: 10.1002/adma.200602649

[13] Bose R. K., Hohlbein N., Garcia S. J., Schmidt A. M., van der Zwaag S.: Connecting supramolecular bond lifetime and network mobility for scratch healing in poly(butyl acrylate) ionomers containing sodium, zinc and cobalt. Physical Chemistry Chemical Physics, **17**, 1697–1704 (2015).
DOI: 10.1039/C4CP04015E

[14] Bode S., Enke M., Bose R. K., Schacher F. H., Garcia S. J., van der Zwaag S., Hager M. D., Schubert U. S.: Correlation between scratch healing and rheological behavior for terpyridine complex based metallopolymers. Journal of Materials Chemistry A, **3**, 22145–22153 (2015).
DOI: 10.1039/C5TA05545H

[15] Michaud-Soret I., Andersson K. K., Que Jr. L., Haavik J.: Resonance Raman studies of catecholate and phenolate complexes of recombinant human tyrosine hydroxylase. Biochemistry, **34**, 5504–5510 (1995).
DOI: 10.1021/bi00016a022

[16] Sever M. J., Wilker J. J.: Absorption spectroscopy and binding constants for first-row transition metal complexes of a DOPA-containing peptide. Dalton Transactions, **2006**, 813–822 (2006).
DOI: 10.1039/B509586G

eXPRESS Polymer Letters Vol.10, No.9 (2016) 750–761
Available online at www.expresspolymlett.com
DOI: 10.3144/expresspolymlett.2016.69

Evaluation of the release characteristics of covalently attached or electrostatically bound biocidal polymers utilizing SERS and UV-Vis absorption

G. N. Mathioudakis[1,2], A. Soto Beobide[1], N. D. Koromilas[2], J. K. Kallitsis[1,2], G. Bokias[1,2], G. A. Voyiatzis[1]*

[1]FORTH/ICE-HT, P.O. Box 1414, GR-265 04 Rio-Patras, Greece
[2]Department of Chemistry, University of Patras, GR-265 00 Rio-Patras, Greece

Received 18 January 2016; accepted in revised form 30 March 2016

Abstract. In this work, biocidal polymers with antimicrobial quaternized ammonium groups introduced in the polymer biocidal chains either through covalent attachment or electrostatic interaction have been separately incorporated in a poly (methyl methacrylate) polymer matrix. The objective of present study was to highlight the release characteristics of biocidal polymers, primarily in saline but also in water ethanol solutions, utilizing UV-Vis absorption and Surface Enhanced Raman Scattering (SERS). It is shown that through the combination of UV-Vis and SERS techniques, upon the release process, it is possible the discrimination of the polymeric backbone and the electrostatically bound biocidal species. Moreover, it is found that electrostatically bound and covalently attached biocidal species show different SERS patterns. The long term aim is the development of antimicrobial polymeric materials containing both ionically bound and covalently attached quaternary ammonium thus achieving a dual functionality in a single component polymeric design.

Keywords: *polymer composites, surface enhanced Raman spectroscopy (SERS), biocidal polymers, release, quaternary ammonium salts*

1. Introduction

The design of novel environmentally friendly/acceptable biocidal polymeric materials represents a very intensive basic research field, related with modern technological demands. For instance the development of 'clean' surfaces for sensitive sanitary applications or/and alternative antifouling paints to address crucial ecological and environmental problems in marine applications are some of the current challenges we face. The term biocide refers to a substance that mainly acts by inhibiting the growth of microorganisms with harmful consequences not only to human health but also to the quality of several products. The incorporation of antimicrobial substances into polymer matrices gains more and more field in technical hygiene processes as the need for secure 'clean' surfaces for sensitive sanitary applications increases [1, 2]. Moreover, the development of antifouling paints to confront crucial ecological and environmental problems in marine applications is some of the current challenges. An application field of these materials is in the aquaculture sector as well as in marine technology and navigation. In the latter, it is expressed by the marine biofouling, namely the accumulation and the adhesion of organisms, such as barnacle, tube worms and algae, to a surface in contact with water for a long time. Thus, extensive research is conducted in this wide field, concerning between others nets with biocidal properties especially in the aquaculture or/and antifouling paints for sub-

*Corresponding author, e-mail: asoto@iceht.forth.gr

merged surfaces of the vessels. Polymers with quaternary ammonium or phosphonium salts are widely explored materials with potent antimicrobial activity [3–5]; these cationic biocides target the bacterial membranes. Their antimicrobial activity is based on their ability to disrupt and disintegrate the negatively charged cell membranes. In some cases [6], phosphonium salts show higher activity [7] and higher thermal stability [8, 9] however, usually with more demanding chemistry than the quaternary ammonium analogues.

In this specific case, antimicrobial polymeric materials containing quaternary ammonium were developed. They can be classified in two categories depending on the incorporation of the quaternary ammonium salts onto polymers, namely the ionically bound or the covalently attached [10–12]. The polymeric materials of the first category habitually exhibit strong biocidal action based on the release of the active quaternary cation in the vicinity of the aqueous environment through ion exchange mechanism; that allows the dissolution of the polymeric phase and the exploit of the whole biocidal material. However, the biocidal action of the second category is based on the contact of the antimicrobial polymer with the microorganisms, preventing any biocidal release that would burden the marine environment. A note is made of the fact that each category has inherent advantages and disadvantages. Biocidal surfaces bearing immobilized active groups may prevent the formation of viable biofilms; however, they could still be contaminated by remaining dead bacteria that may initiate immune responses and inflammation [13]. From the other side, biocidal surfaces, carrying active agents that could be released, may prevent or reduce the initial attachment of bacteria. Therefore, the combination of both strategies is anticipated to reveal an ideal antibacterial polymeric material; however, till now, few works exhibiting relevant dual antibacterial function have been reviewed [14, 15]. This study constitutes the preliminary effort to reveal the release characteristics, if any, of polymeric quaternary ammonium biocides of both types in simulated seawater and hopefully highlight the importance of the development of their combination in one antimicrobial polymeric material containing together ionically bound and covalently attached quaternary ammonium groups.

Raman spectroscopy is a widely used non-invasive technique that provides detailed molecular information. Surface Enhanced Raman spectroscopy (SERS) might be proved a superior detection method because it is a very sensitive technique manifested as an enhancement by many orders of magnitude of the intensity of Raman radiation by molecules in the immediate vicinity to nano-rough metal surfaces or nano-structured colloidal clusters of noble metals, such as Ag and Au. SERS constitutes a challenge of applying it to extremely low concentration level analysis. Applying a surface enhanced Raman scattering excitation/collection configuration bearing an oscillating cell and combined with right angle scattering collection geometry we have quite recently introduced a new method to quantitatively monitor the level of active agents at very low concentration range [16, 17].

The present work is mainly an attempt to monitor by SERS the release of biocide polymers from polymeric films and compare the release rate obtained with a traditional and consequently most commonly used technique in quantitative analysis of controlled release, such as UV-Vis absorption. In this context, polymeric matrices with the ability of controlled release have been developed; two different biocide polymers (PSSAmC16 and PVBCHAM, see Figure 1) have been incorporated into poly(methyl methacrylate) (PMMA) specimens. These films are new polymeric materials with enhanced (and controlled) antifouling properties, which hold great promise for potential applications in the field of 'clean' surfaces, either for health reasons or as antifouling. The monitoring of the release characteristics of these biocide polymers from the polymeric matrix mainly in saline but also in 95% ethanol solution has been carried out and compared utilizing both UV-Vis absorption and SERS.

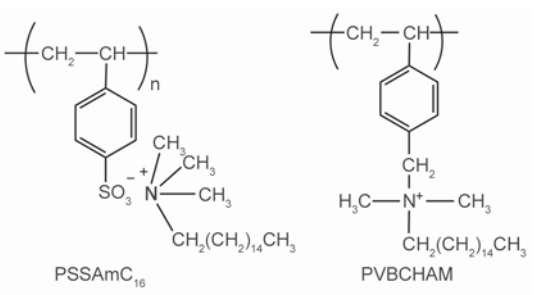

Figure 1. Chemical structures of the polymeric biocides PSSAmC16 (left) and PVBCHAM (right)

2. Experimental

2.1. Materials

Poly(methyl methacrylate) (PMMA, 29773) was a product of BDH Chemicals Ltd, Poole England. Hexadecyl trimethyl ammonium bromide (CTAB, H5882) was supplied from Sigma-Aldrich Germany and dimethylacetamide (DMA, O24344) was purchased from Fisher Scientific Europe. The synthesis of poly(styrene hexadecyl trimethyl ammonium sulfonate) (PSSAmC16) and poly(vinyl benzyl dimethyl hexadecyl ammonium chloride) (PVBCHAM) has been described in details elsewhere [5, 10, 18, 19] and their chemical structures are shown in Figure 1. Analytical grade silver nitrate (>99.99%, 209139) and sodium citrate tribasic dehydrate (99.0%, S4641) for colloid preparation were purchased from Sigma-Aldrich Germany, too.

2.2. Preparation of polymer films

PMMA membranes containing polymeric biocides in a composition 90/10 per weight were prepared by the solution casting technique. The specific biocidal polymer (0.03 g) and the polymer matrix PMMA (0.27 g) were dissolved in 5 mL DMA and heated on a hot plate at 80 °C under stirring to reach complete dissolution. The polymer mixture solutions were cast on a Pyrex petri plate (diameter 5 cm) at 80 °C for 24 hours, the obtained film was dried in a vacuum oven at 80 °C for complete solvent removal. The films had a thickness of 100–120 μm.

2.3. Release studies

For release studies, a piece of film (~40 mg, with dimensions 1.5 cm×1.5 cm×0.1 mm) was cut and placed in vials filled with 8 mL of either ethanol 95% or NaCl 0.5 M (seawater simulation) on a Wisd shaking incubator at 50 rpm and 17 °C. The weighted amounts of the specimens were precisely selected so as in the case of total release of biocide agent its concentration into the different solutions to be 0.5 mg/mL (see UV-Vis absorption calibration curve Figure 2). At several time intervals 2 mL aliquots were withdrawn and UV-Vis absorption spectra were measured using a double beam Lambda UV/Vis/NIR Spectrometer of Hitachi (U-3000). After the UV-Vis absorption measurement the aliquot was decanted back to the vials.

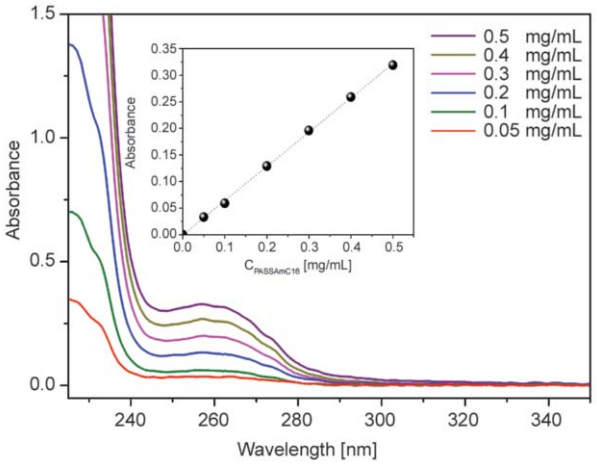

Figure 2. UV–Vis absorption spectra of PSSAmC16/0.5 M NaCl solutions at various concentrations. Inset: The calibration curve plot absorbance versus concentration extracted from the spectra

The release of biocide polymers from the polymeric matrix was also monitored by Surface Enhanced Raman Scattering (SERS). The colloids used to collect the SERS spectra were prepared according to a modified Lee and Meisel procedure [16, 20]. For these measurements, 100 μL aliquots were removed from the vials containing the piece of film immersed in ethanol or NaCl solution, but this aliquot volume was not returned or replaced. The addition of extra 100 μL of the aggregating agent NaCl (1 M) into 1 mL of Ag silver colloid gave rise to the more pronounced enhancement. The Raman/SERS spectra were excited with a water-cooled Ar^+ laser (Spectra physics model 2017, 5 W all lines) operating at 514.5 nm. An achromatic doublet (f: 145 mm; j: 35 mm) was utilized to focus the laser beam into a Pyrex test tube filled with nanocolloidal silver suspensions; the power of the laser beam measured in front of the sample was 40 mW. Raman spectra were collected using the T-64000 spectrometer of Jobin Yvon (ISA-Horiba group). The Raman system was used in the single spectrograph configuration for the collection, analysis and detection of the scattered light. This spectrograph bears a rectangular entrance slit long (and horizontal) in the direction perpendicular to the lateral direction of the separation of light. Therefore, it allows the optimum right angle collection of the collateral scattering volume of a linear-like focusing field of the excitation laser line. For the elastic Rayleigh scattering rejection, an edge filter (LP02-514RU-25,

Laser 2000 (UK) Ltd.) was used. The Raman photons were dispersed by a 600-grooves/mm blazed holographic diffraction grating and detected by a standard LN2 cooled front illuminated CCD detector. The spectrometer was wavenumber calibrated using the standard Raman band positions of cyclohexane. Reproducible and improved Raman scattering collection measurements were allowed by the use of an 'oscillating cell' in combination with the advantage of utilizing the right angle light scattering collection geometry. A detailed description of this configuration has been reported before [16]. Reference FT-Raman spectra were also obtained with NIR excitation at 1064 nm (via an R510 diode pumped Nd:YAG laser) utilizing a Raman component (FRA-106/S) attached to an Equinox 55 Bruker spectrometer.

3. Results and discussion

3.1. Description of polymeric biocides

Quaternary ammonium salts are important biocides known to be effective against a broad spectrum of micro-organisms. The antimicrobial efficacy of hexadecyl trimethyl ammonium bromide, CTAB, depends to a great extent on the length of the alkyl chain (hexadecyl chain) [21]. The chemical structures of the biocidal polymers studied here are shown in Figure 1. Hexadecyl trimethyl ammonium cation (AmC16) was incorporated through ion interactions in PSSNa to give as product the homopolymer poly(sodium styrene hexadecyl trimethyl ammonium sulfonate) (PSSAmC16). On the other hand, the quaternized poly(vinyl benzyl dimethyl hexadecylammonium chloride) (PVBCHAM) bears the ammonium group attached covalently on the polymeric chain [10]. The biocidal activity against a broad range of bacteria of the copolymers bearing quaternary ammonium units with potential antibacterial functionalities bound covalently or electrostatically onto the polymeric chain has been studied in parallel [22].

In this work, the ion exchangeable or polymer bound quaternary ammonium groups of PSSAmC16 and PVBCHAM, respectively, are considered, in terms of release ability from the PMMA matrix. Thus, a seawater simulant (aqueous 0.5 M NaCl solution) or a polar solvent (EtOH 95%) were used to conduct the study. It should be mentioned that, in the case of PSSAmC16 release in aqueous 0.5 M NaCl solution, it is unclear whether the AmC16 groups are just exchanged or the whole PSSAmC16 chain is dissolved. As it will be shown, the combination of SERS and UV-Vis spectroscopy have been proved crucial in this case to discriminate between the AmC16 cations and the poly(styrene sulfonate), PSS, backbone.

3.2. Calibration curves

While the solubility of PSSAmC16 in pure water is limited, the polymer is soluble in aqueous 0.5 M NaCl solution [18]. So, the UV-Vis spectra of PSSAmC16 and CTAB in this seawater simulant were evaluated (Figure 3). The main broad absorption zone of PSSAmC16, bearing bands tentatively located at 256 and 262 nm, is attributed to the benzene ring. On the other hand, the amine based cationic quaternary group in the PSSAmC16, that is CTAB, does not exhibit any significant absorption in the wavelength range under study. Thus, UV-Vis spectroscopy can be used in order to detect the release of PSS backbone of the biocidal polymer in the solution.

Figure 2 depicts the UV-Vis absorption spectra of PSSAmC16 in 0.5 M NaCl solutions at a concentration range from 0.05 to 0.5 mg/mL at 0.1 mg/mL step range. In the inset of Figure 2, the absorbance of the PSSAmC16/NaCl solution at 262 nm is plotted versus concentration, constituting the UV-Vis absorption calibration curve (R^2 = 99.74%) that obeys a linear Beer's law behavior, with a limit of detection LOD = 28 μg/mL and a limit of quantification, LOQ = 95 μg/mL. Similarly, calibration UV-Vis absorption curves have been performed also for PSSAmC16 and PVBCHAM in 95% ethanol solution (Figure 4). Figure 4 depicts the UV-vis absorption spectra of 95%

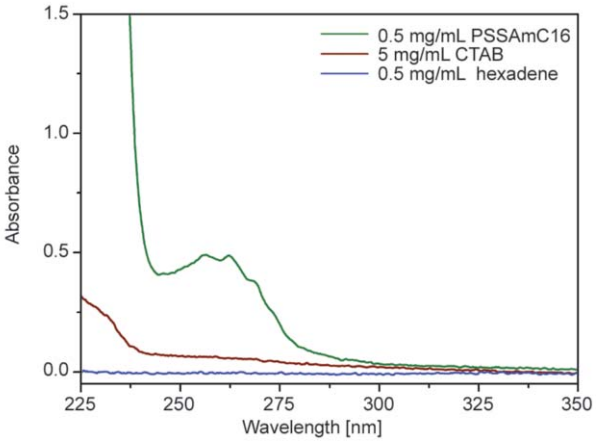

Figure 3. UV–Vis absorption spectra of polymeric biocide PSSAmC16, the quaternary biocide group CTA^+ in 0.5 M NaCl solutions and the aliphatic group Hexadecane in ethanol

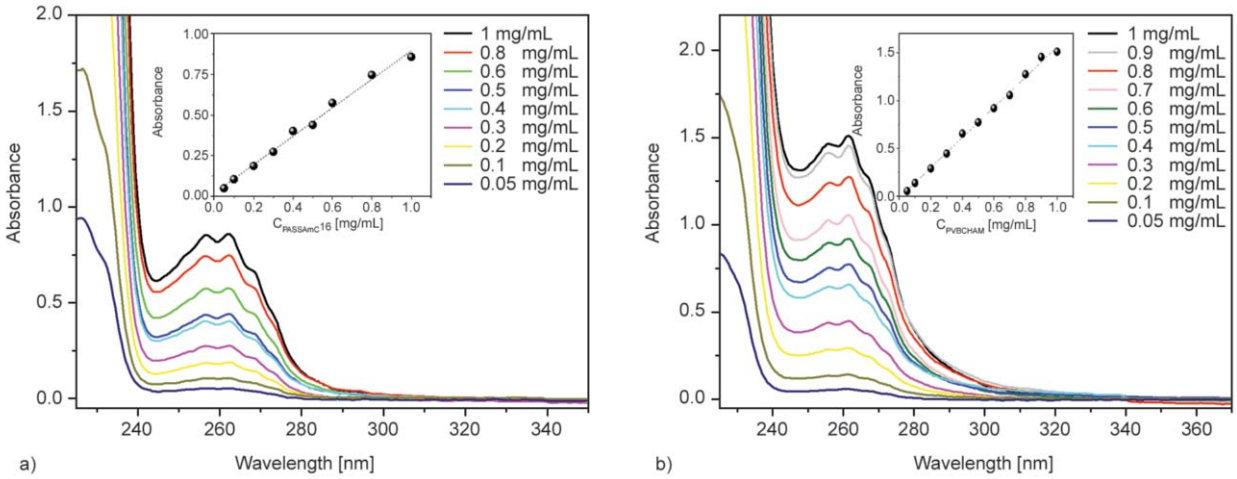

Figure 4. UV–vis absorption spectra of 95% ethanol solutions of: PSSAmC16 (a) and PVBCHAM (b) at various concentrations. Inset: The calibration curve plots absorbance versus concentration extracted from the spectra

ethanol solutions of PSSAmC16 and PVBCHAM at a concentration range from 0.05 to 1 mg/mL at 0.1 mg/mL step range. The main absorption bands (λ_{max}) of both are located at 256 and 262 nm. In the inset of figures, the absorbance of the polymeric biocides in ethanol solution at 262 nm is plotted versus concentration constituting the UV-Vis absorption calibration curve that obeys a linear Beer's law behavior. However, since PVBCHAM is not soluble in NaCl, relevant calibration curve could not be obtained.

In Figure 5, the SERS calibration curve of PSSAmC16 in 0.5 M NaCl solutions is depicted at a concentration range from 10 to 500 μg/mL in the spectral window 1500 to 3200 cm^{-1}. SERS spectra were obtained with a laser power of 40 mW on sample and a spectral slit width (SSW) of ~6 cm^{-1}. The main spectral features observed when increasing PSSAmC16 concentration are the peak at ~1460 cm^{-1} attributed to the CH_2 and CH_3 bending and the peak at 2848 cm^{-1} due to CH stretching in the long methylene chain. For assessment purposes, surface enhanced Raman spectrum of CTAB solution was also obtained. Figure 6 curve c shows the SERS spectrum of a 500 μg/mL CTAB in 0.5 M NaCl solution. For comparison, the conventional Raman spectra of the respective solution and of pure solid CTAB are depicted as Figure 6 curve b and curve a, correspondingly. On the one side, no scattering spectral features were collected from the particular CTAB solution in the conventional Raman spectrum (Figure 6 curve b). On the other side, comparing the SERS spectrum of CTAB (Figure 6 curve c) and the corresponding FT-Raman spectrum

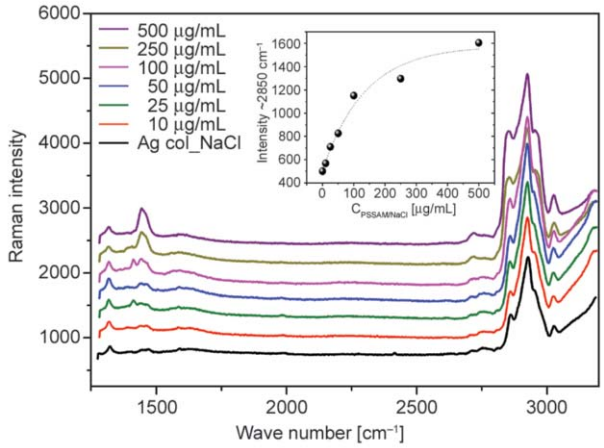

Figure 5. Representative SERS spectra from 100 μL of PSSAmC16/0.5 NaCl solutions placed in 1 mLof Ag nano-colloid suspensions activated with 100 μL NaCl 1 M. Inset: calibration curve plot obtained from the intensity values of the peak at ~2850 cm^{-1} versus concentration

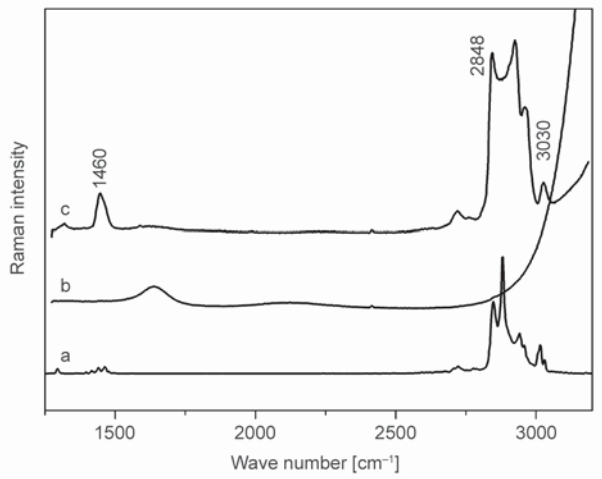

Figure 6. Raman spectra of CTAB: (a) FT-Raman spectrum of pure solid, (b) 0.5 mg/ml CTAB solution in NaCl 0.5 M, and (c) SERS spectrum of a 0.5 mg/mL solution CTAB in NaCl

obtained from the solid (Figure 6 curve a), similarities are found. However, there is an unusually large intensity enhancement of the band at ~1460 cm^{-1} (CH_2 and CH_3 bending) and the predominance of the band at 2848 cm^{-1} (CH– stretching region). The band at 3030 cm^{-1} is due to the head group $(CH_3)_3N^+$ stretch deformations. Dendramis *et al*. [23] have performed a detailed SERS study of CTAB and they concluded that it is not unreasonable to assign the ~1460 cm^{-1} band primarily to deformation of methyl groups attached to the quaternary nitrogen and suggested that the CTAB chain has most C–C bonds nearly parallel to the surface enhancing the Raman signal, while the head group is in close proximity to the surface with the three methyl groups positioned symmetrically over it. We would like to point out that we also attempted to obtain SERS spectrum of hexadecane (long chain methylene in CTAB, $CH_3(CH_2)_{14}CH_3$) dissolved in ethanol, since it is practically insoluble in water, but no vibrational spectrum was collected. Anyway, this certainly suggests that positively charged analyte, in the case of CTAB the head group $(CH_3)_3N^+$, is required for SERS when using citrate-reduced silver nanoparticles colloid (negative surface charge).

Comparing the SERS spectra in Figure 5 with the one in Figure 6 curve c, it is evident that the surface enhanced spectrum of PSSAmC16 coincides with the spectrum of CTAB; no additional peaks due to the poly(styrene sulfonate) are observable, and this is corroborated by the absence of spectral features due to the ring in the SERS spectra of PSSNa, which is similar to that of the silver colloid activated with 100 μL NaCl (Figure 7).

The usefulness of SERS as an accurate mean of determining the release of quaternary biocide group (AmC16) from the polymer PSSAmC16 can be use in parallel with the ability of UV-Vis absorption technique that allows the characterization of the poly (styrene sulfonate) group (PSS). As we have already established (Figure 3), the quaternary AmC16 group of PSSAmC16 does not exhibit any significant absorption band in the UV-Vis wavelength under study. This confirms that the absorption band obtained when measuring the UV-Vis spectra of PSSAmC16 solutions are due to the styrene sulfonate groups of the PSS chain. At the same time, the PSS chain does not present any spectral feature when trying to obtain

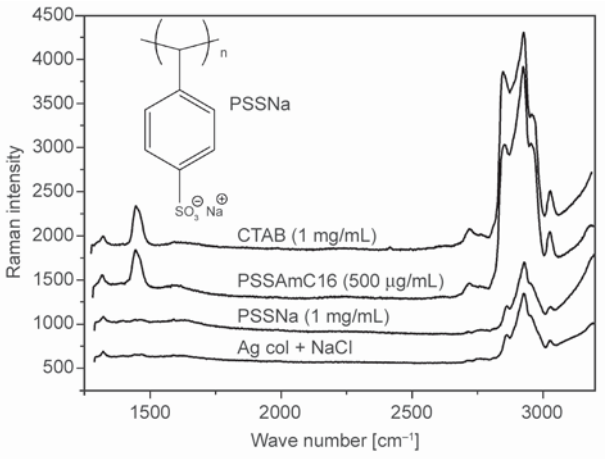

Figure 7. SERS spectra of CTAB, PSSAmC16 and PSSNa in NaCl solutions. Ag colloid is given for reference.

the SERS spectrum of a PSSNa solution (Figure 7), as verified by the complete absence of Raman signal from a 1 mg/mL PSSNa/NaCl solution when added to Ag colloid. The spectral features in the SERS spectra of PSSAmC16 are due to the CTAB group, since the SERS spectra of PSSNa is similar to that of the silver colloid activated with 100 μL NaCl. Namely, the strong similarity of the surface enhanced spectrum of the PSSAmC16/NaCl solution with the CTAB/NaCl solution confirms that the spectral features are due to the cationic quaternary biocide group (AmC16).

The second biocidal polymer under study is the quaternized poly (vinyl benzyl dimethyl hexadecylammonium chloride) (PVBCHAM) that bears the quaternary nitrogen attached covalently on the polymeric chain. This polymer is not soluble in NaCl as there is no possibility of ion exchange since the biocidal group is covalently attached to the chain. That is, the release studies of PVBCHAM from the PMMA polymeric matrix were performed in 95% ethanol solutions. Therefore, calibration curves of PVBCHAM in 95% ethanol solutions were elaborated using UV-Vis (Figure 4b) and SERS (Figure 8) measurements. Absorption spectra present the characteristic bands of the aromatic ring at 256 and 262 nm as in the case of PSSAmC16. The corresponding SERS spectral features of PVBCHAM (Figure 8) are not identical to those of AmC16. The 2848 cm^{-1} Raman peak attributed to CH– stretching and the Raman peak at 3030 cm^{-1} due to the head group $(CH_3)_3N^+$ stretch deformations in AmC16 are not the predominant ones

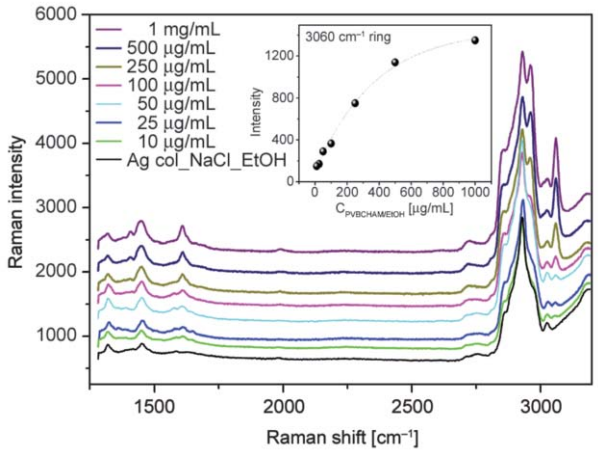

Figure 8. Representative SERS spectra from 100 µL of PVBCHAM/95%ethanol solutions placed in 1 mL of Ag nano-colloid suspensions activated with 100 µL NaCl 1 M. Inset: calibration curve plot obtained from the intensity values of the peak at ~3060 cm^{-1} versus concentration

as in the case of PSSAmC16, but in the case of PVBCHAM new additional SERS features are generated at ~1613 and 3060 cm^{-1}. These new SERS peaks can be respectively assigned to the 1–4 disubstituted benzene ring (peak at ~1613 cm^{-1}) and the aromatic CH stretching mode (peak at 3060 cm^{-1}). On the other hand, we already know that in the case of PVBCHAM the biocide is covalently attached so there is not free quaternary species in the solution. As a consequence of electrostatic interactions, the polycation PVBCHAM most probably approaches close or even is attached to the negatively surface charged citrate-reduced silver nanoparticles and enhancement of the Raman peaks assigned to the aromatic ring occurs. This is an important issue, revealing the CTAB type of moieties as potential carriers stimulating SERS activity to attached presumably SERS inactive functional groups.

The corresponding SERS spectra of the biocidal polymers, PSSAmC16 and PVBCHAM, despite their similar structure, display some different spectral features, due to their own way of 'adsorption – interaction' at the colloid surface revealing distinct SERS features that enable discrimination between them. Based on these considerations/facts, it is then reasonable to assume the possibility of carrying out the main objective of present work highlighting the release characteristics of quaternary ammonium-based biocidal polymers, mainly in saline, but also in water ethanol solutions, utilizing UV-Vis absorption and SERS.

3.3. Release measurements

The release characteristics of the quaternary ammonium biocide group, either ionically attached or covalently bound, have been explored by a systematic study, via both UV-Vis absorption and SERS, performed for PMMA films containing PSSAmC16 or PVBCHAM and immersed into either 0.5 M NaCl (seawater simulate) or 95% ethanol solutions (accelerated release study) for a period of time extended up to a few weeks.

3.3.1. Immersion of ~40 mg of PMMA films doped with biocide polymer into 8 mL of 0.5 M NaCl solution

In Figure 9, we monitor both by UV-Vis (Figure 9a) and SERS (Figure 9b) any eventual release after the immersion of a PMMA/PSSAmC16 (90/10) film in 0.5 M NaCl solution for a period of time from a few hours up to 15 days. In the UV-Vis spectra, the absorption values are essentially close to the baseline with the maximum value at 0.10 after 15 days of immersion. According to the calibration curve of Figure 2, this could correspond to a concentration of

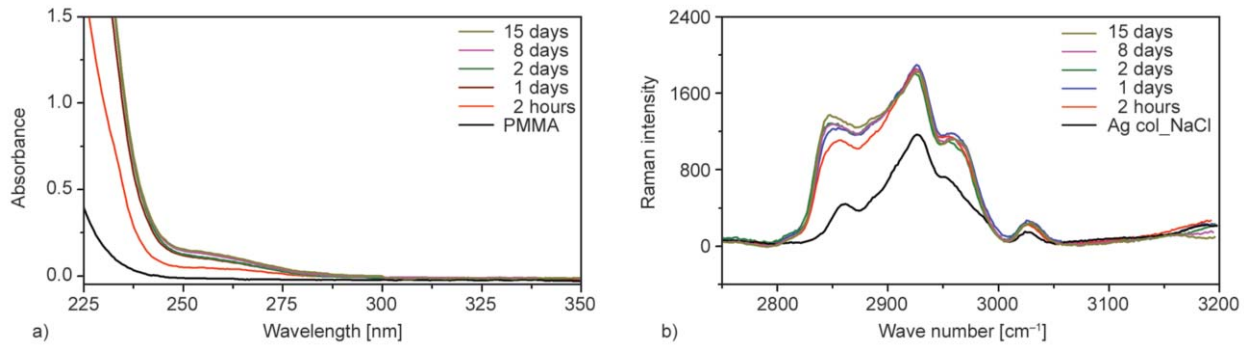

Figure 9. (a) UV-Vis absorbance spectra of the 0.5 M NaCl solution after the immersion of PMMA/PSSAmC16 (90/10) film for a period of time up to 15 days. (b) SERS spectra

PSS of ~150 μg/mL. The absorption spectrum of a 0.5 M NaCl solution where a pure PMMA film (without loaded biocide polymer) was immersed is also shown for comparison; it does not exhibit any absorption at ~262 nm regardless of the time of immersion. In the SERS spectra depicted on the Figure 9b, we can observe the corresponding vibrational spectroscopic features of PSSAmC16, in this case via the CTAB molecular fingerprint. There is an early release of AmC16 from the biocide doped PMMA film in the saline solution in the 2 first hours of immersion. Afterwards, during the next couple of weeks, it converges towards a plateau that corresponds to a concentration of AmC16 of ~200 μg/mL, according to the calibration curve in Figure 5. Therefore, the concentration of both ionic components of PSSAmC16 released, PSS and AmC16, in 8 mL of a 0.5 M NaCl solution after the immersion for 15 days of a ~40 mg PMMA/PSSAmC16 (90/10) film was effectively determined by the combination of UV-Vis and SERS. From these results, the overall quantity of the released material, namely the sum of the masses of its components found in solution, is determined at 2.8 mg. This quantity is ~70% of the PSSAmC16 content (4 mg) of the PMMA film, in a very good agreement with the results found through Total Organic Carbon and Total Nitrogen determination for the release of PSSAmC16 for similar release studies [18]. The projection of the concentration to the moles of PSSAmC16 released after a few weeks of immersion reveals a number of $0.80 \cdot 10^{-6}$ moles of styrene sulfonate units of PSS detected by the UV-Vis measurements vis-à-vis to the number of $0.70 \cdot 10^{-6}$ moles of AmC16 cations probed by SERS measurements.

Other PMMA film loaded with the covalently attached quaternary ammonium group, PVBCHAM, was also subjected to the same release conditions in 0.5 M NaCl solution. The UV-Vis measurements of aliquots measured at similar time intervals gave rise to very low absorption values even after the long period of time (15 days), coinciding with the absorption profile of the reference PMMA sample. The same applies for the corresponding SERS measurements; no vibrational spectral features were observed. That is, there is no release of PVBCHAM from the 10 wt% PVBCHAM incorporated PMMA film when immersed in NaCl 0.5 M.

3.3.2. Immersion of ~40 mg of PMMA films doped with biocide polymers into 8 mL of 95% ethanol solution

This time, PMMA/biocide samples were immersed in 95% ethanol solutions and the release of the biocide group was again studied by both UV-Vis and SERS. Figures 10 and 11 show the results for samples PMMA/PSSAmC16 (90/10) and PMMA/PVBCHAM (90/10), respectively, probed by both techniques. In the UV-Vis measurements shown as Figures 10a and 11a, the absorption spectrum of a 95% ethanol solution where a pure PMMA film (without loaded biocide polymer) was immersed is also shown as control in the two extreme time intervals of the release process adopted. There is certain absorption indicating that an amount of the polymer is present in the ethanol solution and increases with time due to the partial solubility of PMMA in 95% ethanol. The absorption is due to the carbonyl chromophore (C=O) of PMMA ($n \rightarrow \pi^*$ 270 nm, and $\pi \rightarrow \pi^*$ 170–200 nm). Therefore, in the biocide doped PMMA films immersed in ethanol solutions, there is an increasing contribution of the ~262–270 nm absorption zone due to the partial dissolution of the poly-

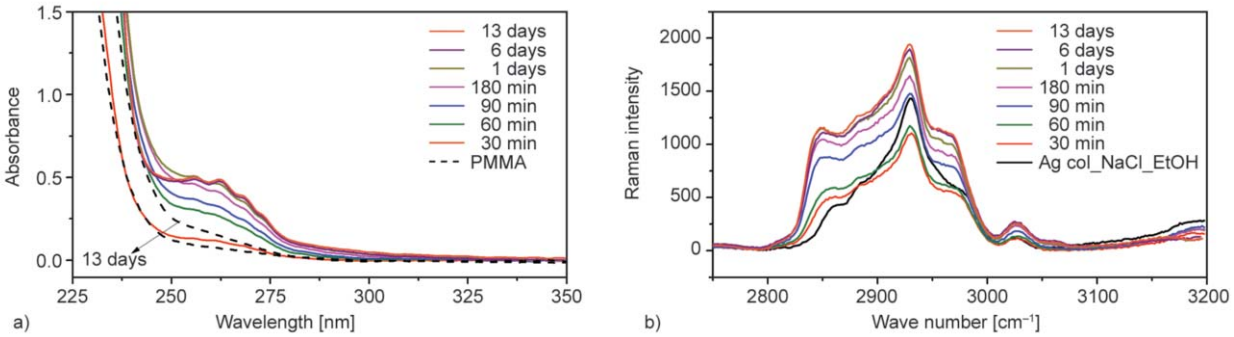

Figure 10. (a) UV-Vis absorbance spectra of the 95% ethanol solution after the immersion of PMMA/PSSAMC16 (90/10) film for a period of time up to 13 days. The UV-Vis spectra of an ethanol solution where a PMMA film was immersed (as blank) for a few minutes and for a period of 13 days are depicted with dash line. (b) SERS spectra

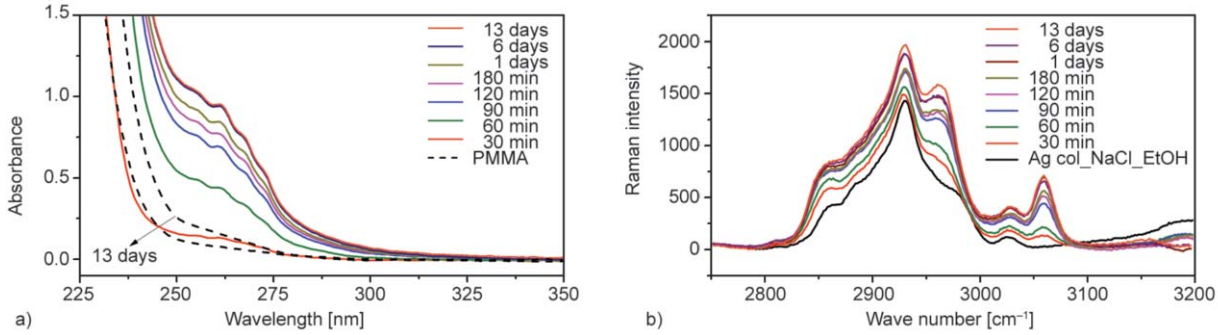

Figure 11. (a) UV-Vis absorbance spectra of the 95% ethanol solution after the immersion of PMMA/PVBCHAM (90/10) film for a period of time up to 13 days. The UV-Vis spectra of an ethanol solution where a PMMA film was immersed (as blank) for a few minutes and for a period of 13 days are depicted with dash line. (b) SERS spectra

mer matrix, as well. Taking into account the above, we may have a look at the release of either PSSAmC16 (Figure 10) or PVBCHAM (Figure 11) in 95% ethanol solution. It is clearly seen that at the beginning of the release process, in the first 2–3 hours, there is a 'burst' effect with elevated absorption values at ~262 nm. The absorption values in the case of PVBCHAM biocide polymer encapsulated in PMMA polymer matrix are higher than the corresponding bearing the PSSAmC16 one. This is in agreement with the higher absorption values of PVBCHAM with respect to PSSAmC16 in 95% ethanol calibration curves given in Figure 4. This burst effect can be explained by the swelling of PMMA polymer matrix in ethanol solutions [24], allowing the biocide polymer to be leached out of the polymer matrix. In the corresponding SERS experiments, shown in Figures 10b and 11b, a similar early release is observed for both PSSAmC16 and PVBCHAM biocide doped PMMA films immersed in 95% ethanol solutions.

In order to investigate the morphology and quality of mixing between the biostatic polymer and the polymeric matrix, cross section SEM images of biocide-free PMMA polymer films as well as after PSSAmC16 or PVBCHAM biocides incorporation before and after the immersion in NaCl 0.5 M and ethanol 95% aqueous solutions are shown in Figure 12. The fractured specimens were examined utilizing a SUPRA 35VP Zeiss scanning electron microscope. In Figures 12b and 12c, the biocides are shown to be dispersed in the PMMA matrix bearing micro droplet morphology, as compared to Figure 12a. After the immersion of the PMMA/biocide films in NaCl 0.5 M solution only the electrostatically bound PSSAmC16 has been released; as a consequence, craters were observed on the PMMA/PSSAmC16 films (Figure 12e) to the locations occupied by the biocide before. Conversely, in Figure 12f the SEM picture presents similar morphology to the corresponding of the control film (Figure 12c) since the covalently attached PCVBHAM is not released from the polymer matrix after the immersion in NaCl. Finally, when PMMA/biocide polymer films were immersed in ethanol solutions the release/dissolution of both biocides, PSSAmC16 and PVBCHAM, generates hollows in the polymeric matrix indicating a burst type release aided by the swelling or/and even the partial dissolution of the PMMA matrix (Figures 12g, h and i).

4. Conclusions

Surface enhanced Raman scattering allows the detection and more over the discrimination between similar biocide polymers bearing a quaternary ammonium group (hexadecyl trimethyl ammonium unit) introduced in the polymer chain through electrostatic or covalent interaction. In the case of electrostatic interaction (PSSAmC16), the bands corresponding to the head group vibration, $(CH_3)_3N^+$, appear to be preferentially enhanced, while in the case of covalent interaction (PVBCHAM), the bands enhanced are the ones belonging to the aromatic ring. This can be explained by the way the biocide polymers approximate the negatively charge citrate reduced silver colloid used for the SERS measurements. For PSSAmC16, there is ion exchange in NaCl solutions and it is the AmC16 group the one that interacts with the colloid. On the other hand, the polycation PVBCHAM interacts electrostatically with the citrate reduced silver colloid, resulting in the close proximity of the aromatic ring to the silver colloid and enhancing thus the Raman bands corresponding to the ring.

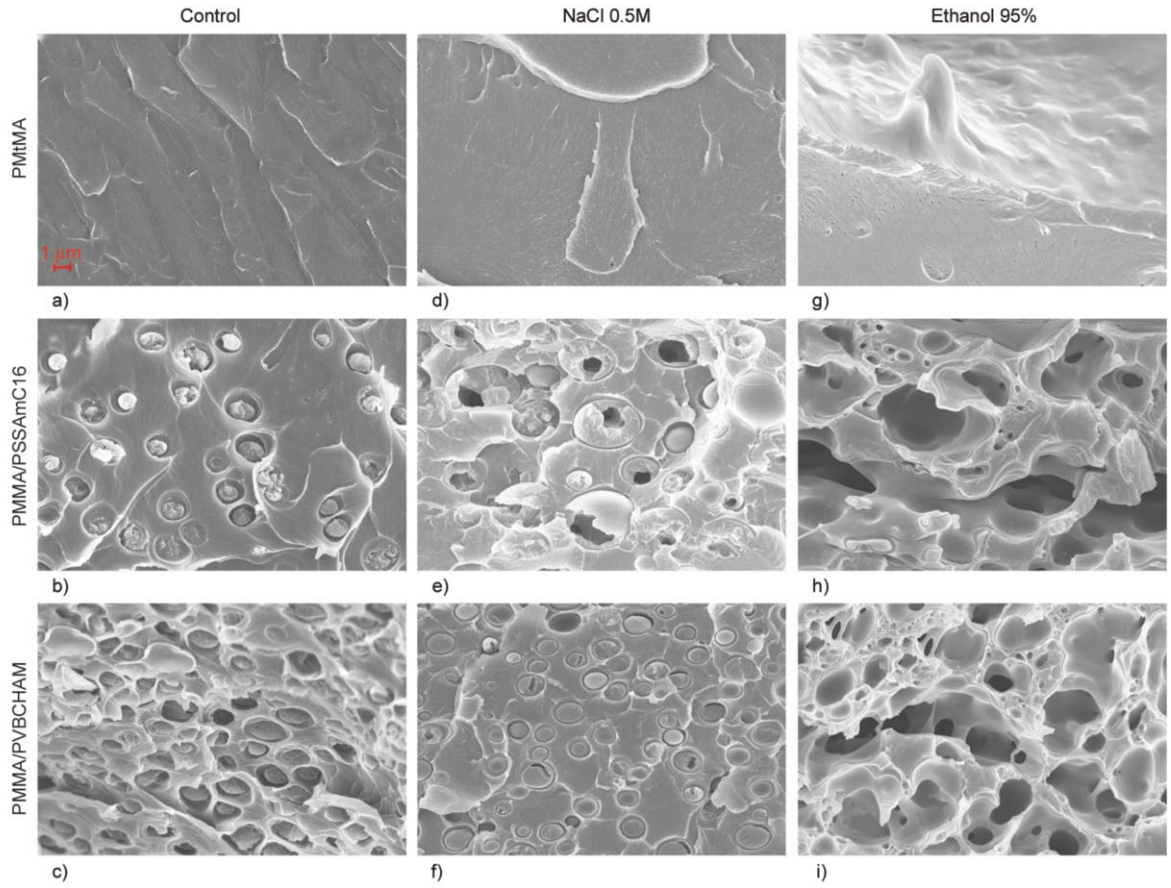

Figure 12. Film morphologies by SEM. Control films: PMMA (a), PMMA/PSSAmC16 90/10 (b) and PMMA/PVBCHAM 90/10 (c). Films immersed in 0.5 M NaCL: PMMA (d), PMMA/PSSAmC16 90/10 (e) and PMMA/PVBCHAM 90/10 (f). Films immersed in 95% ethanol: PMMA (g), PMMA/PSSAmC16 90/10 (h) and PMMA/PVBCHAM 90/10 (i).

From a practical point of view, in this work SERS and UV-Vis measurements were applied to study the release of biocidal polymers from a polymer matrix. When the polymer matrix bearing the biocide polymer is immersed in seawater simulation solution, the release of PSSAmC16 (the biocidal quaternized ammonium group is ionically attached to the polymer chain) can be detected by both methods; UV-Vis absorption is able to detect the polymer chain PSS and SERS measurements can identify the AmC16 group. This is due to dissociation of the PSSAmC16 in the NaCl solution through ion exchange in which PSSAmC16 is soluble. These kind of antimicrobial polymers are known as biocide-releasing polymers. However, in the case of PVCHAM (the biocidal quaternized ammonium group is attached to the polymer chain by covalent bond) there is not release to the NaCl solution due to insolubility. When the release study is performed in ethanol solutions, the biocidal polymer is expelled out the polymer matrix and detected by both, absorption and SERS measurements.

Overall, UV-Vis and SERS methodologies constitute a powerful combination, enabling us to discriminate the polymeric PSS backbone and the electrostatically bound AmC16 species, as well as to discriminate between electrostatically bound and covalently attached PVBCHAM species. This is of utmost importance for the development of antimicrobial polymeric materials containing both ionically bound and covalently attached biocidal quaternary ammonium units, achieving thus a dual functionality in a single component polymeric design.

Acknowledgements

This research has been co-financed by the European Union (European Social Fund – ESF) and Greek national funds through the Operational Program 'Education and Lifelong Learning' of the National Strategic Reference Framework (NSRF) – Research Funding Program: THALES. Investing in knowledge society through the European Social Fund. Project title: 'Development of Novel Functional Copolymers and Surfaces with Permanent and/or Controlled released biocidal species' (MIS: 379523).

References

[1] Muñoz-Bonilla A., Fernandez-Garcia M.: Polymeric materials with antimicrobial activity. Progress in Polymer Science, **37**, 281–339 (2012). DOI: 10.1016/j.progpolymsci.2011.08.005

[2] Muñoz-Bonilla A., Fernandez-Garcia M.: The roadmap of antimicrobial polymeric materials in macromolecular nanotechnology. European Polymer Journal, **65**, 46–62 (2015). DOI: 10.1016/j.eurpolymj.2015.01.030

[3] Gilbert P., Moore L. E.: Cationic antiseptics: Diversity of action under a common epithet. Journal of Applied Microbiology, **99**, 703–715 (2005). DOI: 10.1111/j.1365-2672.2005.02664.x

[4] Saif M. J., Anwar J., Munawar M. A.: A novel application of quaternary ammonium compounds as antibacterial hybrid coating on glass surfaces. Langmuir, **25**, 377–379 (2009). DOI: 10.1021/la802878p

[5] Oikonomou E. K., Iatridi Z., Moschakou M., Damigos P., Bokias G., Kallitsis J. K.: Development of Cu_2^+- and/or phosphonium-based polymeric biocidal materials and their potential application in antifouling paints. Progress in Organic Coatings, **75**, 190–199 (2012). DOI: 10.1016/j.porgcoat.2012.04.019

[6] Xue Y., Xiao H., Zhang Y.: Antimicrobial polymeric materials with quaternary ammonium and phosphonium salts. International Journal of Molecular Sciences, **16**, 3626–3655 (2015). DOI: 10.3390/ijms16023626

[7] Kanazawa A., Ikeda T., Endo T.: Polymeric phosphonium salts as a novel class of cationic biocides. II. Effects of counter anion and molecular weight on antibacterial activity of polymeric phosphonium salts. Journal of Polymer Science Part A: Polymer Chemistry, **31**, 1441–1447 (1993). DOI: 10.1002/pola.1993.080310611

[8] Wolff M. O., Alexander K. M., Belder G.: Uses of quaternary phosphonium compounds in phase transfer catalysis. Chimica Oggi, **18**, 29–32 (2000).

[9] Bradaric C. J., Downard A., Kennedy C., Robertson A. J., Zhou Y.: Industrial preparation of phosphonium ionic liquids. Green Chemistry, **5**, 143–152 (2003). DOI: 10.1039/B209734F

[10] Koromilas N. D., Lainioti G. C., Oikonomou E. K., Bokias G., Kallitsis J. K.: Synthesis and self-association in dilute aqueous solution of hydrophobically modified polycations and polyampholytes based on 4-vinylbenzyl chloride. European Polymer Journal, **54**, 39–51 (2015). DOI: 10.1016/j.eurpolymj.2014.02.009

[11] Guo A., Wang F., Lin W., Xu X., Tang T., Shen Y., Guo S.: Evaluation of antibacterial activity of *N*-phosphonium chitosan as a novel polymeric antibacterial agent. International Journal of Biological Macromolecules, **67**, 163–171 (2014). DOI: 10.1016/j.ijbiomac.2014.03.024

[12] Kenawy E-R., Abdel-Hay F. I., El-Shanshoury A. E. R. R., El Newehy M. H.: Biologically active polymers. V. Synthesis and antimicrobial activity of modified poly (glycidyl methacrylate-*co*-2-hydroxyethyl methacrylate) derivatives with quaternary ammonium and phosphonium salts. Journal of Polymer Science Part A: Polymer Chemistry, **40**, 2384–2393 (2002). DOI: 10.1002/pola.10325

[13] Costerton J. W., Stewart P. S., Greenberg E. P.: Bacterial biofilms: A common cause of persistent infections. Science, **284**, 1318–1322 (1999). DOI: 10.1126/science.284.5418.1318

[14] Yu Q., Wu Z., Chen H.: Dual-function antibacterial surfaces for biomedical applications. Acta Biomateriala, **16**, 1–13 (2015). DOI: 10.1016/j.actbio.2015.01.018

[15] Mi L., Jiang S.: Integrated antimicrobial and nonfouling zwitterionic polymers. Angewandte Chemie International Edition, **53**, 1746–1754 (2014). DOI: 10.1002/anie.201304060

[16] Manikas A. C., Soto Beobide A., Voyiatzis G. A.: Quantitative analysis *via* surface enhanced Raman Scattering from Ag nano-colloids utilizing an oscillating cell and right-angle collection geometry. Analyst, **134**, 587–592 (2009). DOI: 10.1039/B815053B

[17] Anastasopoulos J. A., Soto Beobide A., Voyiatzis G. A.: Quantitative surface enhanced Raman scattering measurements at the early stage of active agent release processes. Journal of Raman Spectroscopy, **44**, 401–405 (2013). DOI: 10.1002/jrs.4222

[18] Bekiari V., Nikolaou K., Koromilas N., Lainioti G., Avramidis P., Hotos G., Kallitsis J. K., Bokias G.: Release of polymeric biocides from synthetic matrices for marine biofouling applications. Agriculture and Agricultural Science Procedia, **4**, 445–450 (2015). DOI: 10.1016/j.aaspro.2015.03.051

[19] Koromilas N. D., Lainioti G. Ch., Gialeli Ch., Barbouri D., Kouravelou K. D., Karamanos N. K., Voyiatzis G. A., Kallitsis J. K.: Preparation and toxicological assessment of functionalized carbon nanotube-polymer hybrids. Plos One, **9**, e107029/1–e107029/15 (2014). DOI: 10.1371/journal.pone.0107029

[20] Lee P. C., Meisel D.: Adsorption and surface-enhanced Raman of dyes on silver and gold sols. The Journal of Physical Chemistry, **86**, 3391–3395 (1982). DOI: 10.1021/j100214a025

[21] Simomcic B., Tomsic B.: Structures of novel antimicrobial agents for textiles – A review. Textile Research Journal, **80**, 1721–1737 (2010).
DOI: 10.1177/0040517510363193

[22] Kougia E., Tselepi M., Vasilopoulos G., Lainioti G. C., Koromilas N. D., Druvari D., Bokias G., Vantarakis A., Kallitsis J. K.: Evaluation of antimicrobial efficiency of new polymers comprised by covalently attached and/or electrostatically bound bacteriostatic species, based on quaternary ammonium compounds. Molecules, **20**, 21313–21327 (2015).
DOI: 10.3390/molecules201219768

[23] Dendramis A. L., Schwinn E. W., Sperline R. P.: A surface-enhanced Raman scattering study of CTAB adsorption on copper. Surface Science, **134**, 675–688 (1983).
DOI: 10.1016/0039-6028(83)90065-1

[24] Papanu J. S., Hess D. W., Soane D. S., Bell A. T.: Swelling of poly(methyl methacrylate) thin films in low molecular weight alcohols. Journal of Applied Polymer Science, **39**, 803–823 (1990).
DOI: 10.1002/app.1990.070390404

eXPRESS Polymer Letters Vol.10, No.9 (2016) 762–770
Available online at www.expresspolymlett.com
DOI: 10.3144/expresspolymlett.2016.70

Carbazole based electrochromic polymers with benzoazole units: Effect of heteroatom variation on electrochromic performance

C. Doyranli[1,2], *F. Baycan Koyuncu*[1,2*]

[1]Department of Chemistry, Faculty of Sciences and Arts, Çanakkale Onsekiz Mart University, 17020 Çanakkale, Turkey
[2]Polymeric Materials Research Laboratory, Çanakkale Onsekiz Mart University, 17020 Çanakkale, Turkey

Received 26 February 2016; accepted in revised form 5 April 2016

Abstract. A series of carbazole-based polymers were synthesized via Suzuki polymerization between N-(2-ethylhexyl)carbazole-3,6-bis(ethyleneboronate) (**Cbz**) and dibromobenzazole unit. Three different polymers, **PCBN**, **PCBS** and **PCBSe** were obtained from 4,7-dibromo-2-hexyl-2H-benzotriazole (**BN**), 4,7-dibromo-2,1,3-benzothiadiazole- (**BS**) and 4,7-dibromo-2,1,3-benzoselenadiazole (**BSe**), respectively. It is observed that, the variation of heteroatoms (N,S and Se) on the benzazole unit have most important effect on electro-optic properties of the **PCBX** polymers. Neutral state color of the polymer films and their electrochromic performances are also influenced. Among the synthesized polymers, the **PCBS** bearing 2,1,3-benzothiadiazole as acceptor units has a broad absorption and 50% of ΔT in the near-IR regime at the oxidized state. This property of **PCBS** is a great advantage for near-IR electrochromic applications.

Keywords: *polymer synthesis, molecular engineering, electrochromic polymers, carbazole, benzotriazole, benzothiadiazole*

1. Introduction

For 20 years, the donor-acceptor electrochromic polymers have been intensively studied owing to their respectable properties such as their tunable band gaps, and also electrochemical and optical properties. A reversible and visual color change called as electrochromism is obtained by the reversible redox behavior of the electroactive polymers. Electron-donor and electron-withdrawing parts are attached on the same polymer backbone of the donor–acceptor systems [1]. HOMO–LUMO energy levels of these systems are recognized exactly due to their dual electrochemical properties. These polymers have also an important charge transfer band in the neutral state to apply on the photovoltaic and electroluminescent devices. They also can be used in electrochromic materials to fabricate smart windows [2, 3], switchable mirrors [4, 5] and camouflage materials [6, 7].

Carbazole is one of the widely used donor moieties in the donor-acceptor systems as it can be functionalized at different positions such as (3,6) [8], (2,7) [9] or N-positions [10]. It is also an efficient blue emissive polymer in the organic light emitting diodes [11]. Owing to their effective carrier transport properties, carbazole based polymers can form relatively stable cations (polarons) and dications (bipolarons) when applying positive potential or doping agent [12]. Because of these superior properties, these polymers can be used in electrochromic materials, light emitting diodes, electrophotography and as photovoltaic constituents [9, 13–15]. Nevertheless, organic optoelectronic applications of poly-3,6-carbazoles are limited because of both poor conjugation within the polymer backbone and also not obtaining high molecular weights. Therefore, poly-3,6-carbazoles are still used as host materials because of

*Corresponding author, e-mail: fatmabaycan@hotmail.com

their high ability of hole transporting [16–18]. Besides, these polymers demonstrate remarkable electrochromic properties due to the conjugation broken on the carbazyl nitrogen. One of the exciting multicolor polymer frameworks based on the 3,6-linked carbazole moiety was proposed by Reynolds and coworkers [18–20]. These polymers can form radical cations that are separated from each other owing to the broken conjugation on the polymer backbone. When applying higher potentials on the polymer, radical dications (bipolarons) are formed in the polymer system via removing another electron. For these reasons, electrochromic materials containing poly(3,6)carbazole derivatives have multielectrochromic behavior due to their district oxidation property in the anodic regime [21, 22].

To understand the effect of heteroatom variation both on electro-optic properties of polymers and also on their electrochromic performance, we synthesized a series of donor-acceptor polymers based on N-(2-ethylhexyl)carbazole-3,6-bis(ethyleneboronate) (**Cbz**) and dibromobenzazole unit (BX)with different heteroatoms (N, S and Se) named as poly(4,7-(N-hexylbenzotriazole)-3,6-(N-(2-ethylhexyl)carbazole) (**PCBN**), poly(4,7-(2,1,3-benzothiadiazole)-3,6-(N-(2-ethylhexyl)carbazole) (**PCBS**) and poly(4,7-(2,1,3-benzoselenadiazole)-3,6-(N-(2-ethylhexyl)carbazole) (**PCBSe**). The band gap of polymers and also the neutral state color of the films can be tuned by attaching a heteroatom on the acceptor moiety, changing nitrogen to sulfur or selenium. Further, owing to multi step redox behavior at the anodic regime, various colors were obtained on the polymer films upon applied potentials. Among the **PCBX** polymers, **PCBS** has a broad absorption and 50% of ΔT in the near-IR regime at the oxidized state. Owing to this property, **PCBS** can be a good candidate to use for near-IR electrochromic applications.

2. Experimental section

2.1. Materials

Compounds were procured from Aldrich. The initial compounds (Cbz, BN, BS and BSe) were prepared and characterized according to the literature [23].

2.2. Instrumentation

Fourier transform infrared spectra (FT-IR) were recorded on a Perkin Elmer FT-IR Spectrum One spectrometer by using an attenuated total reflectance (ATR) module (4000–650 cm^{-1}). ^{1}H-NMR spectra were recorded on a Bruker Advance DPX-400 at 25 °C in deuterated chloroform solutions with tetramethylsilane (TMS) as internal standard. Electrochemical analyses were performed by Biologic SP50 potentiostat–galvanostat system with a platinum disk (0.02 cm^2) as working electrode (WE), Ag wire as reference electrode (RE) and Pt wire as counter electrode (CE). UV-vis absorption spectra were recorded by an Analytic Jena Speedcord S-600 diode-array spectrophotometer. The optical band gaps (E_g) of polymers were found from their absorption onsets [24]. The emission spectra measurements were taken by a PTI QM1 fluorescence spectrophotometer. Spectroelectrochemical measurements were carried out to consider absorption spectra of polymer films under applied potential. The color coordinates are determined by three characteristics; luminance (L), hue (a), and saturation (b) in Commission Internationale de l'Elcairage (CIE) system [25]. To determine these characteristics, Analytic Jena UV–vis spectrophotometer containing a chromameter module was used. GPC analysis of the polymers was performed with Agilent 1260 HPLC instrument. This system consists of an Agilent 1200 series pump, three Waters Styragel HR columns (guard, 4, 3) and a BI-DNDC differential refractometer (Brookhaven Instruments Corporation, 620 nm) with a THF flow rate of 1 mL/min. Polystyrene was used as calibration standard. Surface morphologies were investigated by Nanosurf Naio AFM.

2.3. Synthesis of PCBX polymers

The polymers were synthesized via Suzuki polymerization reaction between 2-ethylhexyl-9H-carbazole-3,6-diboronicacidbis(1,3-propanediole) ester and dibromo benzoazole-based heterocycles. Benzoazoledibromide (1 mol) and 2-ethylhexyl-9H-carbazole-3,6-diboronic acid bis(1,3-propanediole) ester (1 mol) were added into potassium carbonate solution (K_2CO_3, 2M in H_2O) and 20 mL toluene. Then, $Pd(PPh_3)_4$ (5 mol%) was added to flask. The mixture was heated to 110 °C and refluxed for 16 h under N_2. For ending the reaction benzeneboronic acid (0.122 mol) was added and refluxed about 3 h and then bromobenzene (0.122 mol) was also put into flask and stirred for 3 h, too. Lastly, the mixture was cooled and then

filtered. After that, it poured into methyl alcohol. The crude product was filtered again and dried. Soxhlet extraction was achieved with methyl alcohol and then $CHCl_3$ for the last purification.

PCBN (*Yield 78%; yellow powder*): FTIR [cm^{-1}]: *3094* (*C–H aromatic*); *2957*, *2931*, *2856* (*C–H aliphatic*); *1615* (*C=N*); *1595*, *1530* (*C=C aromatic*); 1443 (C–N); ^{1}H-NMR (*$CHCl_3$-d*): *δ ppm*, *8.84–7.17* (*m*, *8H*, *C–H aromatic*); *4.81* (*m*, *2H*, *–NCH_2–*, *triazole*); *4.52* (*m*, *2H*, *–NCH_2–*, *carbazole*); *2.17–1.33* (*m*, *17H*, *C–H aliphatic*); *0.91* (*m*, *9H*, *–CH_3*).

PCBS (*Yield 86%; orange powder*): FTIR [cm^{-1}]: *3086* (*C–H aromatic*); *2954*, *2929*, *2850* (*C–H aliphatic*); *1612* (*C=N*); *1578*, *1524* (*C=C aromatic*); *1441* (*C–N*); ^{1}H-NMR (*$CHCl_3$-d*): *δ ppm*, *8.82–7.48* (*m, 8H*, *C–H aromatic*); *4.29* (*m*, *2H, –NCH_2–*); *2.19–1.38* (*m, 9H*, *C–H aliphatic*); *0.91* (*m*, *6H*, *–CH_3*).

PCBSe (*Yield 82%*; *red powder*): FTIR [cm^{-1}]: *3084* (*C–H aromatic*); *2950*, *2925*, *2796* (*C–H aliphatic*); *1610* (*C=N*); *1574, 1522* (*C=C aromatic*); *1440* (*C–N*); ^{1}H-NMR (*$CHCl_3$-d*): *δ ppm*, *8.71–7.16* (*m*, *8H*, *C–H aromatic*); *4.29* (*m, 2H*, *–NCH_2–*); *2.15–1.39* (*m*, *9H*, *C–H aliphatic*); *0.91* (*m*, *6H*, *–CH_3*).

3. Results and discussion

3.1. Synthesis of PCBX polymers

Cbz, BN, BS and BSe were synthesized according to procedures from the literature [23]. Syntheses of the polymers (PCBN, PCBS and PCBSe) were achieved by Suzuki reaction between Cbz-donor and BX-acceptors respectively (Figure 1). FTIR and ^{1}H-NMR analysis were used to prove the formation of the PCBX polymers. Noteworthy, spectral properties variations were detected for initial and the final compounds. According to ^{1}H-NMR spectra of polymers, carbazole and benzazole aromatic proton signals were observed 8.84–7.16 ppm. Because of the electron-acceptor effect of carbazyl nitrogen, N–CH_2 aliphatic group signal was detected at higher ppm, (4.52 ppm for PCBN – 4.29 ppm for PCBS and PCBSe) than that of other aliphatic protons (Figure 2). The similar situation was also observed in the benzotriazole's N–CH_2 aliphatic signal (4.81 ppm).

GPC was used for the investigation of polydispersity index (PDI) and molecular weight of the polymers. According to GPC measurements, degree of polymerization of PCBX polymers was found to be 7, 6 and 4 respectively (Table 1). The results obtained indicate that these molecules are oligomers. Because of the presence of an alkyl chain on the benzotriazole moiety, the molecular weight of PCBN higher than that of the other polymers.

3.2. Optical properties of PCBX polymers

The optic characterization of **PCBX** polymers were achieved by UV-Vis and Fluorescence spectroscopy. Owing to π-π* transitions arising from the conjugation of the polymer main chain, PCBX polymers showed absorption bands at about 300 nm. Besides, because of the interaction of carbazole-donor and benzazole-acceptor at the conjugated polymer system, a typical charge transport band was obtained at 360 nm for **PCBN**, at 440 nm for **PCBS** and at 475 nm for **PCBSe**, respectively (Figure 2a). Finally,

Table 1. Molecular weights of PCBN, PCBS and PCBSe

Polymer	M_n [Da]	M_w [Da]	PDI
PCBN	3339	4768	1.42
PCBS	2516	3632	1.44
PCBSe	1626	2031	1.24

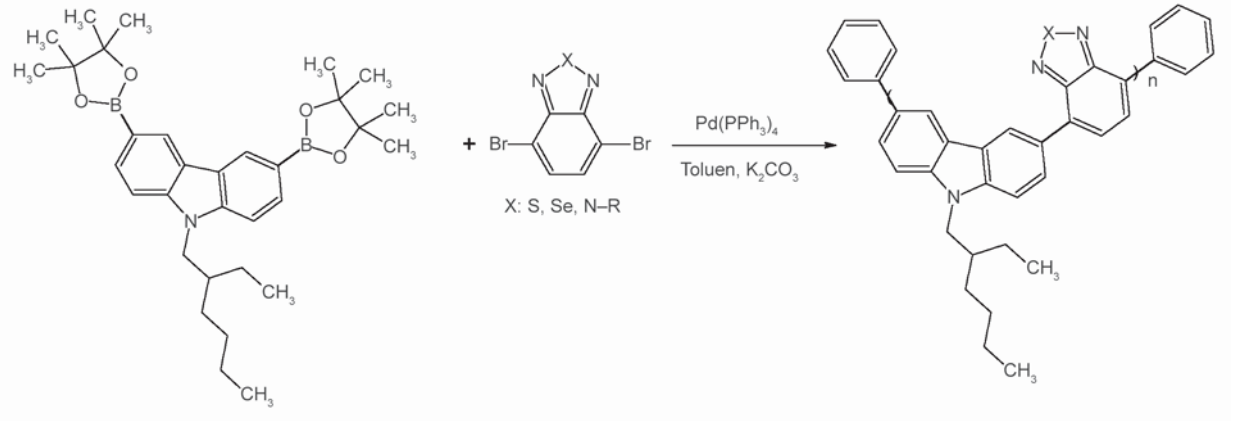

Figure 1. Synthetic route for PCBX polymers

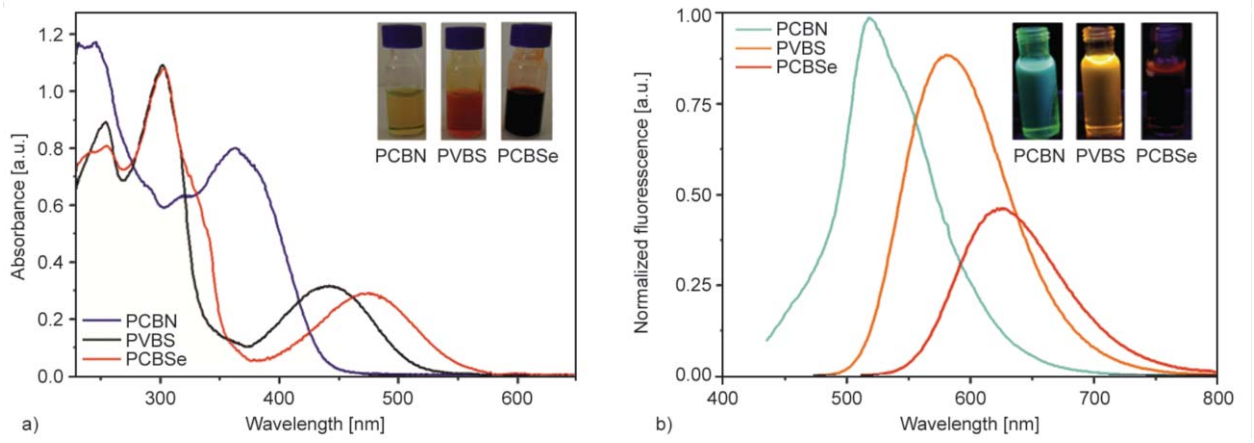

Figure 2. Absorption (a) and fluorescence (b) spectra of PCBX polymers in CH_2Cl_2 solution

the optical band gaps were found to be 2.80 eV for **PCBN** (at 442 nm), 2.42 eV for **PCBS** (at 513 nm) and 2.18 eV for **PCBSe** (at 569 nm) respectively. According to this result, there is about 127 nm bathochromic shift from **PCBN** to **PCBSe**. On the other hand, similar results were observed in the fluorescence measurements. Upon **PCBXs** excited from absorption maxima of their charge transfer band (λ_{max} = 360 nm for PCBN, λ_{max} = 440 nm for PCBS, and λ_{max} = 475 nm for PCBSe) strong emission bands were obtained at 440, 580, and 623 nm with Stokes' shifts of 157, 140, and 148 nm, respectively (Figure 2b). The emission colors of the polymer solutions were diverse as cyan, orange and red, respectively. Finally, absorption and fluorescence behavior could be arranged by the substitution of different heteroatoms on the benzazole acceptor moiety to carbazole donor unit.

3.3. Electrochemical properties of PCBX polymers

To understand the redox behaviors of **PCBX** polymers, cyclic voltammetry (CV) technique was used. **PCBN**, **PCBS** and **PCBSe** have a great difference in their redox properties obtained from the CV voltamograms which are shown in Figure 3. The electron-deficient character of the heteroatom on the benzazole moiety strongly affected the reduction potentials of the polymers in the cathodic regime. **PCBN**, **PCBS** and **PCBSe** polymers have an irreversible reduction peak at –1.65, –1.50 and –1.42 V, respectively. According to these results, changing the electron-deficient unit of the polymer significantly altered the reduction potential of the polymers. Thus, LUMO levels responded differently and consequently **PCBSe** has a lower band gap value compared with **PCBS** and PCBN because of the stronger electron-withdrawing character of benzoselenadiazole moiety [26–28].

On the other hand, semi reversible oxidation peaks were found at $E^{ox}_{p,a}$ = 1,35 V, $E^{ox}_{p,c}$ =1.01 V and $E^{ox}_{p,1/2}$ = 1.18 V for **PCBN**; $E^{ox}_{p,a}$ = 1,26 V, $E^{ox}_{p,c}$ =0.98 V and $E^{ox}_{p,1/2}$ = 1.12 V for **PCBS**, $E^{ox}_{p,a}$ = 1,58 V, $E^{ox}_{p,c}$ =1.05 V and $E^{ox}_{p,1/2}$ = 1.32 V for **PCBSe** in the anodic region. According to Table 2, it can be deduced that electrochemical and optical behaviors of the polymers were significantly affected by varying the heteroatom on the acceptor moiety attached to the carbazole-donor main chain.

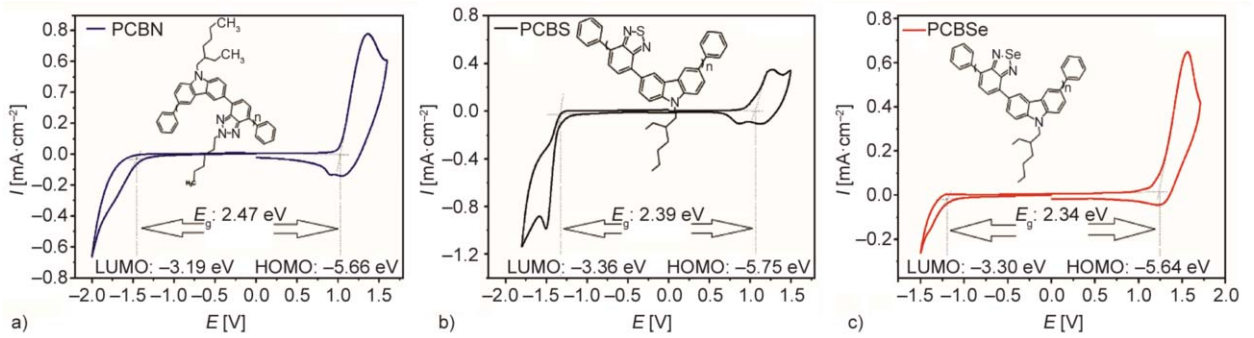

Figure 3. Redox behavior of PCBN (a) PCBS (b) and PCBSe (c) in 0.1 M $TBAPF_6/CH_2Cl_2$ electrolyte solution at scan rate 100 mV/s, vs. Ag wire

Table 2. HOMO-LUMO, electrochemical and optical band gaps (E_g) of PCBX polymers

Polymer	HOMO [eV]	LUMO [eV]	Optical E_g [eV]	Electrochemical E_g [eV]
PCBN	–5.66	–3.19	2.80	2.47
PCBS	–5.75	–3.36	2.42	2.39
PCBSe	–5.64	–3.30	2.18	2.34

3.4. Surface morphologies

Morphology of **PCBN**, **PCBS** and **PCBSe** film surfaces was examined by atomic force microscopy (AFM) (Figure 4). Polymer solutions were obtained from 20 mg/mL of PCBX in $CHCl_3$. PCBX polymer films were prepared by using spin-casting method on ITO substrates at 2000 rpm for 60 s from the polymer solutions. While the thickness of the films were calculated as 96, 168 and 190 nm, for **PCBN**, **PCBS** and **PCBSe** respectively, the RMS (root mean surface) roughness of polymers are found to be 10.38, 18.87 and 25.45 nm. The AFM image of the PCBS and PCBSe exhibit conglomerate non-uniform structure and the roughness of these polymer films are high. Besides, PCBN has a longer side alkyl chain on the benzotriazole acceptor moiety. Because of this, solvation is promoted by increasing the length of the alkyl chain. As a result of increasing the solubility and also expansion of π conjugation along the polymer backbone, a uniform surface could be obtained. Consequently, better polymer thin films could be obtained by decreasing the roughness [29, 30]. As known in the literature [31–33] during electrochromic switching, the electrolyte ions are injected/ejected to the polymer film surface. Because of the feature, the electrochromic performance of the PCBX polymer was affected by the polymer film surface roughness.

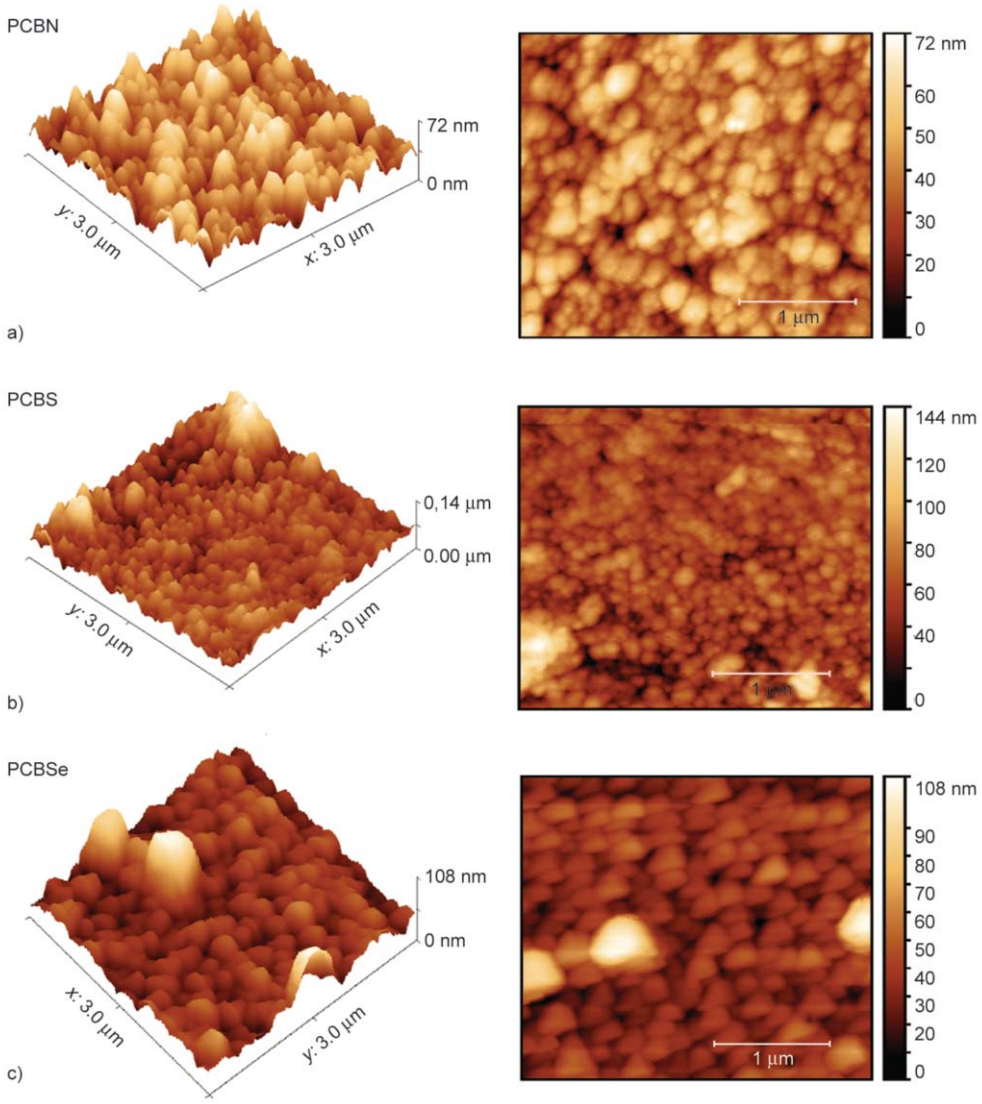

Figure 4. AFM image of PCBN (a), PCBS (b) and PCBSe (c) onto ITO/glass surface

3.5. Spectroelectrochemical properties of PCBX polymers

Spectroelectrochemical investigation of **PCBN**, **PCBS** and **PCBSe** films was carried out via Diode-array UV-Vis spectrophotometer. While oxidation of **PCBN** film (0–1.2 V), an absorption band at 360 nm corresponds to valence band-conduction band ($\pi \rightarrow \pi^*$ transition) started to decrease and another band intensified at 550 nm. This new absorption band pointed out the formation of polaron on the carbazole based polymer chain and thus light yellow neutral state color of the film (L: 78.7; a: –13.5; b: 47.8) converted to green (L: 71.5; a: –27.5; b: 56.9). Additionally, upon applied higher potentials (1.2–1.8 V), another new band was observed in the near-IR region (at 860 nm) as a result of the formation of a bipolaron. Consequently, the color of the **PCBN** polymer film turned into red (L: 39.01; a: 4.98; b: 4.54) at fully oxidized state (Figure 5).

Anodic scan of PCBS (0 to 1.8 V) (Figure 6), the charge transfer band at 455 nm decreased, and two new absorption bands were started to form at 600 nm (0–1.4 V) and 825 nm (1.4–1.8 V) (Figure 5). Moreover, formation of polaron and bipolaron on the **PCBS** polymer backbone was verified by the intensification of the broad band in the visible and near-IR regime (Figure 5). While the orange color of the film at neutral state (L: 69.57; a: 5.66; b: 56.67) changed to blue (L: 24.9; a: 3.6; b: –28.7) and then black (L: 39.08; a: –0.4; b: –1.25) upon the applied positive potential (Figure 6).

Further, red color **PCBSe** polymer film (L: 42.6; a: 28.6; b: 32.6) was exhibited a maximum absorption band at 475 nm (λ_{max}, the charge transfer band) at the neutral state. During to anodic scan (Figure 7), intensity of $\pi \rightarrow \pi^*$ transition and charge transfer bands were decreased. On the other hand, new absorption bands at about 650 nm (0–1.4 V) and 800 nm (1.4–1.8 V) started to be intensified depending on the formation of polarons and bipolarons, respectively (Figure 7). Hence, above 700 nm (the Near-IR region) was intensely absorbed by the **PCBSe** polymer film at fully oxidized state. According to these results, the red polymer film converted to oily green (L: 34.5; a: –11.7; b: 16.5), and dark blue (L: 29.6; a: –2.98; b: –11.7), respectively (Figure 7).

Kinetic performance of **PCBX** polymers was carried out by the square-wave voltammetry which observes the difference of transmittance at the point of absorption maxima against to time while applying voltage between redox states of polymers with a residence time of 10 s (Figure 7). The percentage transmittance change ($\Delta T\%$) of PCBX polymers was investigated between 0–1.8 V with switching time of 10 s. As a result of these measurements, $\Delta T\%$ was found to be 21% for **PCBN** at 860 nm, 45% for **PCBS** at 825 nm

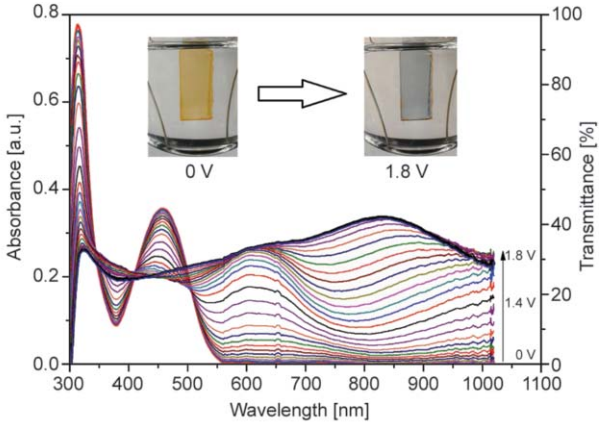

Figure 6. Color changes and spectroelectrochemistry of PCBS film on ITO in the anodic region

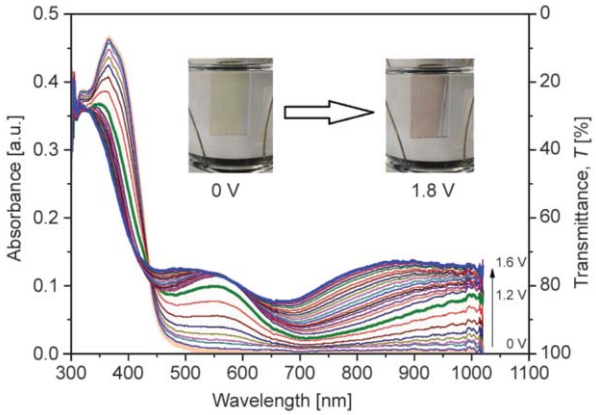

Figure 5. Color changes and spectroelectrochemistry of PCBN film on ITO in the anodic region

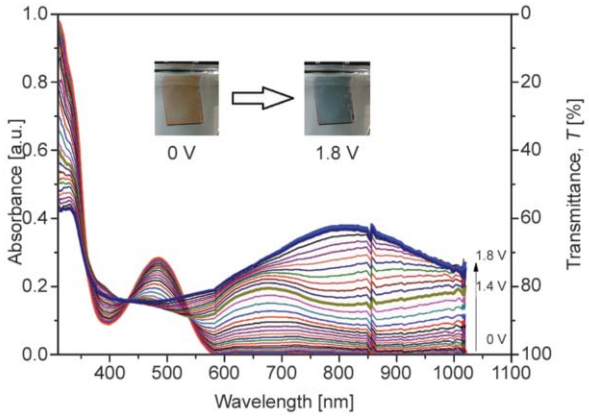

Figure 7. Color changes and spectroelectrochemistry of PCBSe film on ITO in the anodic region

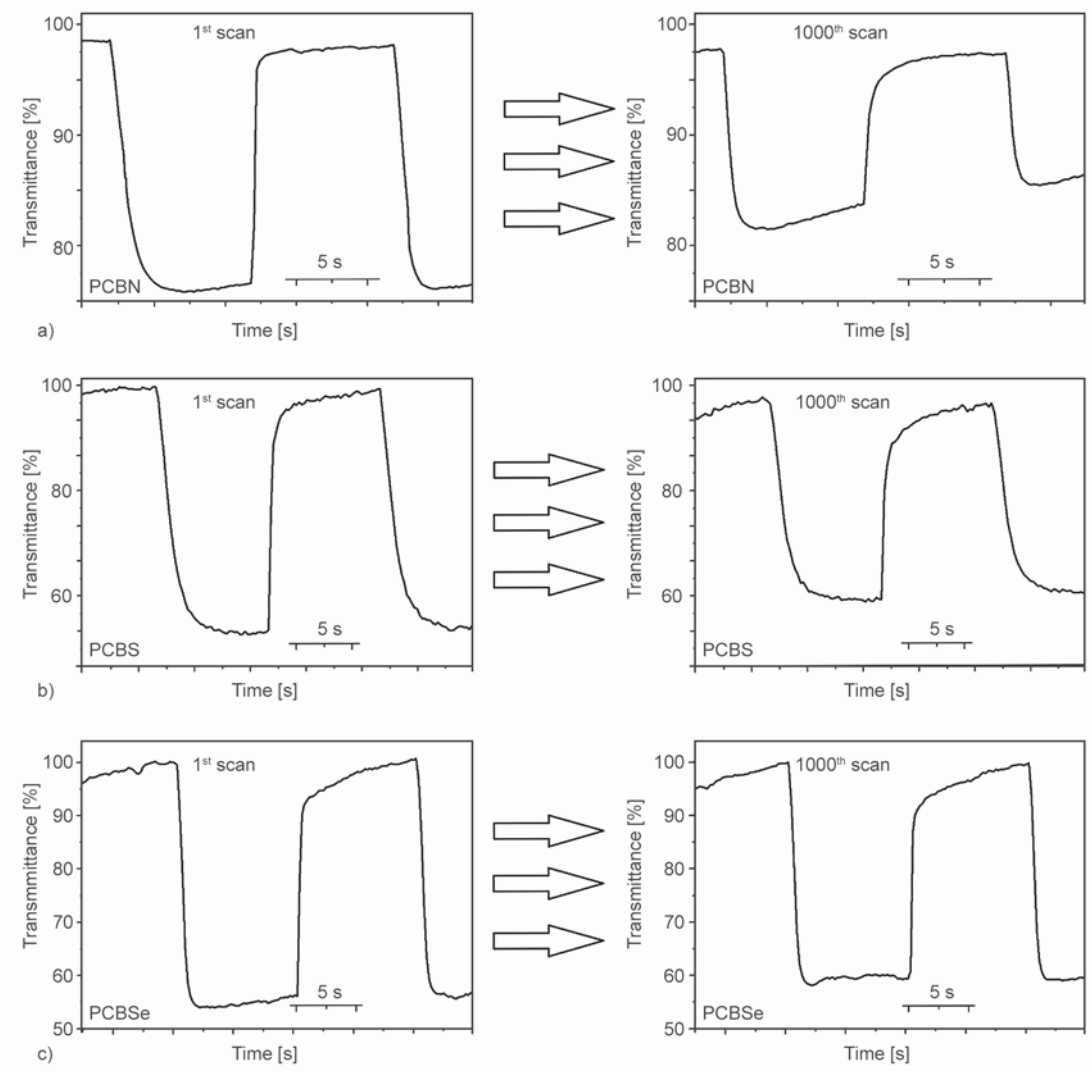

Figure 8. Stability test of polymers. [Optical difference watched at 860 nm for PCBN (a), 825 nm for PCBS (b) and 800 nm for PCBSe between 0 and 1.8 V (c)]

and 41% for **PCBN** at 800 nm respectively (Figure 8).

Optical activity is one of the most significant parameter to determine the electrochromic performance of the polymer films [34]. While **PCBN** has 62% of the optical activity, **PCBS** and **PCBSe** have 84% and 86% of the optical activity after 1000 cycles, respectively. The reduction and oxidation response times were also determined. The values were found to be 4.8 and 1.2 s for **PCBN**, 2.4 and 6.1 s for **PCBS**, and 1.8 and 2.4 s for **PCBSe** respectively.

Another important parameter is coloration efficiency (CE) for the electrochromic applications. CE was determined via the equation: $CE = \Delta OD/Q_d$ and $\Delta OD = \log(T_{colored}/T_{bleached})$ [where $T_{bleached}$ is transmittance at neutral state, $T_{colored}$ is transmittance at oxidized state and Q_d is Injected/ejected charge between redox states] [25]. According to this equation, CE values of **PCBN**, **PCBS** and **PCBSe** were determined as 93, 178 and 154 $cm^2 \cdot °C^{-1}$ respectively. As it can be clearly observed, CE values of **PCBS** and **PCBSe** are approximately two times greater than that of **PCBN**. Considering all data, electrochromic performance of the polymers was significantly affected by the type of heteroatom on the benzoazole acceptor moiety. Finally, **PCBN**, **PCBS** and **PCBSe** polymer films exhibited multi-electrochromic behavior, reasonable response time and optical contrast. Furthermore, **PCBS** has a broad absorption band in both the visible and near-IR regime at its oxidized state. Consequently, it could be a good candidate to use a visible and near-IR filter in various applications.

4. Conclusions

In this work, a series of carbazole based electrochromic polymers with benzazole moiety as electron-acceptor were synthesized and characterized. Besides, the heteroatom variation effects on the analogous electrochromic polymers were also investigated. The polymer thin films of PCBX were obtaining by using spin-casting metod. They have several colors presented for the neutral and polaronic species, owing to multiple redox behavior of carbazole moiety at their oxidized state. The neutral state color of PCBX polymers were yellow, orange and red, respectively. On the other hand, the color of the films converted to red, black and dark blue at fully oxidized state, respectively. In conclusion, electrochromic polymers **PCBN**, **PCBS** and **PCBSe** exhibit medium band gaps (2.47, 2.39 and 2.34 eV) and reasonable electrochromic performance (optical activity, coloration efficiency and oxidation/reduction times).

Acknowledgements

The authors would like thank Çanakkale Onsekiz Mart University for financial support (Project Number: 2015/56).

References

[1] Shirota Y.: Organic materials for electronic and optoelectronic devices. Journal of Materials Chemistry, **10**, 1–25 (2000).
DOI: 10.1039/a908130e

[2] Niklasson G. A., Granqvist C. G.: Electrochromics for smart windows: Thin films of tungsten oxide and nickel oxide, and devices based on these. Journal of Materials Chemistry, **17**, 127–156 (2007).
DOI: 10.1039/b612174h

[3] Granqvist C. G., Azens A., Hjelm A., Kullman L., Niklasson G. A., Rönnow D., Mattsson M. S., Veszelei M., Vaivars G.: Recent advances in electrochromics for smart windows applications. Solar Energy, **63**, 199–216 (1998).
DOI: 10.1016/S0038-092X(98)00074-7

[4] Mortimer R. J.: Electrochromic materials. Chemical Society Reviews, **26**, 147–156 (1997).
DOI: 10.1039/cs9972600147

[5] Rosseinsky D. R., Mortimer R. J.: Electrochromic systems and the prospects for devices. Advanced Materials, **13**, 783–793 (2001).
DOI: 10.1002/1521-4095(200106)13:11<783::AID-ADMA783>3.0.CO;2-D

[6] Chandrasekhar P., Zay B., Birur G. C., Rawal S., Pierson E. A., Kauder L., Swanson T.: Large, switchable electrochromism in the visible through far-infrared in conducting polymer devices. Advanced Functional Materials, **12**, 95–103 (2002).
DOI: 10.1002/1616-3028(20020201)12:2<95::AID-ADFM95>3.3.CO;2-E

[7] Beaupré S., Breton A-C., Dumas J., Leclerc M.: Multicolored electrochromic cells based on poly(2,7-carbazole) derivatives for adaptive camouflage. Chemistry of Materials, **21**, 1504–1513 (2009).
DOI: 10.1021/cm802941e

[8] Zhang Z-B., Fujiki M., Tang H-Z., Motonaga M., Torimitsu K.: The first high molecular weight poly(*N*-alkyl-3,6-carbazole)s. Macromolecules, **35**, 1988–1990 (2002).
DOI: 10.1021/ma011911b

[9] Blouin N., Michaud A., Gendron D., Wakim S., Blair E., Neagu-Plesu R., Belletête M., Durocher G., Tao Y., Leclerc M.: Toward a rational design of poly(2,7-carbazole) derivatives for solar cells. Journal of the American Chemical Society, **130**, 732–742 (2008).
DOI: 10.1021/ja0771989

[10] Watanabe T., Ueda S., Inuki S., Oishi S., Fujii N., Ohno H.: One-pot synthesis of carbazoles by palladium-catalyzed *N*-arylation and oxidative coupling. Chemical Communications, **43**, 4516–4518 (2007).
DOI: 10.1039/b707899d

[11] Thomas K. R. J., Lin J. T., Tao Y-T., Ko C-W.: Light-emitting carbazole derivatives: Potential electroluminescent materials. Journal of the American Chemical Society, **123**, 9404–9411 (2001).
DOI: 10.1021/ja010819s

[12] Pomerantz Z., Zaban A., Ghosh S., Lellouche J-P., Garcia-Belmonte G., Bisquert J.: Capacitance, spectroelectrochemistry and conductivity of polarons and bipolarons in a polydicarbazole based conducting polymer. Journal of Electroanalytical Chemistry, **614**, 49–60 (2008).
DOI: 10.1016/j.jelechem.2007.11.005

[13] Liou G-S., Hsiao S-H., Huang N-K., Yang Y-L.: Synthesis, photophysical, and electrochromic characterization of wholly aromatic polyamide blue-light-emitting materials. Macromolecules, **39**, 5337–5346 (2006).
DOI: 10.1021/ma0608469

[14] Akcelrud L.: Electroluminescent polymers. Progress in Polymer Science, **28**, 875–962 (2003).
DOI: 10.1016/S0079-6700(02)00140-5

[15] Getautis V., Daskeviciene M., Malinauskas T., Gaidelis V., Jankauskas V., Tokarski Z.: Cross-linkable hydrazone-containing molecular glasses for electrophotography. Synthetic Metals, **155**, 599–605 (2005).
DOI: 10.1016/j.synthmet.2005.09.039

[16] Brunner K., van Dijken A., Börner H., Bastiaansen J. J. A. M., Kiggen N. M. M., Langeveld B. M. W.: Carbazole compounds as host materials for triplet emitters in organic light-emitting diodes: Tuning the HOMO level without influencing the triplet energy in small molecules. Journal of the American Chemical Society, **126**, 6035–6042 (2004).
DOI: 10.1021/ja049883a

[17] Tsai M-H., Lin H-W., Su H-C., Ke T-H., Wu C-C., Fang F-C., Liao Y-L., Wong K-T., Wu C-I.: Highly efficient organic blue electrophosphorescent devices based on 3,6-bis(triphenylsilyl)carbazole as the host material. Advanced Materials, **18**, 1216–1220 (2006).
DOI: 10.1002/adma.200502283

[18] Cirpan A., Argun A. A., Grenier C. R. G., Reeves B. D., Reynolds J. R.: Electrochromic devices based on soluble and processable dioxythiophene polymers. Journal of Materials Chemistry, **13**, 2422–2428 (2003). DOI: 10.1039/b306365h

[19] Witker D., Reynolds J. R.: Soluble variable color carbazole-containing electrochromic polymers. Macromolecules, **38**, 7636–7644 (2005).
DOI: 10.1021/ma050805x

[20] Schwendeman I., Hickman R., Sönmez G., Schottland P., Zong K., Welsh D., Reynolds J. R.: Enhanced contrast dual polymer electrochromic devices. Chemistry of Materials, **14**, 3118–3122 (2002).
DOI: 10.1021/cm020050y

[21] Wang H-M., Hsiao S-H., Liou G-S., Sun C-H.: Synthesis, photoluminescence, and electrochromism of polyamides containing (3,6-di-*tert*-butylcarbazol-9-yl)triphenylamine units. Journal of Polymer Science Part A: Polymer Chemistry, **48**, 4775–4789 (2010).
DOI: 10.1002/pola.24269

[22] Koyuncu F. B., Koyuncu S., Ozdemir E.: A novel donor–acceptor polymeric electrochromic material containing carbazole and 1,8-naphtalimide as subunit. Electrochimica Acta, **55**, 4935–4941 (2010).
DOI: 10.1016/j.electacta.2010.03.094

[23] Icli M., Pamuk M., Algi F., Önal A. M., Cihaner A.: Donor–acceptor polymer electrochromes with tunable colors and performance. Chemistry of Materials, **22**, 4034–4044 (2010).
DOI: 10.1021/cm100805g

[24] Patil A. O., Heeger A. J., Wudl F.: Optical properties of conducting polymers. Chemical Reviews, **88**, 183–200 (1988).
DOI: 10.1021/cr00083a009

[25] Thompson B. C., Schottland P., Sonmez G., Reynolds J. R.: *In situ* colorimetric analysis of electrochromic polymer films and devices. Synthetic Metals, **119**, 333–334 (2001).
DOI: 10.1016/S0379-6779(00)00863-8

[26] Das S., Pati P. B., Zade S. S.: Cyclopenta[*c*]thiophene-based D–A conjugated copolymers: Effect of heteroatoms (S, Se, and N) of benzazole acceptors on the properties of polymers. Macromolecules, **45**, 5410–5417 (2012).
DOI: 10.1021/ma3006697

[27] Shen P., Bin H., Zhang Y., Li Y.: Synthesis and optoelectronic properties of new D–A copolymers based on fluorinated benzothiadiazole and benzoselenadiazole. Polymer Chemistry, **5**, 567–577 (2014).
DOI: 10.1039/C3PY00968H

[28] Baran D., Oktem G., Celebi S., Toppare L.: Neutral-state green conjugated polymers from pyrrole bis-substituted benzothiadiazole and benzoselenadiazole for electrochromic devices. Macromolecular Chemistry and Physics, **212**, 799–805 (2011).
DOI: 10.1002/macp.201000744

[29] Zhang Q., Cirpan A., Russell T. P., Emrick T.: Donor–acceptor poly(thiophene-*block*-perylene diimide) copolymers: Synthesis and solar cell fabrication. Macromolecules, **42**, 1079–1082 (2009).
DOI: 10.1021/ma801504e

[30] Li Z., Zhang Y., Tsang S-W., Du J., Zhou J., Tao Y., Ding J.: Alkyl side chain impact on the charge transport and photovoltaic properties of benzodithiophene and diketopyrrolopyrrole-based copolymers. Journal of Physical Chemistry C, **115**, 18002–18009 (2011).
DOI: 10.1021/jp202996p

[31] Poverenov E., Li M., Bitler A., Bendikov M.: Major effect of electropolymerization solvent on morphology and electrochromic properties of PEDOT films. Chemistry of Materials, **22**, 4019–4025 (2010).
DOI: 10.1021/cm100561d

[32] Mortimer R. J., Graham K. R., Grenier C. R. G., Reynolds J. R.: Influence of the film thickness and morphology on the colorimetric properties of spray-coated electrochromic disubstituted 3,4-propylenedioxythiophene polymers. ACS Applied Materials and Interfaces, **10**, 2269–2276 (2009).
DOI: 10.1021/am900431z

[33] Neo W. T., Shi Z., Cho C. M., Chua S-J., Xu J.: Effects of chemical composition, film thickness, and morphology on the electrochromic properties of donor–acceptor conjugated copolymers based on diketopyrrolopyrrole. ChemPlusChem, **80**, 1298–1305 (2015).
DOI: 10.1002/cplu.201500182

[34] Cihaner A., Algi F.: A processable rainbow mimic fluorescent polymer and its unprecedented coloration efficiency in electrochromic device. Electrochimica Acta, **53**, 2574–2578 (2008).
DOI: 10.1016/j.electacta.2007.10.030

eXPRESS Polymer Letters Vol.10, No.9 (2016) 771–779
Available online at www.expresspolymlett.com
DOI: 10.3144/expresspolymlett.2016.71

Characterisation of natural fibre reinforced PLA foams prepared by supercritical CO_2 assisted extrusion

K. Bocz[1*], *T. Tábi*[2,3], *D. Vadas*[1], *M. Sauceau*[4], *J. Fages*[4], *Gy. Marosi*[1]

[1]Department of Organic Chemistry and Technology, Budapest University of Technology and Economics, Műegyetem rkp. 3., H-1111 Budapest, Hungary
[2]MTA–BME Research Group for Composite Science and Technology, Műegyetem rkp. 3., H-1111 Budapest, Hungary
[3]Department of Polymer Engineering, Budapest University of Technology and Economics, Műegyetem rkp. 3., H-1111 Budapest, Hungary
[4]Centre RAPSODEE, École des Mines d'Albi, CNRS, Université de Toulouse, F-81013 Albi, France

Received 30 January 2016; accepted in revised form 19 April 2016

Abstract. Natural fibre reinforced polylactic acid (PLA) foams, as potential green replacements for petroleum-based polymer foams, were investigated. Highly porous ($\varepsilon > 95\%$) microcellular PLA foams were manufactured by supercritical CO_2 assisted extrusion process. To overcome the inherently low melt strength of PLA, epoxy-functionalized chain extender was applied, while talc was added to improve its crystallization kinetics. The combined application of chain extender and talc effectively promoted the formation of uniform cell structures. The effect of cellulose and basalt fibre reinforcement on the foamability, morphology, structure and mechanical properties of the PLA foams were investigated as well. The addition of 5 wt% natural fibres promoted the cell nucleation, but caused non-uniform distribution of cell size due to the microholes induced by local fibre-matrix debonding. The compression strength of the manufactured basalt fibre reinforced PLA foams reached 40 kPa.

Keywords: *biopolymers, biocomposites, foam extrusion, polylactic acid, natural fibre*

1. Introduction

The replacement of conventional petrol-based and short life-cycle polymer foams with bio-based and biodegradable alternatives will be crucial for the natural environment and to diminish the burden of landfills, still the application of biopolymers as porous materials is negligible up to now.

Recently, poly(lactic acid) (PLA) foams have been considered as the most promising bio-based and biodegradable substitutes for polystyrene (PS) and polyethylene (PE) foam products, which currently hold the majority ratio in the packaging industry. This is mainly due to the competitive material and processing costs of PLA accompanied with comparable barrier and mechanical properties and environmental friendly character [1]. Besides packaging industry, there is a wide range of potential application fields for PLA foams, such as construction and transportation, where these could effectively serve as lightweight heat and sound insulating elements, panels and sandwich composite cores. However, to produce low-density PLA foams with uniform cell morphology, improvements of the inherent shortcomings of PLA, especially its low melt strength and slow crystallization kinetics, need to be addressed.

One of the most investigated methods to improve the melt strength of PLA is the increase of its molecular weight and the modification of its linear molecular structure by using chain extenders (CEs). CEs have two or more functional groups such as hydroxyl, amine, anhydride, epoxy, carboxylic acid or isocyanate. Bifunctional CEs couple the two end groups

*Corresponding author, e-mail: kbocz@mail.bme.hu

of PLA, thereby lead to a linear polymer with somewhat higher molecular weight, while CEs of higher functionality give raise to branched structures with significantly improved rheological properties [2, 3]. It was found by Wang *et al*. [4] that molecular branching increases melt strength and elasticity, and thereby also the integrity of cells, cell density, and expansion ratio during extrusion foaming.

Enhancing crystallization kinetics of PLA during foaming has been recognized as an effective way to overcome its weak viscoelastic properties and to improve its foaming behaviour (i.e. cell nucleation and expansion) [1, 5, 6]. In PLA, improved crystallinity has been achieved by using different nucleation agents, such as talc, that increase the heterogeneous nucleation density [7]. It was shown by Pilla *et al*. [2] that the simultaneous addition of talc and CE leads to increased cell density and more uniform cell structure. Fillers, such as wood particles [8] or clay nanoparticles [9] are also known to act as crystal nucleating agents and change the melt viscosity. Moreover fillers influence the microstructure and thus the mechanical and thermal properties of the foams [10]. Significant crystallinity can also be achieved by using plasticizers that widen the crystallization window by increasing the PLA chain mobility and decreasing the glass transition temperature.

Polymer foams are generally obtained by the addition of chemical blowing agents, their mostly exothermic reaction makes, however, the process and the final cell structure hardly controllable. In addition, they may lead to unwanted residues in the bulk. Physical blowing agents are more desirable from this respect. Currently, the focus is on CO_2 due to its chemical inertness, non-flammability, relative ease of handling, well controllable influence and more favourable interaction with polymers compared to other inert gases. Moreover, it advantageously replaces less ecological solvents like butane, pentane or chlorofluorocarbons (CFCs), which are known for their contribution to the depletion of the ozone layer and may bring hazardous risks. Therefore, the new types of bio-foams are preferably manufactured by CO_2 aided techniques.

Microcellular PLA foams can be manufactured through batch processes, which are, however, hardly scalable from lab-scale due to their small production rate. In the industry more cost-effective continuous processing technologies such as extrusion foaming and foam injection moulding are preferred. Recently, many studies have focused on extrusion foaming using supercritical CO_2 ($scCO_2$) as physical blowing agent [11]. When CO_2 is supercritical, its solubility and diffusivity in PLA increases significantly. The $scCO_2$ introduced into the extruder dissolves in the polymer melt and acts as a plasticizer [12] and by this means affects its crystallization rate [13]. Moreover, lower processing temperatures are applicable and also the mechanical abrasion of the equipment will be reduced. In addition, this may lead to reduced degradation of thermo-labile molecules like active pharmaceutical ingredients which may be used with such process [14]. Compared to the conventional foaming processes, the advantages of the $scCO_2$ aided extrusion foaming are the accurate control of the foam quality (i.e. cell structure), the mild conditions (reduced risk of thermal and hydrolytic degradation), environmental friendliness (organic solvent-free, no residue), the reduced energy demand during processing and the safety.

In this work, natural fibre reinforced PLA foams, as potential green replacements for petroleum-based polymer foams, were investigated. High porosity, microcellular biocomposite foams were manufactured by continuous $scCO_2$ assisted extrusion process. To obtain uniform cell structures with increased cell density, epoxy-functionalized CE and talc were applied. The effect of cellulose and basalt fibre reinforcement was investigated on the morphology and mechanical properties of the PLA foams.

2. Materials and methods

2.1. Materials

Ingeo™ Biopolymer 3052D grade PLA (T_m = 145–160 °C, M_w = 116 000 g/mol, MFR = 14 g/10 min (210 °C, 2.16 kg), D-lactide content = 4%), purchased from NatureWorks LLC (Minnetonka, MN, USA), was the polymer matrix. Its rheology was controlled using a styrene-acrylic oligomer multi-functional epoxide chain extender (CE), Joncryl ADR4368-C with a molecular weight of 6800 g/mol and an epoxy equivalent weight of 285 g/mol, kindly supplied by BASF SE (Lugwigshafen, Germany). As nucleating agent HTPultra5 L type talc (T), received from IMI FABI SpA (Postalesio, Italy), with a median diameter of 0.65 μm was used. The applied reinforcements

included cellulose fibres (Arbocel BWW40, J. Rettenmaier & Söhne GmbH, Rosenberg, Germany) with average fibre length and diameter of 200 and 20 μm, respectively, and basalt fibres (Basaltex KVT 150tex13-I) with linear density of 150 tex, filament diameter of 13 μm and an initial fibre length of 10 mm. CO_2 (Linde AG, Munich, Germany) was applied as physical foaming agent.

2.2. Sample preparation

Before processing, all materials (PLA, natural fibres and additives) were dried at 85 °C for 6 h in all cases. PLA mixtures were prepared by using a Labtech Scientific LTE 26-44 modular twin screw extruder (Labtech Engineering Co., Samutprakarn, Thailand) with a constant screw speed of 20 rpm and the following temperature profile of the extruder zones: $zone_1$ = 175 °C, $zone_2$ = 175 °C, $zone_3$ = 180 °C, $zone_4$ = 180 °C, $zone_5$ = 185 °C, $zone_6$ = 190 °C. The obtained extrudates were pelletized and dried prior to foam extrusion. The composition of the manufactured four types of PLA compounds is summarised in Table 1.

Supercritical-CO_2-aided melt extrusion was performed on a single-screw extruder (Rheoscam, SCAMEX, Crosne, France) with a screw diameter of 30 mm and a length to diameter ratio (L/D) of 37 [15, 16]. As physical foaming agent, CO_2 was injected into the barrel using a syringe pump (260D, ISCO Lincoln, NE, USA). As it is shown in Figure 1, the injection position is located at 20 L/D from hopper, where the screw diameter is constant. CO_2 was introduced at the same pressure as the pressure prevailing in the extruder. The polymer–CO_2 mixture then passed through a static mixer (SMB-H 17/4, Sulzer, Switzerland). This element, inserted before the die, provides a distributive mixing between the two components. A flat die with a width of 30 mm and an adjustable height, which allows tuning the pressure before the die, was used. The temperature inside the barrel was regulated at the following six locations: T_1 and T_2 before and T_3 after the CO_2 injection location, T_4 before the mixing element, T_5 at the static mixer and T_6 at the die. The temperature (T_{mat1}–T_{mat3}) and pressure (P_1–P_4) of the material were measured at three and four sensor locations, respectively.

During foam extrusion experiments, the screw speed was kept constant at 30 rpm and the following temperature profile was set for the extruder zones: T_{hopper} = 50 °C, T_1 = 160 °C, T_2 = 180 °C, T_3 = 180 °C, T_4 = 160 °C, while the mixer (T_5) and die temperatures (T_6) were varied at each experiments while keeping them at a same value. This temperature will be called die temperature in the rest of this article. CO_2 was introduced at a constant volumetric flow rate ranging between 1.5 and 3.0 mL/min. Once $scCO_2$ was injected, a significant decrease in the material pressure within the extruder barrel occurred, mainly due to the

Table 1. Composition of the PLA compounds used for foam extrusion

Sample	PLA [wt%]	Chain extender [wt%]	Talc [wt%]	Cellulose fibre [wt%]	Basalt fibre [wt%]
PLA	100	–	–	–	–
PLA+CE+T	96	2	2	–	–
PLA+CE+T+CF	91	2	2	5	–
PLA+CE+T+BF	91	2	2	–	5

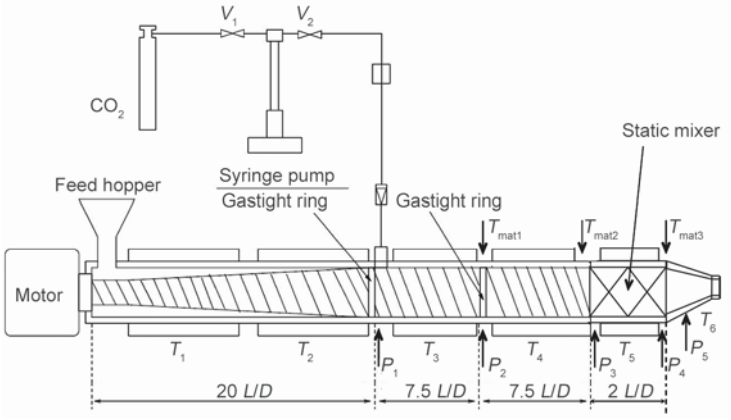

Figure 1. Schematic picture of the foaming system

decrease of melt viscosity. Parallel with the increasing CO_2 concentrations (in the range of 2 to 8 wt%), T_5 and T_6 had been cooled to increase melt strength at the die. Once stable conditions have been established, samples were collected. At each new condition, the temperature (T_{mat3}) and pressure (P_4) of the material, measured just before the entry within the die, were registered. To study the influence of operating parameters on porous structure, several experiments have been carried out varying mixer and die temperatures and CO_2 concentration, by keeping other parameters constant.

2.3. Methods

Rheological measurements

Melt rheology under dynamical shear was investigated using an AR 2000 type rotational rheometer (TA Instruments, New Castle, DE, USA) with 25 mm diameter parallel-plate geometry. Dynamic frequency sweep tests were performed at 170 °C to measure the complex shear viscosity (η*, Pa·s) over a frequency range of 0.1–100 Hz under controlled strain of 1%.

Porosity measurements

Porosity is defined as the ratio of void volume to the total volume of the foam sample. Porosity (ε) of foams was calculated from their apparent density (ρ_{app}) and the density of the non-foamed extrudate (ρ) according to Equation (1):

$$\varepsilon\,[\%] = 100 - \frac{\rho_{app}}{\rho} \cdot 100 \qquad (1)$$

The bulk density (ρ) of the PLA based polymer mixtures were considered to be 1.27 g/cm^3, while ρ_{app} of expanded samples was determined by water-pycnometry.

Scanning electron microscopy (SEM)

Scanning electron microscopic (SEM) images were taken using a JEOL JSM-5500 LV type apparatus (JEOL Ltd., Akishima, Tokyo, Japan) using an accelerating voltage of 15 keV. The samples were coated with gold-palladium alloy before examination to prevent charge build-up on the surface.

Differential scanning calorimetry (DSC)

DSC measurements were carried out using a TA Instruments Q2000 type instrument (New Castle, DE, USA) with a heating rate of 10 °C/min under 50 mL/min nitrogen gas flow, covering a temperature range of 25–180 °C. About 3–6 mg of sample was used in each test.

The percentage crystallinity (χ_c) of PLA foams was calculated according to Equation (2), where ΔH_m is the melting enthalpy, ΔH_{cc} is the cold crystallization enthalpy, ΔH_m^0 is the melting enthalpy of a perfect PLA crystal equal to 93 J/g [16] and φ is the weight fraction of fillers:

$$\chi_c\,[\%] = \frac{\Delta H_m - \Delta H_{cc}}{\Delta H_m^0 \cdot (1-\varphi)} \cdot 100 \qquad (2)$$

Compression strength

An AR2000 Rheometer (TA Instruments, New Castle, DE, USA) with plate-plate adjustment was used for mechanical characterization of cylindrical foam specimens with a diameter of 8 mm. Compression tests were carried out with a constant compression rate of 30 μm/s. The diameter of the squeezing upper plate was 25 mm and the initial gap was 20 mm in all cases. The compressive resistance at 10% relative deformation were determined for each foam samples. At least 5 specimens were tested in all cases.

3. Results and discussion

3.1. Rheological properties

The effect of the used additives, chain extender, talc and fibres on the melt rheology and processability of PLA was studied by dynamic viscosity measurements. As illustrated in Figure 2, the introduction of 2% CE and 2% talc was found to increase the complex viscosity. Likely, not only the CE induced long-

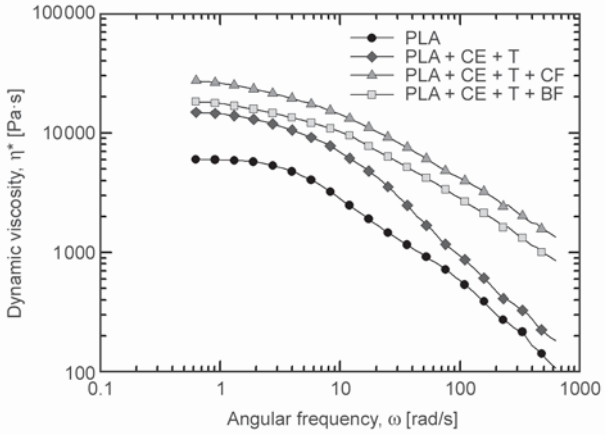

Figure 2. Dynamic viscosity as a function of angular frequency for neat and additive containing PLA

chain branched structure reduced the chain mobility of PLA but also talc enhanced the melt viscosity mainly at the lower shear rate region. The addition of both cellulose and basalt fibres further increased the melt viscosity in the whole frequency range. As the increase of the viscosity mainly depends on the concentration, particle size, particle size distribution and shape of the fillers, the mobility of PLA chain segments were more hindered by the larger number, smaller and less uniform cellulose particles. The decreased chain mobility was expected to improve the melt strength and resistance against CO_2 diffusion, but affect the crystallization kinetics as well.

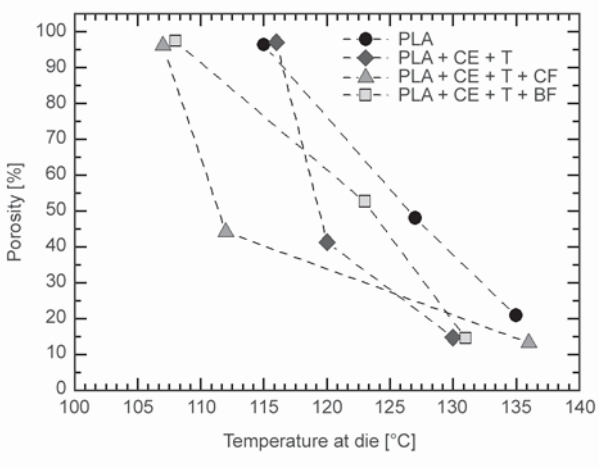

Figure 3. Effect of formulation and mixer and die temperatures on the porosity of PLA foams extruded at 8% of CO_2

3.2. Morphology

Foamed samples from each experiment were compared at three porosity levels, at around 15, 45 and 95%, respectively. Highly porous ($\varepsilon > 95\%$) PLA foam structures were obtained typically at a CO_2 concentration of about 8 wt% and with T_{mat3} of around 110–120 °C, as presented in Figure 3. In all cases, the lower the die temperature, the higher the porosity. This effect is well documented in the literature [7] and is linked with the formation of a skin at the surface of the samples due to lower die temperatures and an optimal melt temperature before the die. This frozen surface prevents CO_2 to escape leading to pore growth and higher expansion ratio. Moreover, in order to prevent cell coalescence and to preserve the high cell density, the polymer melt should be cooled substantially to increase its strength to preserve the high cell density, while keeping a sufficient fluidity for bubbles to grow. The effect of CO_2 content is also linked with temperature since the CO_2 solubilisation is inversely proportional to temperature. High CO_2 content can only be obtained at low temperatures.

It was observed that a wider processing window is available for PLA foam formation by using natural fibres. Compared to neat PLA, in the case of the additive containing mixtures less porous foams were obtained at all die temperatures, indicating more gas loss when CE, talc and fibre are present in the polymer melts. As a function of decreasing temperatures, a sharp increase in the porosity of the CE and talc containing PLA foam (PLA+CE+T) is observable, which is associated with its accelerated solidification with crystallization at low temperature. Similar behaviour was observed for the cellulose containing mixture, indicating enhanced nucleation effect of the dispersed cellulose fibres.

SEM micrographs taken from the highly expanded ($\varepsilon > 95\%$) foams are presented in Figure 4. It can be seen that broad cell size distribution accompanied with rather limp or collapsed cell walls are characteristic for the neat PLA foam (Figure 4a). It is assumed that due to the early homogeneous nucleation the cells have longer time for growth [17]. Nevertheless, due to the insufficient melt strength of PLA at the foaming temperature, the cell walls have only low resistance against CO_2 diffusion from the melt to the atmosphere, and thus limp and mechanically weak cell structure is formed. In contrast, the PLA foam containing CE and talc (PLA+CE+T) had a denser and more uniform cell morphology (Figure 4b), indicating that the addition of CE effectively increased the melt strength. Based on the lower temperature profile, allowed in the case of the fibre reinforced foams, a greater degree of crystallinity and improved melt strength were expected. It can be seen on Figure 4c and d that the addition of natural fibres resulted in decreased cell diameters likely due to the increased melt viscosity (see Figure 2) and due to the increased number of nucleating sites induced by the fibre surfaces [18, 19]. At the same time, the fibre reinforced foams have less uniform cell structure, which should be related to the fibre distribution within the polymer matrix and the fibre matrix interactions [19]. It is suggested that as a result of local fibre-matrix debonding microholes are induced, where the gas loss hinders the cell growing ability, and thus non-uniform

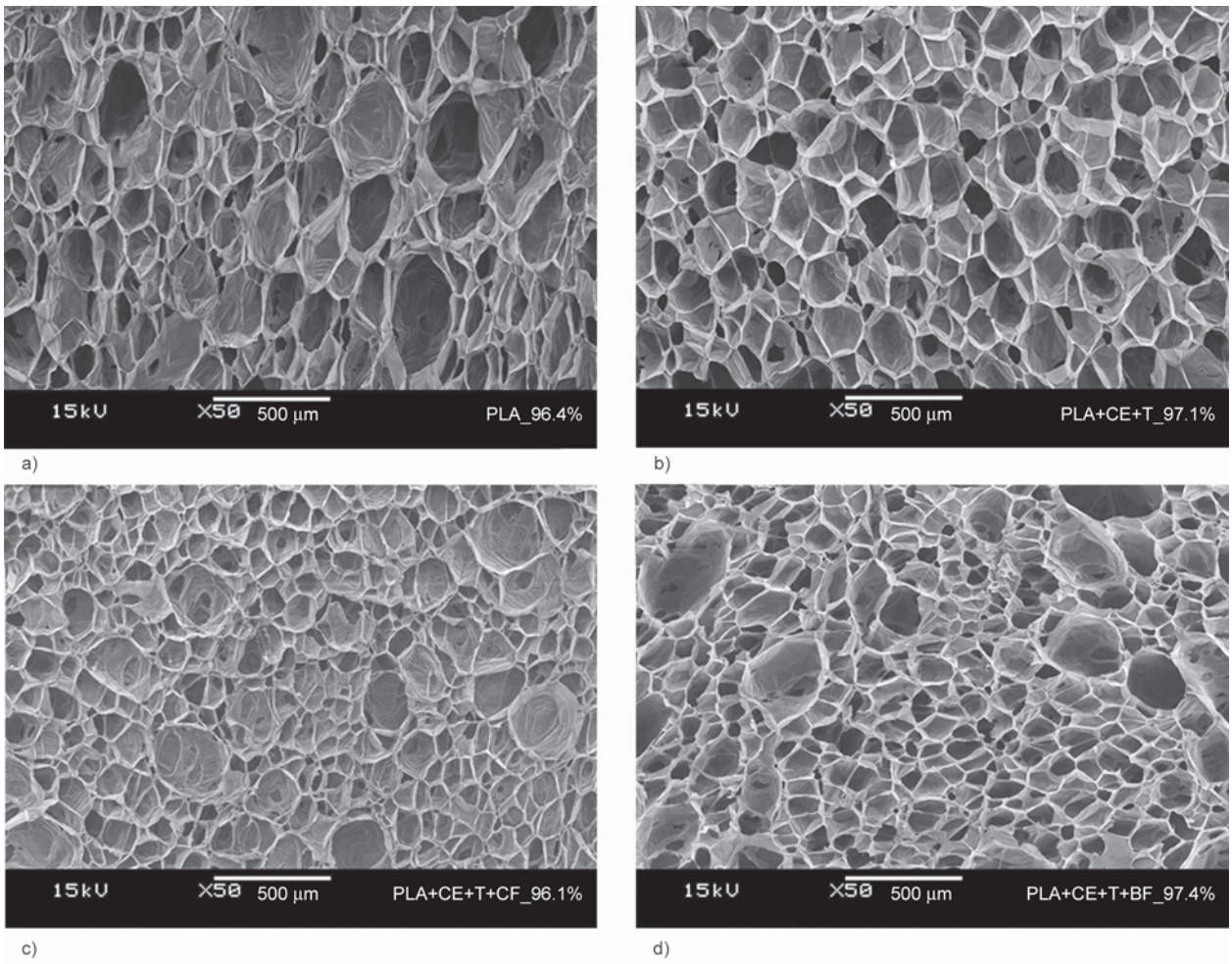

Figure 4. SEM micrographs of the cell morphologies obtained for highly expanded (ε > 95%) PLA foams. PLA (a), PLA+CE+T (b), PLA+CE+T+CF (c), PLA+CE+T+BF (d). The actual porosity values are represented after the abbreviation of the materials within every micrograph.

distribution of cell size is obtained. Also, an increase in the open-cell ratio in the presence of fibres compared to unreinforced PLA foams was expected based on the results of previous studies [20].

3.3. Crystallinity

The crystallinity of the PLA foams was examined by DSC method. The first heating runs of the neat PLA foams at three porosity levels are presented in Figure 5. It can be observed that the low porosity PLA foams are almost fully amorphous, which is indicated by the sharp glass transition around 60 °C and by the broad exothermic peak in the range of 100 and 120 °C indicating significant cold-crystallisation [21]. The melting of the crystalline phase occurs around 150 °C. Typically two endothermic peaks are visible, at 149 °C corresponding to melting of the less ordered α' crystals, and at 156 °C corresponding to melting of the thermodynamically more stable α

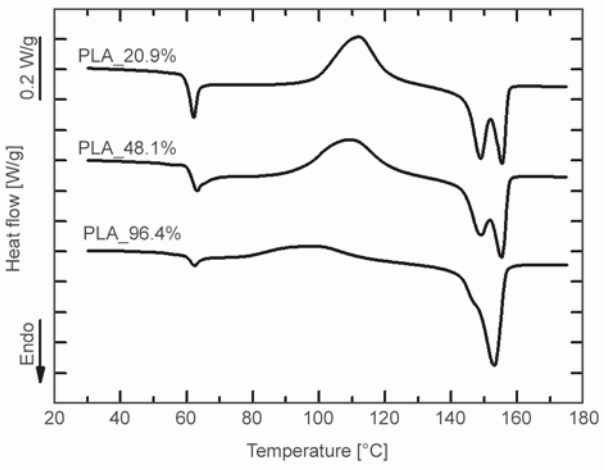

Figure 5. DSC curves of PLA foams of increasing porosity. The actual porosity values are represented after the abbreviation of the materials within the graph.

crystals [22]. In contrast, only a slight cold-crystallization exotherm is observable in the DSC curve of the PLA foam of 96.4% porosity, indicating notice-

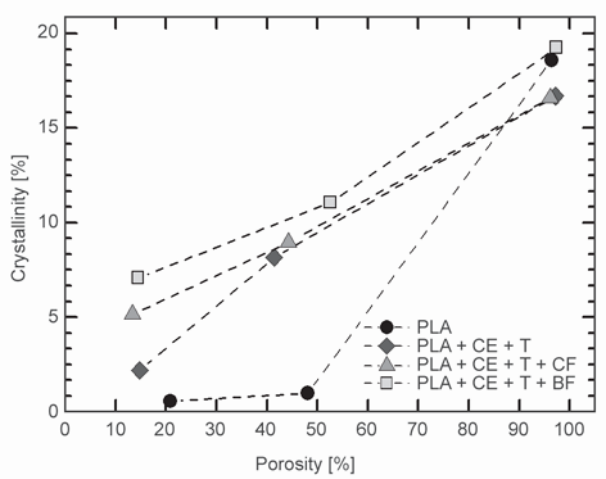

Figure 6. Foam crystallinity as a function of porosity

able inherent crystalline phase in this sample. Based on the dominance of the ordered α crystal form in the highly expanded PLA foam, it can be concluded that its crystallization occurred mainly during processing. Similar trends were observed for the other examined, additive containing PLA foams.

Figure 6 presents the estimated crystallinity versus porosity for the neat and additive containing PLA foams. It can be seen that for the foam samples containing additives the degree of crystallinity increased almost linearly with porosity. It is likely due to the strain-induced crystallization [9, 23] and to the plasticizing effect of CO_2 which results in the decrease of the temperature of crystallization and formation of more perfect crystalline domains.

The advantageous effect of the used nucleating agents (talc, cellulose and basalt fibre) on the crystallinity is most observable at lower expansion ratios. Accordingly, both natural fibres promoted the nucleation effectively, but the highest degree of crystallinity values were obtained for the basalt fibre reinforced PLA foams. In the case of cellulose fibre reinforcement, it is supposed that the increased dynamic viscosity (Figure 2) and thus the hindrance of molecular chain mobility decreased the crystallization. The high degree of crystallinity is, however, crucial to obtain improved thermo-mechanical properties [24, 25]. The prominent nucleating ability of basalt fibres has been utilized recently by Tábi *et al*. [26] to obtain crystalline PLA composites of high heat deflection temperatures.

3.4. Compression strength

The mechanical performance of the PLA foams, manufactured in this work, has been evaluated based on their compression strength at 10% deformation. The compression strength of the obtained neat and additive containing highly expanded ($\varepsilon > 95\%$) PLA foams are indicated in Figure 7. It is clearly visible that without additives the neat PLA foam has low compression strength, about 20 kPa. This is expected based on the collapsed cell structure, also observed in Figure 4a, formed as a consequence of the insufficient melt strength. In contrast, the addition of CE and talc promoted the formation of uniform cell-structure, the mechanical resistance of which reaches 100 kPa. The compression strength of the talc and CE containing PLA foam deteriorated when 5 wt% natural fibres were added. This can be explained by the poor adhesion, the lower polydispersity and the increased open-cell ratio evidenced by SEM micrographs (Figure 4c and d). Another argument can be that cellulose and basalt fibres are too large compared with the cell size to provide efficient reinforcement. Nevertheless, the compression strength of the basalt fibre reinforced PLA foam reaches 40 kPa.

4. Conclusions

Natural fibre reinforced microcellular PLA composite foams were manufactured by $scCO_2$ assisted foam extrusion process, the same method that could be easily scaled-up even towards real industrial applications. Epoxy functionalized CE and talc were used to improve the foamability of PLA. It was found that the addition of 5 wt% cellulose or basalt fibres pro-

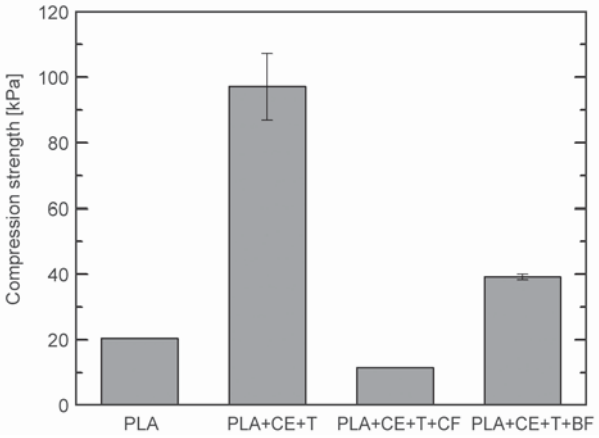

Figure 7. Compression strength of PLA foams

vides a wider processing window for PLA foam production. Based on the lower applicable temperature profile, a greater degree of crystallinity and improved melt strength could be expected. It was evinced that natural fibres increase the melt viscosity and promote the heterogeneous cell nucleation. As a result, microcellular composite foam structures with porosity higher than 95% could be obtained. However, due to the fibre distribution and the weak fibre matrix adhesion, the fibre reinforced foams have less uniform cell structure and increased open cell ratio compared to the unreinforced CE and talc containing foam. Basalt fibres can serve as reinforcement providing improved compression strength comparing to PLA foams. However, the best mechanical performance was achieved without reinforcing fibres, by applying only the combination of CE and talc. The compression strength of this foam reaches 100 kPa. It is believed that further chemical or physical modifications, such as reinforcement and flame retardancy, could promote the market penetration of PLA foams in technical application fields as well.

Acknowledgements

This work was financially supported by the Hungarian Scientific Research Fund (grant numbers OTKA K112644 and K105257). This paper was supported by the János Bolyai Research Scholarship of the Hungarian Academy of Sciences and by the Italian-Hungarian and the Mexican-Hungarian bilateral agreement of the Hungarian Academy of Sciences. This work is connected to the scientific program of the 'Development of quality-oriented and harmonized R+D+I strategy and functional model at BME' project. This project is supported by the New Széchenyi Development Plan (Project ID: TÁMOP-4.2.1/B-09/1/KMR-2010-0002).

References

[1] Nofar M., Park C. B.: Poly (lactic acid) foaming. Progress in Polymer Science, **39**, 1721–1741 (2014). DOI: 10.1016/j.progpolymsci.2014.04.001

[2] Pilla S., Kim S. G., Auer G. K., Gong S., Park C. B.: Microcellular extrusion-foaming of polylactide with chain-extender. Polymer Engineering and Science, **49**, 1653–1660 (2009). DOI: 10.1002/pen.21385

[3] Najafi N., Heuzey M. C., Carreau P. J., Wood-Adams P. M.: Control of thermal degradation of polylactide (PLA)-clay nanocomposites using chain extenders. Polymer Degradation and Stability, **97**, 554–565 (2012). DOI: 10.1016/j.polymdegradstab.2012.01.016

[4] Wang J., Zhu W., Zhang H., Park C. B.: Continuous processing of low-density, microcellular poly(lactic acid) foams with controlled cell morphology and crystallinity. Chemical Engineering Science, **75**, 390–399 (2012). DOI: 10.1016/j.ces.2012.02.051

[5] Nofar M., Ameli A., Park C. B.: A novel technology to manufacture biodegradable polylactide bead foam products. Materials and Design, **83**, 413–421 (2015). DOI: 10.1016/j.matdes.2015.06.052

[6] Nofar M., Ameli A., Park C. B.: Development of polylactide bead foams with double crystal melting peaks. Polymer, **69**, 83–94 (2015). DOI: 10.1016/j.polymer.2015.05.048

[7] Mihai M., Huneault M. A., Favis B. D.: Crystallinity development in cellular poly(lactic acid) in the presence of supercritical carbon dioxide. Journal of Applied Polymer Science, **113**, 2920–2932 (2009). DOI: 10.1002/app.30338

[8] Rachtanapun P., Selke S. E. M., Matuana L. M.: Microcellular foam of polymer blends of HDPE/PP and their composites with wood fiber. Journal of Applied Polymer Science, **88**, 2842–2850 (2003). DOI: 10.1002/app.12170

[9] Keshtkar M., Nofar M., Park C. B., Carreau P. J.: Extruded PLA/clay nanocomposite foams blown with supercritical CO_2. Polymer, **55**, 4077–4090 (2014). DOI: 10.1016/j.polymer.2014.06.059

[10] Di Y., Iannace S., Di Maio E., Nicolais L.: Poly(lactic acid)/organoclay nanocomposites: Thermal, rheological properties and foam processing. Journal of Polymer Science Part B: Polymer Physics, **43**, 689–698 (2005). DOI: 10.1002/polb.20366

[11] Sauceau M., Fages J., Common A., Nikitine C., Rodier E.: New challenges in polymer foaming: A review of extrusion processes assisted by supercritical carbon dioxide. Progress in Polymer Science, **36**, 749–766 (2011). DOI: 10.1016/j.progpolymsci.2010.12.004

[12] Ladin D., Park C. B., Park S. S., Naguib H. E., Cha S. W.: Study of shear and extensional viscosities of biodegradable PBS/CO_2 solutions. Journal of Cellular Plastics, **37**, 109–148 (2001) DOI: 10.1106/72D3-9PX6-7C60-RD2X

[13] Takada M., Hasegawa S., Ohshima M.: Crystallization kinetics of poly(L-lactide) in contact with pressurized CO_2. Polymer Engineering and Science, **44**, 186–196 (2004). DOI: 10.1002/pen.20017

[14] Vigh T., Sauceau M., Fages J., Rodier E., Wagner I., Sóti P. L., Marosi G., Nagy Z. K.: Effect of supercritical CO_2 plasticization on the degradation and residual crystallinity of melt-extruded spironolactone. Polymers for Advanced Technologies, **25**, 1135–1144 (2014). DOI: 10.1002/pat.3367

[15] Le Moigne N., Sauceau M., Benhyakhlef M., Jemai R., Benezet J-C., Rodier E., Lopez-Cuesta J. M., Fages J.: Foaming of poly(3-hydroxybutyrate-*co*-3-hydroxyvalerate)/organo-clays nano-biocomposites by a continuous supercritical CO_2 assisted extrusion process. European Polymer Journal, **61**, 157–171 (2014).
DOI: 10.1016/j.eurpolymj.2014.10.008

[16] Fischer E. W., Sterzel H. J., Wegner G.: Investigation of the structure of solution grown crystals of lactide copolymers by means of chemical reactions. Colloid and Polymer Science, **251**, 980–990 (1973).
DOI: 10.1007/BF01498927

[17] Matuana L. M., Diaz C. A.: Study of cell nucleation in microcellular poly(lactic acid) foamed with supercritical CO_2 through a continuous-extrusion process. Industrial and Engineering Chemistry Research, **49**, 2186–2193 (2010).
DOI: 10.1021/ie9011694

[18] Matuana L. M., Faruk O.: Effect of gas saturation conditions on the expansion ratio of microcellular poly(lactic acid)/wood-flour composites. Express Polymer Letters, **4**, 621–631 (2010).
DOI: 10.3144/expresspolymlett.2010.77

[19] Bergeret A., Benezet J. C.: Natural fibre-reinforced biofoams. International Journal of Polymer Science, **2011**, 569871/1–569871/14 (2011).
DOI: 10.1155/2011/569871

[20] Li Q., Matuana L. M.: Foam extrusion of high density polyethylene/wood-flour composites using chemical foaming agents. Journal of Applied Polymer Science, **88**, 3139–3150 (2003).
DOI: 10.1002/app.12003

[21] Tábi T., Sajó I. E., Szabó F., Luyt A. S., Kovács J. G.: Crystalline structure of annealed polylactic acid and its relation to processing. Express Polymer Letters, **4**, 659–668 (2010).
DOI: 10.3144/expresspolymlett.2010.80

[22] Le Marec P. E., Ferry L., Quantin J-C., Bénézet J-C., Bonfils F., Guilbert S., Bergeret A.: Influence of melt processing conditions on poly(lactic acid) degradation: Molar mass distribution and crystallization. Polymer Degradation and Stability, **110**, 353–363 (2014).
DOI: 10.1016/j.polymdegradstab.2014.10.003

[23] Garancher J-P., Fernyhough A.: Expansion and dimensional stability of semi-crystalline polylactic acid foams. Polymer Degradation and Stability, **100**, 21–28 (2014).
DOI: 10.1016/j.polymdegradstab.2013.12.037

[24] Battegazzore D., Bocchini S., Frache A.: Crystallization kinetics of poly(lactic acid)-talc composites. Express Polymer Letters, **5**, 849–858 (2011).
DOI: 10.3144/expresspolymlett.2011.84

[25] Petchsuk A., Buchatip S., Supmak W., Opaprakasit M., Opaprakasit P.: Preparation and properties of multi-branched poly(D-lactide) derived from polyglycidol and its stereocomplex blends. Express Polymer Letters, **8**, 779–789 (2014).
DOI: 10.3144/expresspolymlett.2014.80

[26] Tábi T., Tamás P., Kovács J. G.: Chopped basalt fibres: A new perspective in reinforcing poly(lactic acid) to produce injection moulded engineering composites from renewable and natural resources. Express Polymer Letters, **7**, 107–119 (213).
DOI: 10.3144/expresspolymlett.2013.11

eXPRESS Polymer Letters Vol.10, No.9 (2016) 780–787
Available online at www.expresspolymlett.com
DOI: 10.3144/expresspolymlett.2016.72

Solvothermal synthesis of a polyaniline nanocomposite – a prospective biosensor electrode material

R. K. Agrawalla[1,2], V. Meriga[2], R. Paul[1,3], A. K. Chakraborty[2], A. K. Mitra[1,4]*

[1]Nanoscience Laboratory, Department of Physics, National Institute of Technology Durgapur, M. G. Avenue, 713209 Durgapur, India
[2]Carbon Nanotechnology Laboratory, Department of Physics, National Institute of Technology Durgapur, M.G. Avenue, 713209 Durgapur, India
[3]Presently D S Kothari Postdoctoral Fellow, Materials Engineering Department, Indian Institute of Science, 560012 Bangalore, India
[4]Presently Visiting Professor, National Institute of Technology, 713209 Durgapur, India

Received 14 February 2016; accepted in revised form 1 May 2016

Abstract. Polyaniline (PANI) is the most important conducting polymer with excellent electrochemical properties. So PANI-based biosensors may find wide applications in medical diagnostics. We report here a ternary nanocomposite of gold nanoparticle- decorated single- walled carbon nanotubes (SWCNTs) embedded in sulfonated polyaniline matrix, prepared using a simple solvothermal chemical route. The structural and morphological characteristics have been determined by electron microscopy, X-ray diffraction and Raman spectroscopy. Optical characteristics of the nanocomposite have been determined by ultraviolet (UV)-visible absorption spectroscopy and photoluminescence spectroscopy. The direct current (DC)-conductivity measurement of the material shows a significant increase in electrical conductivity at 353 K from $7.80 \cdot 10^{-2}$ S/m for pure SPANI to 10.91 S/m for the 3-phase nanocomposite as synthesized in the present investigations. Thus the incorporation of SWCNT/Au nanohybrid fibers in the PANI matrix enhanced its electrical properties. Sulfonation increased the processability of the material, as the samples have now been found to be soluble in water and common organic solvents like DMSO. Such a functional nanocomposite will make an excellent biosensor electrode material.

Keywords: *nanocomposites, SWCNT/Au fibers, sulfonated polyaniline, biosensor*

1. Introduction

Biosensors make a very important area of intensive investigation for their wide applications in medical diagnostics and other useful fields. Polyaniline (PANI) is an interesting polymer due to its conducting properties, relatively cheap price and good stability and hence is one of the most studied conducting polymers in recent years [1–3]. Moreover as polyaniline (PANI) has excellent electrochemical properties, it is an automatic choice in the design of sensor electrode materials.

Carbon nanotubes (CNTs) have attracted great research interest due to their many interesting properties leading to numerous potential applications [4]. In particular, functionalized SWCNTs, due to active functional groups on their surfaces are suitable for even wider range of applications such as in sensors, polymer composites etc. [5–7]. Consequently, researchers have combined functionalized CNTs with PANI [8, 9] and evaluated their properties. However, as PANI is insoluble in water and common organic solvents, in order to improve its processability, researchers often carry out sulfonation in which sul-

*Corresponding author, e-mail: akmrecdgp@yahoo.com

fonic acid functional groups are attached to PANI and the product thus formed is a soluble polymer called sulfonated polyaniline (SPANI) as pointed out in their work by some investigators [10, 11].

One problem in this approach is that the electrical conductivity is greatly reduced by sulfonation which puts some limitation on the use of the polymer. Owing to their excellent electrical properties, it is expected that incorporating CNTs and in particular, metal nanoparticle-decorated CNTs, into SPANI matrix may result in composites having enhanced electrical properties due to synergetic influence, without compromising much the electrochemical properties of the polymer. Noble metal nanoparticles such as gold, silver etc. are special choice for decorating CNTs, in the design of biosensors, due to their high chemical stability and excellent electrical conductivity. Gold is particularly important because of its known affinity towards attachment with biomolecules, which is important for its application in biosensors.

However, in spite of the interest, till todate only few reports have been published on this topic. The earliest report is the one by Santhosh *et al*. [12] who prepared electrocatalysts by dispersing gold nanoparticles into a PANI grafted multi-walled carbon nanotube (MWCNT) matrix which can have application in direct methanol fuel cells. The PANI/gold (Au) composite hollow spheres were synthesized by Feng *et al*. [13], which showed more than three times higher electrical conductivity than that of pure PANI hollow spheres. The composite further showed enhanced electrocatalytic activity for the oxidation of dopamine when immobilized onto a carbon electrode. Wang *et al.* [14] synthesized PANI/MWCNT/Au composite film via a two-step electrochemical process, with Au nanoparticles dispersed in the PANI-MWCNT film. The composite exhibited good electrochemical and electrocatalytic activity. Chang *et al*. [15] fabricated PANI/Au/MWCNT nanocomposite by one pot synthesis when aniline molecules were adsorbed and polymerized on the surfaces of MWCNTs. The composite showed superior sensitivity in ammonia gas detection. Lee *et al*. [16] prepared composites of single-walled carbon nanotubes (SWCNTs), PANI and Au nanoparticles in an in-situ one-pot fashion, by using γ-radiation as source for initiation of polymerization and generation of Au nanoparticles. Guo and Peng [17] synthesized SWCNT/PANI/Au composite by using aromatic amine chemistry, and found the material to be a good electrode material for use in electrochemical sensors. Rima and Mitra [18] prepared and studied the optical and electrical properties of SWCNT/Au nanohybrids, and suggested that the composite could be used as efficient catalyst in chemical industry, as well as in medical diagnostics. What we have observed is that these studies have mostly used PANI rather than SPANI and hence the synthesized material has very little processability. So the ternary composites containing SWCNT, SPANI and gold nanoparticles deserve greater research attention, and would lead to a better biosensor electrode coating material.

In an effort to understand the influence of gold nanoparticles on SWCNT/SPANI composites, we present a simple chemical synthesis of a composite containing sulfonated polyaniline (SPANI) and SWCNT/Au hybrid nanostructures. The gold nanoparticle- decorated SWCNTs (SWCNT/Au nanohybrid) were prepared by a simple wet chemical process. The morphology and structural properties of the nanocomposites thus produced were characterized by a number of analytical techniques including X-ray diffraction (XRD), scanning electron microscopy (SEM), high resolution transmission electron microscopy (HRTEM), Raman spectroscopy etc. Optical properties of the nanocomposites were evaluated by UV-visible absorption spectroscopy and photoluminescence (PL) spectroscopy. Further, the electrical properties were studied through DC-conductivity measurement.

2. Materials and methods

2.1. Materials

The SWCNTs used in this work were supplied by Chengdu Organic Chemicals Co. Ltd, P. R. China, prepared by electric arc discharge method. The average diameter, length and purity of the SWCNTs, as stated by the manufacturer were 1–2 nm, 1–3 μm, and 95 wt%, respectively. Aniline, 1,2-dichloroethane (DCE) and ammonium persulfate were supplied by Merck Specialties Pvt. Ltd., Mumbai, India. The chlorosulfonic acid and trisodium citrate used in our work were supplied by LOBA Chemie Pvt. Ltd., Mumbai, India. Except SWCNTs, all other chemicals were used as received without further purification.

2.2. Purification and functionalization of SWCNTs

The as-received SWCNTs were purified following methods reported elsewhere [11]. In brief the purification involved heating in a muffle furnace at 350 °C in air for 1 h followed by soaking and stirring in 6 M HCl for 12 h. The acid-treated SWCNTs were filtered and washed thoroughly with deionized water after which further treated in a mixture of concentrated HNO_3/H_2SO_4 in 1:3 volume proportion for 4 h followed by washing with dilute NaOH aqueous solution and filtration until the pH became neutral. The product thus obtained was SWCNTs functionalized with carboxylic (–COOH) acid groups (f-SWCNTs).

2.3. Synthesis of SWCNT/Au nanohybrid

Tetrachloroauric acid (0.0142 g) was added to deionized water (50 mL) and stirred at 100 °C for 30 min. In another beaker, trisodium citrate solution (reducing agent) was prepared by mixing it with de-ionized water and stirred at 100 °C for 30 min. SWCNTs (0.0612 g) was then added to the solution containing tetrachloroauric acid and simulataneously the citrate solution was also added into it followed by stirring at 80 °C for further 30 min. The resultant mixture was then filtered using vacuum filtration system (Millipore membrane, pore size ~ 0.22 μm). The precipitate was then washed with deionized water and filtered again to obtain SWCNT/Au nanohybrid fibres. The sample was then dried under an infrared (IR) lamp.

2.4. Synthesis of SPANI and SPANI/SWCNT composite

The detailed method for the synthesis of sulfonated polyaniline (SPANI) has been reported elsewhere by our group [11]. In brief, this involved the use of aniline hydrochloride, ammonium persulfate and chlorosulfonic acid as precursors. SPANI/SWCNT composite containing 6 wt.% SWCNT (as estimated from TGA) was prepared by dissolving SPANI and SWCNT in water followed by filtration.

2.5. Synthesis of SPANI/SWCNT/Au ternary composite

SWCNT/Au nanohybrid (0.03 g) was added into deionized water followed by addition of SPANI aqueous solution and stirred for 3 hrs at 60 °C. The SPANI/SWCNT/Au composite was obtained by filtering the solution and drying the filtrate.

2.6. Characterization methods

The high resolution micrographs were recorded using a (Carl Zeiss) field emission scanning electron microscope (FESEM), and a high resolution transmission electron microscope (HRTEM) JEM-2010 (JEOL Japan) with operating acceleration voltage of 200 kV. Raman spectroscopy was performed using EZ Raman–M field portable Raman analyzer (Enwave Optronics Inc., USA), using a diode laser of wavelength 785 nm as excitation source. The thermogravimetric analysis (TGA) was carried out with Perkin Elmer Pyris-1 TGA thermogravimetric analyzer (USA) at a heating rate of 10 °C/min in nitrogen atmosphere. The optical absorbance spectra were recorded using a U-3010 UV-visible absorption spectrophotometer (HITACHI, JAPAN). Photoluminescence spectra of the samples were acquired using a PerkinElmer LS-55 Fluorescence Spectrophotometer (USA). The electrical conductivity of the samples was measured in ambient atmosphere by a Four-Probe set-up (DFP-02, Scientific Equipment, India).

3. Results and discussion

The morphology of SPANI/f-SWCNT/Au composite was investigated by electron microscopy. The FESEM micrographs of the sample are shown in Figure 1a, in which we observe gold nanoparticles attached to the surfaces of nanotube bundles. The presence of gold is confirmed in the energy dispersive analysis by X-ray spectroscopy (EDAX) spectrum shown in Figure 1b. The presence of carbon comes from both f-SWCNT and SPANI. The morphology shows tubular structure of carbon nanotube bundles with attached gold nanoparticle clusters on its surfaces, and covered by polyailine matrix. Such structures have been observed by earlier investigators [19].

In the HRTEM image (Figure 2), we observe the presence of CNT bundle coated with SPANI and decorated with gold nanoparticles. The average diameter of tubular structure is measured to be about ~12 nm from the HRTEM micrograph. The dark spots represent the gold nanoparticles with particle size in the range of 2 to 7 nm.

The X-ray diffractograms of SPANI, f-SWCNT, SPANI/f-SWCNT binary composite (6 wt%) and

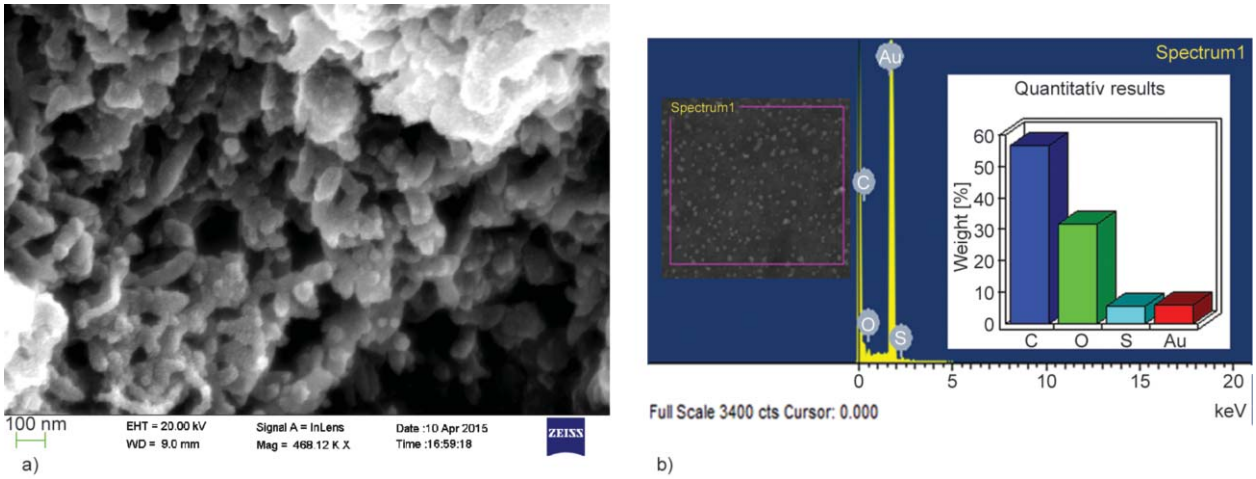

Figure 1. (a). FESEM image of SPANI/f-SWCNT/Au ternary nanocomposite, (b) EDAX analysis of SPANI/f-SWCNT/Au ternary composite showing SEM picture in the left, spectrum in the middle and the quantity of elements in the right

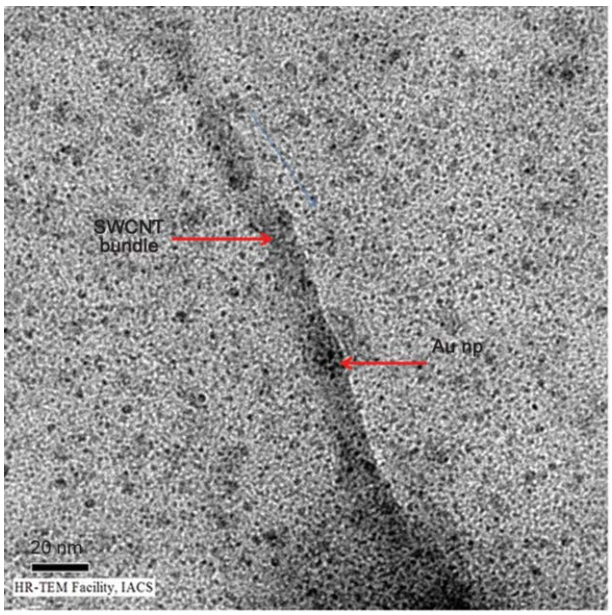

Figure 2. HRTEM micrograph of SPANI/f-SWCNT/Au ternary composite

SPANI/f-SWCNT/Au ternary composite are compared in Figure 3. The features observed for SPANI and SWCNT (JCPDS card no. 75-1621) are in good agreement with the reported literature. The magnified diffractogram of the ternary composite is separately plotted in Figure 4, for better clarity in which the characteristic peaks of CNT and gold are clearly visible. The sharp peaks at 37.8, 43.7 and 64° are assigned to (111), (200) and (220) planes of the reflections of face-centered cubic (fcc) structure of metallic Au nanocrystals (JCPDS card no. 00-004-0784). The average size of Au nanoparticles in the composite is calculated to be ~8 nm using the *Debye-Scherrer formula*. The general features of the diffractogram of SPANI are retained in the composite, but the crystallinity of Au and SWCNT manifest in the SPANI background.

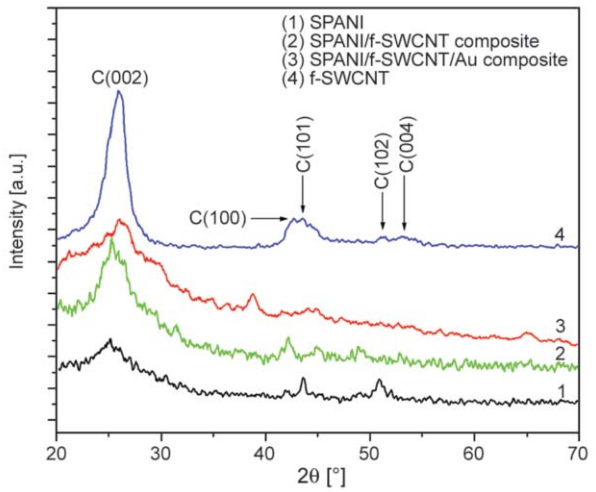

Figure 3. XRD patterns of SPANI, f-SWCNT, SPANI/f-SWCNT and SPANI/f-SWCNT/Au

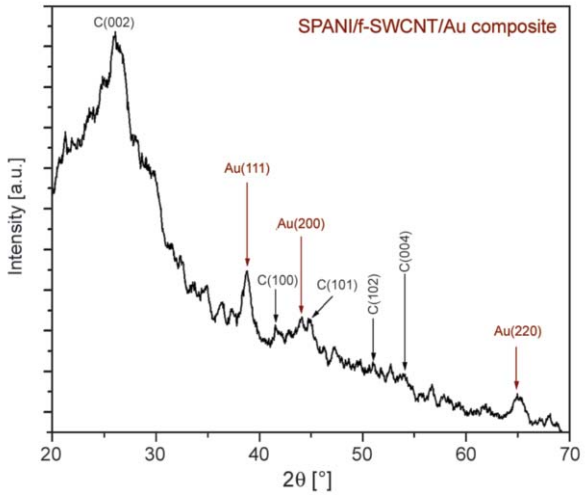

Figure 4. Magnified XRD pattern of SPANI/f-SWCNT/Au ternary composite

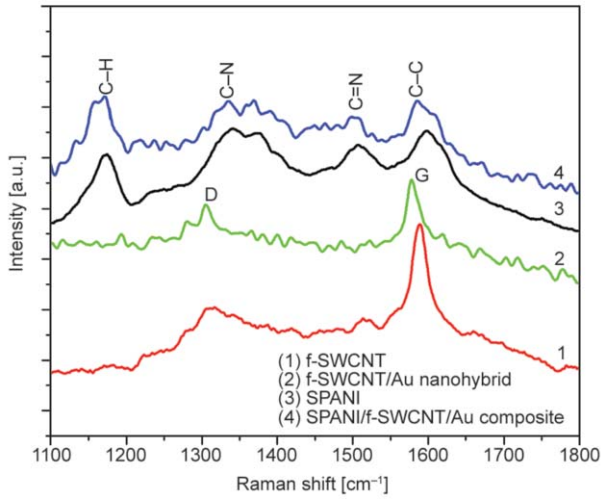

Figure 5. Raman spectra of SPANI, f-SWCNT, f-SWCNT/Au hybrid and SPANI/f-SWCNT/Au ternary composite

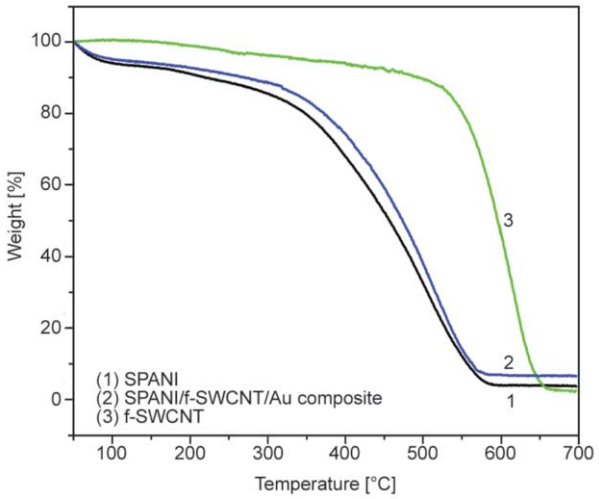

Figure 6. Thermograms of SPANI, f-SWCNT, and SPANI/f-SWCNT/Au ternary composite

Figure 5 shows the Raman spectra of SPANI, f-SWCNT, f-SWCNT/Au nanohybrid and SPANI/f-SWCNT/Au ternary composite. The spectra of f-SWCNT (curve 1) and f-SWCNT/Au hybrid (curve 2) show peaks assigned to both G-band and D-bands of SWCNT. The position of the G-band of SWCNT is red-shifted from 1589 to 1577 cm on decorating with Au nanoparticles, indicating charge transfer between SWCNT bundles and Au nanoparticles [20, 21]. Further, the ratio of the intensity of these two peaks (I /I) increases from 0.51 to 0.79 on attaching gold nanoparticles on the SWCNT surfaces indicating an increased disorder and lowering of symmetry as expected. In the ternary composite (curve 4), the features are dominated by those of SPANI possibly due to thick coating of SWCNT/Au nanohybrids with SPANI polymer.

Figure 6 shows the TGA thermograms of f-SWCNT, SPANI and SPANI/f-SWCNT/Au composite. The thermogram of the ternary composite is similar to that of SPANI, which is due to very low nanohybrid content. While f-SWCNTs do not show any noticeable loss of mass until about 550 °C, the SPANI and its composites show almost complete weight loss at a temperature of 580 °C. This is not surprising given SPANI being a relatively soft polymer and that the ternary sample has very low CNT content. The interesting thing to observe here is that for SPANI/f-SWCNT/Au composite, some residual weight (of about 7%) is observed even at temperatures above 700 °C. This is due to the undecomposed gold metal present in the nanocomposite, although the residual weight for pure SPANI is less than 4%. Moreover SPANI may also have undergone some incomplete decomposition, as has been observed in some earlier investigations.

For optical spectroscopy, the samples were dissolved in an organic solvent dimethyl sulfoxide (DMSO) which is a good solvent for both SPANI and its SWCNT-based composites.

The UV-visible absorption spectra of different samples are compared in Figure 7. The spectrum of SPANI consists of humps at 355 nm (π-π^* transition), 455 nm (polaron-π^* transition) and beyond 750 nm (π-polaron transition). The different absorbance bands for SPANI/f-SWCNT binary composite are clearly evident. In the spectrum of SPANI/f-SWCNT/Au nanocomposite, there is a shift of the π-π^* transition to

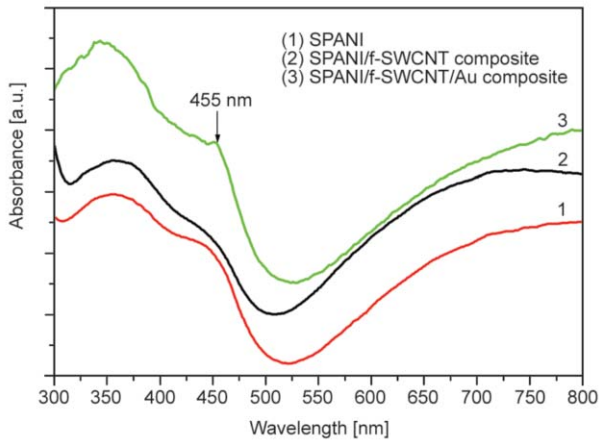

Figure 7. UV-vis absorbance spectra of SPANI, SPANI/f-SWCNT binary composite and SPANI/f-SWCNT/Au ternary composite

340 nm. We also observe a shoulder peak at about 455 nm, which may correspond to the modified SPR band of gold nanoparticles. The SPR band for gold nanoparticles is generally observed at about 520 nm which might have changed its position with reduced intensity. As SPANI provides a different dielectric medium to Au nanoparticles and as the SPR band is sensitive to its environment, shifting and quenching effects take place. There is a possibility of merging of the strong SPR band with the polaron band of SPANI, which is also observed in this region. Similar observations have been reported earlier [16].

The optical band gaps of the investigated samples are estimated using *Tauc relation* [22]. The optical band gap of pure SPANI is estimated to be 3.75 eV. For the samples of SPANI/f-SWCNT and SPANI/f-SWCNT/Au composites, it is estimated to be 3.66 and 3.41 eV respectively, as shown in Figure 8. The decrease in band gap with incorporation of SWCNT and SWCNT/Au hybrid is compatible with their better electrical conductivities [23].

The PL spectra for the different samples are obtained for an excitation wavelength of 300 nm and are shown in Figure 9. SPANI shows a hump around 445 nm. There is a quenching effect of the broad emission band of SPANI upon interactions with CNT/Au nanohybrid, which generally takes place when the polymer is doped to a highly conductive state [24].

Figure 10 shows the dc electrical conductivity of SPANI, SPANI/f-SWCNT binary composite and SPANI/f-SWCNT/Au ternary composite at temperatures ranging from 313 to 353 K. We observe an increase in the conductivity with increase in temperature for all these samples, thus showing semiconductor like behavior. On adding the nanotubes or the nanohybrids to the polymer, the conductivity increases. At 353 K, the conductivity values for SPANI, SPANI/f-SWCNT and SPANI/f-SWCNT/Au samples are $7.80 \cdot 10^{-2}$, $5.58 \cdot 10^{-1}$ and 10.91 S/m, respectively. Therefore, the conductivity of the ternary composite becomes nearly 137 and 25 times higher than those of SPANI and SPANI/f-SWCNT binary composite respectively, although the conductivities still remain in the semiconducting range. This increase is attributed to the presence of gold nanoparticles, making available more electrons as charge carriers for the n-type

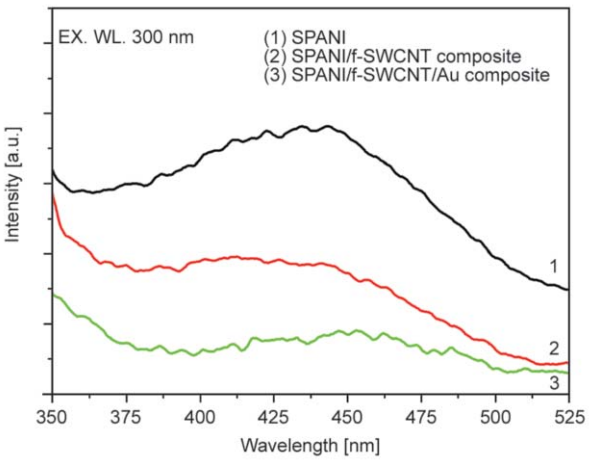

Figure 9. Photoluminescence spectra for SPANI, SPANI/f-SWCNT binary composite and SPANI/f-SWCNT/Au ternary composite

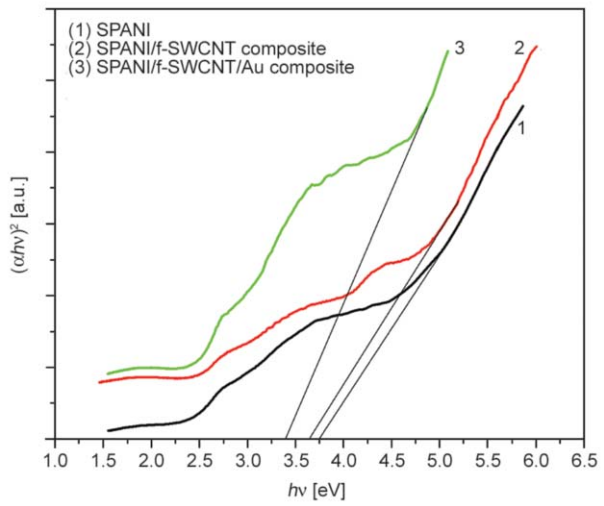

Figure 8. Plot of $(\alpha h\nu)^2$ vs. hν for SPANI, SPANI/f-SWCNT binary composite and SPANI/f-SWCNT/Au ternary composite for optical band gap calculation

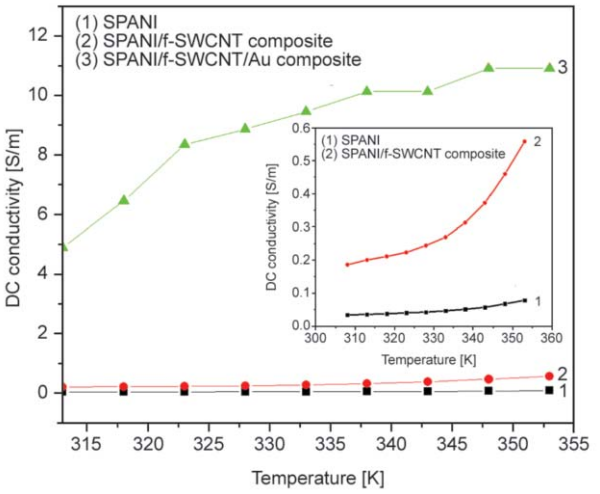

Figure 10. Comparison of dc conductivity of SPANI/f-SWCNT/Au ternary composite with SPANI and SPANI/f-SWCNT binary composite at varying temperature; comparision between SPANI and SPANI/f-SWCNT is shown in the inset

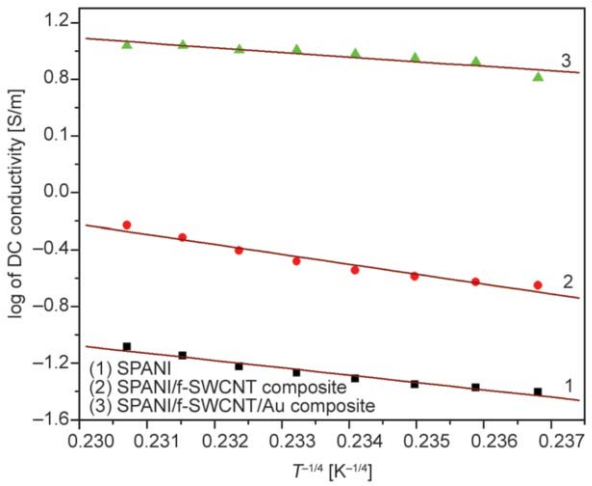

Figure 11. Variation of log of DC conductivity of SPANI, SPANI/f-SWCNT binary composite and SPANI/f-SWCNT/Au ternary composite with $T^{-1/4}$ [$K^{-1/4}$] satisfying VRH model with γ = ¼

semiconductor, and supports the band gap estimations from the absorption data plotted in Figure 7.

In order to understand the electrical conduction mechanism, the log of dc conductivity of all samples were plotted against $T^{-1/4}$, which resulted in a straight line indicating a three-dimensional variable range hopping (3D VRH) conduction mechanism of Mott (Figure 11) [25]. The estimated values of Mott temperature were $4.38 \cdot 10^6$, $1.38 \cdot 10^7$ and $1.08 \cdot 10^6$ K for SPANI, SPANI/f-SWCNT binary composite and SPANI/f-SWCNT/Au ternary composite, respectively. The significant decrease of Mott temperature in the ternary composite indicates a less disordered system, which is due to the presence of f-SWCNT/Au nanohybrid fillers in the sample. A similar decrease in Mott temperature due to introduction of Au nanoparticles into PANI has been observed previously by other researchers [23, 25].

4. Conclusions

In the present study, we have shown a simple wet chemical route to synthesize a 3-phase nanocomposite of SWCNT/Au nanohybrid fibers embedded in sulfonated polyaniline with excellent solution and electrical properties. The sulfonated composite is water soluble which can be very useful for its further processing. The synthesized nanocomposite has been characterized for its structural, thermal, electrical and optical properties. Optical absorption spectroscopy was used to estimate the band gaps which showed reduction I band gap as a function of incorporation of SWCNT and SWCNT/Au nanohybrids fillers. The DC electrical conductivity measurements showed significant increase in the electrical conductivity of the ternary composite compared to those of both SPANI and SPANI/SWCNT binary composite, in good agreement with the measured band gaps. The enhanced conductivity of the water soluble composite may find applications in electromagnetic interference (EMI) shielding [26], energy storage etc. But such a three-component polymer composite can primarily be utilized as an electrode material in biosensors [27] because of the excellent electrochemical properties of polyaniline and its composites, as well as for their long-term environmental stability. Further Au has a great affinity to attach biomolecules.

Acknowledgements

The authors are indebted to the TEQIP- I scheme of the Government of India for providing the laboratory and instrumental facilities at National Institute of Technology Durgapur, India. We also express thanks to the MHRD funded Centre of Excellence in Advanced Materials at NIT Durgapur for providing laboratory support.

References

[1] Li X-G., Feng H., Huang M-R., Gu G-L., Moloney M. G.: Ultrasensitive Pb(II) potentiometric sensor based on copolyaniline nanoparticles in a plasticizer-free membrane with a long lifetime. Analytical Chemistry, **84**, 134–140 (2012).
DOI: 10.1021/ac2028886

[2] Li X-G., Huang M-R., Lu Y-Q., Zhu M-F.: Synthesis and properties of processible copolymer microparticles from chloroanilines and aniline. Journal of Materials Chemistry, **15**, 1343–1352 (2005).
DOI: 10.1039/B412587H

[3] Meriga V., Valligata S., Sundaresan S., Cahill C., Dhanak V. R., Chakraborty A. K.: Optical, electrical, and electrochemical properties of graphene based water soluble polyaniline composites. Journal of Applied Polymer Science, **132**, 42766/1–42766/9 (2015).
DOI: 10.1002/app.42766

[4] De Volder M. F. L., Tawfick S. H., Baughman R. H., Hart A. J.: Carbon nanotubes: Present and future commercial applications. Science, **339**, 535–539 (2013).
DOI: 10.1126/science.1222453

[5] Chakraborty A. K., Coleman K. S., Dhanak V. R.: The electronic fine structure of 4-nitrophenyl functionalized single-walled carbon nanotubes. Nanotechnology, **20**, 155704/1–155704/6 (2009).
DOI: 10.1088/0957-4484/20/15/155704

[6] Kar P., Choudhury A.: Carboxylic acid functionalized multi-walled carbon nanotube doped polyaniline for chloroform sensors. Sensors and Actuators B: Chemical, **183**, 25–33 (2013).
DOI: 10.1016/j.snb.2013.03.093

[7] Lafuente E., Callejas M. A., Sainz R., Benito A. M., Maser W. K., Sanjuán M. L., Saurel D., de Teresa J. M., Martínez M. T.: The influence of single-walled carbon nanotube functionalization on the electronic properties of their polyaniline composites. Carbon, **46**, 1909–1917 (2008).
DOI: 10.1016/j.carbon.2008.07.039

[8] Kang M. S., Shin M. K., Ismail Y. A., Shin S. R., Kim S. I., Kim H., Lee H., Kim S. J.: The fabrication of polyaniline/single-walled carbon nanotube fibers containing a highly-oriented filler. Nanotechnology, **20**, 085701/1–085701/6 (2009).
DOI: 10.1088/0957-4484/20/8/085701

[9] Dhand C., Solanki P. R., Datta M., Malhotra B. D.: Polyaniline/single-walled carbon nanotubes composite based triglyceride biosensor. Electroanalysis, **22**, 2683–2693 (2010).
DOI: 10.1002/elan.201000269

[10] Wei X-L., Wang Y. Z., Long S. M., Bobeczko C., Epstein A. J.: Synthesis and physical properties of highly sulfonated polyaniline. Journal of the American Chemical Society, **118**, 2545–2555 (1996).
DOI: 10.1021/ja952277i

[11] Agrawalla R. K., Paul R., Sahoo P. K. Chakraborty A. K., Mitra A. K.: A facile synthesis of a novel optoelectric material: A nanocomposite of SWCNT/ZnO nanostructures embedded in sulfonated polyaniline. International Journal of Smart and Nano Materials, **5**, 180–193 (2014).
DOI: 10.1080/19475411.2014.937471

[12] Santhosh P., Gopalan A., Lee K-P.: Gold nanoparticles dispersed polyaniline grafted multiwall carbon nanotubes as newer electrocatalysts: Preparation and performances for methanol oxidation. Journal of Catalysis, **238**, 177–185 (2006).
DOI: 10.1016/j.jcat.2005.12.014

[13] Feng X., Mao C., Yang G., Hou W., Zhu J-J.: Polyaniline/Au composite hollow spheres: Synthesis, characterization, and application to the detection of dopamine. Langmuir, **22**, 4384–4389 (2006).
DOI: 10.1021/la053403r

[14] Wang Z., Yuan J., Li M., Han D., Zhang Y., Shen Y., Niu L., Ivaska A.: Electropolymerization and catalysis of well-dispersed polyaniline/carbon nanotube/gold composite. Journal of Electroanalytical Chemistry, **599**, 121–126 (2007).
DOI: 10.1016/j.jelechem.2006.09.021

[15] Chang Q., Kai Z., Chen X., Li M., Liu J.: Preparation of gold/polyaniline/multiwall carbon nanotube nanocomposites and application in ammonia gas detection. Journal of Materials Science, **43**, 5861–5866 (2008).
DOI: 10.1007/s10853-008-2827-3

[16] Lee K-P., Gopalan A. I., Santhosh P., Lee S. H., Nho Y. C.: Gamma radiation induced distribution of gold nanoparticles into carbon nanotube-polyaniline composite. Composites Science and Technology, **67**, 811–816 (2007).
DOI: 10.1016/j.compscitech.2005.12.030

[17] Guo L., Peng Z.: One-pot synthesis of carbon nanotube-polyaniline-gold nanoparticle and carbon nanotube-gold nanoparticle composites by using aromatic amine chemistry. Langmuir, **24**, 8971–8975 (2008).
DOI: 10.1021/la8010458

[18] Rima P., Mitra A. K.: Synthesis and study of optical and electrical characteristics of single-wall carbon nanotube/gold nanohybrid. Journal of Nano Research, **17**, 27–33 (2012).
DOI: 10.4028/www.scientific.net/JNanoR.17.27

[19] Ansari M. O., Khan M. M., Ansari S. A., Amal I., Lee J., Cho M. H.: *p*TSA doped conducting graphene/polyaniline nanocomposite fibers: Thermoelectric behavior and electrode analysis. Chemical Engineering Journal, **242**, 155–161 (2014).
DOI: 10.1016/j.cej.2013.12.033

[20] Scolari M., Mews A., Fu N., Myalitsin A., Assmus T., Balasubramanian K., Burghard M., Kern K.: Surface enhanced Raman scattering of carbon nanotubes decorated by individual fluorescent gold particles. Journal of Physical Chemistry C, **112**, 391–396 (2008).
DOI: 10.1021/jp076190i

[21] Sumanasekera G. U., Allen J. L., Fang S. L., Loper A. L., Rao A. M., Eklund P. C.: Electrochemical oxidation of single wall carbon nanotube bundles in sulfuric acid. Journal of Physical Chemistry B, **103**, 4292–4297 (1999).
DOI: 10.1021/jp984362t

[22] Tauc J.: Optical properties and electronic structure of amorphous Ge and Si. Materials Research Bulletin, **3**, 37–46 (1968).
DOI: 10.1016/0025-5408(68)90023-8

[23] Gupta K., Jana P. C., Meikap A. K.: Electrical transport and optical properties of the composite of polyaniline nanorod with gold. Solid State Sciences, **14**, 324–329 (2012).
DOI: 10.1016/j.solidstatesciences.2011.12.003

[24] Mott N. F., Davis E. A.: Electronic processes in non-crystalline materials. Oxford University Press, New York (1979).

[25] Chakraborty G., Ghatak S., Meikap A. K., Woods T., Babu R., Blau W. J.: Characterization and electrical transport properties of polyaniline and multiwall carbon nanotube composites. Journal of Polymer Science Part B: Polymer Physics, **48**, 1767–1775 (2010).
DOI: 10.1002/polb.22042

[26] Saini P., Choudhary V., Singh B. P., Mathur R. B., Dhawan S. K.: Polyaniline–MWCNT nanocomposites for microwave absorption and EMI shielding. Materials Chemistry and Physics, **113**, 919–926 (2009).
DOI: 10.1016/j.matchemphys.2008.08.065

[27] Dhand C., Dwivedi N., Mishra S., Solanki P. R., Mayandi V., Beuerman R. W., Ramarishna S., Lakshminarayanan R., Malhotra B. D.: Polyaniline-based biosensors. Nanobiosensors in Disease Diagnosis, **4**, 25–46 (2015).
DOI: 10.2147/NDD.S64841